Optical Tweezers Tensiometry

pushing the boundaries

F.C.M. Boon

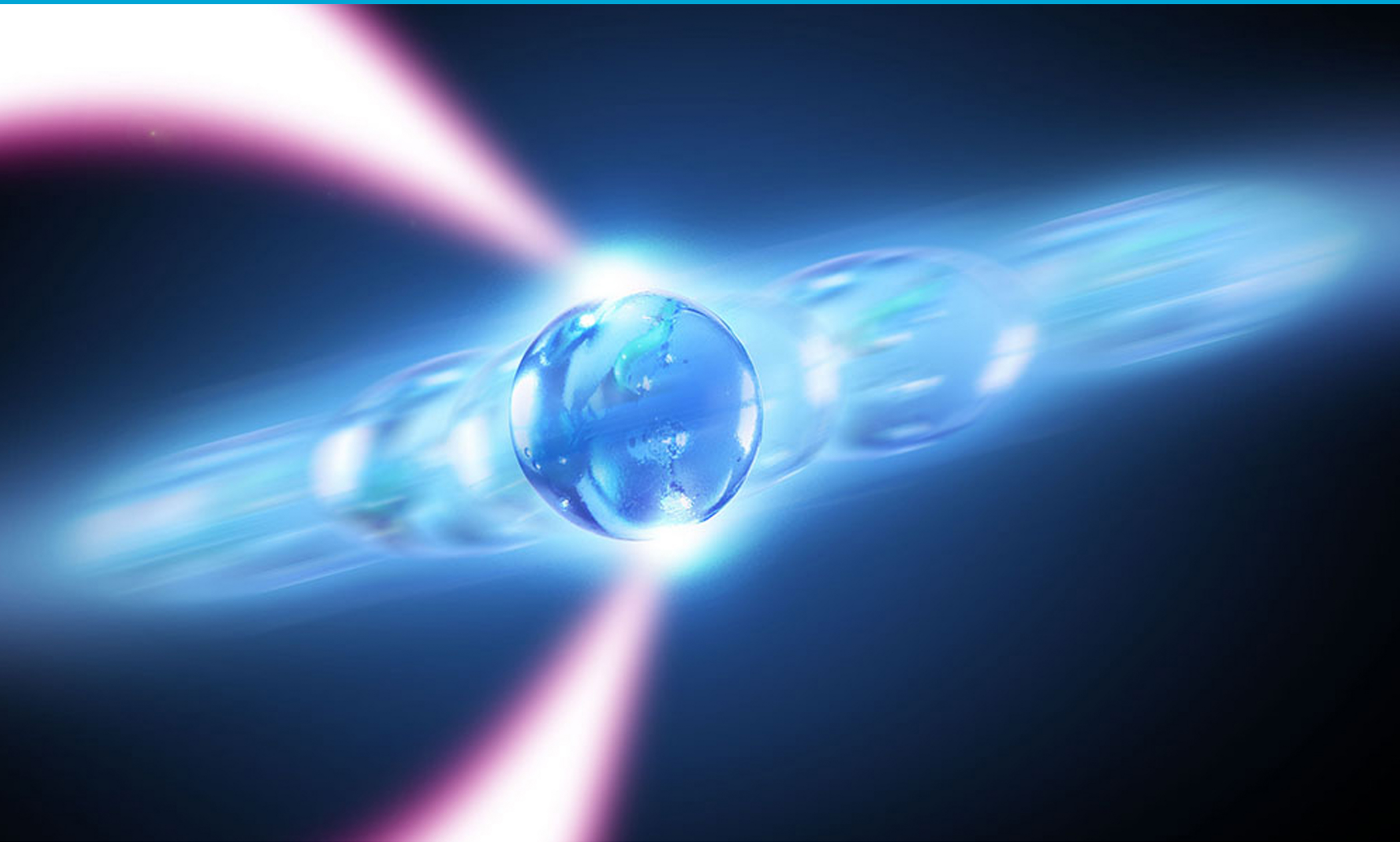

TU Delft

laboratory for Aero & Hydro Dynamics

Bionanoscience Department
Think big about life at the smallest scale

Optical Tweezers Tensiometry

pushing the boundaries

by

F.C.M. Boon

to obtain the degree of Master of Science
at the Delft University of Technology,
to be defended publicly on Friday December 4, 2020 at 2:00 PM.

Student number:	4295935	
Project duration:	October 21, 2019 – December 4, 2020	
	experimental work halted from 9 March 2020 - 15 June 2020 due to corona measures	
Thesis committee:	Prof. dr. ir. W. van de Water,	TU Delft, supervisor
	Dr. D. S. W. Tam,	TU Delft, supervisor
	Dr. L. Botto	Process & Energy (3mE) - TU Delft
	Dr. ir. R. A. J. van Ostayen	Precision and Microsystems Engineering (3mE) - TU Delft

An electronic version of this thesis is available at `http://repository.tudelft.nl/`.
Front page picture from University of Rochester, Michael Osadciw.

Preface

Before you lies the master thesis that marks the end of my time as a student at Delft University of Technology. The thesis has been written for completion of the MSc Mechanical Engineering, with a specialisation in Energy, Flow and Process Technology. I had the honor of conducting my research in two groups at different faculties: the Laboratory for Aero & Hydronamics (3mE) and the Aubin-Tam group (AS). What made my thesis truly a great experience was working together with academic professionals having different backgrounds, teaching me how to view the same problem from different angles.

I would like to thank my supervisors Willem and Daniel, in the first place for teaching me the art of conducting scientific research, but also for sparking my interest in the field of fluid dynamics with the courses you teach. I can say with great certainty that without your inspiration I would have chosen a different path. The lessons you have thought me in our meetings on what it means to conduct sound scientific research, I will carry throughout the rest of my life - independent of my future career path.

Furthermore, I would like to thank Marie-Eve. I am grateful to her for granting me the opportunity of working with the optical tweezers in her lab, as well as the numerous useful suggestions she had to make the method work. I would also like to thank Guillermo, who taught me all the magic involved in conducting these complex experiments. I would like to thank all the other people in the Aubin-Tam group too, for making the experience very pleasant. Especially many thanks to Roland: not only for the endless interesting conversational topics, but also for being enormously helpful.

This thesis would not have been possible without the help and support I got from those who are close to me: my family, friends and boyfriend. I thank you for being there throughout all the highs and lows this year gave us and listening to endless stories about optical trapping. I promise that I will find new conversational topics after my graduation.

It is with a great feeling of excitement that I look back upon the two-and-a-bit years that make my masters program at TU Delft. I have had the pleasure of working with many great people from all over the world - of which many I now call my friends.

Moreover, I would like to thank the members of the thesis committee for evaluating my work: dr. L. Botto and dr. ir. R.A.J. van Ostayen.

Last, but not least, I would like to thank you - if I have not already done that - for having finished the first page of my report. I hope you will enjoy reading the rest of it as much as I did whilst conducting the research.

F.C.M. Boon
Delft, December 2020

Abstract

The interfacial tension is a fundamental property of liquid-liquid systems and governs the mixing potential of two immiscible fluids. For two fluids to form a stable mixture, their interfacial tension needs to be very low. Applications of systems with a low interfacial tension find a plethora of applications: for example, in the food industry, for generating oil-water emulsions, or in the pharmaceutical industry, where characterising the mixture is important for the drug delivery. Despite the numerous industrial applications, characterising low interfacial tension remains a challenge. Traditional direct force measurement techniques, such as the Wilhelmy Plate method, have difficulties resolving the small forces involved. Other conventional drop distortion techniques, such as spinning drop tensiometry, require long calibration time and can have error margins up to 60%.

This thesis investigates the potential of utilising the optical tweezers for studying low interfacial tensions and developed a method to do so. In this set-up, a highly focused laser beam holds a micron-sized sphere: similar to a pair of tweezers. As light refracts through the bead, momentum is transfered and thus exerts a force. The light refraction is also used for position detection, allowing for a spatial resolution of 0.1-2 nm.

Figure 1 presents a graphical abstract of the experiment. As a micro-sphere (1), which is hold by the optical tweezers (2), is pushed against an interface (3), the forces exerted on the bead are probed allowing for the interfacial tension to be determined. Combining the excellent spatial resolution of the optical tweezers with fitting a minimal surface model, the set-up has the potential to measure the interfacial tension over a range of decades.

We have researched the dodecane-water interface, where we added glycerol to the aqueous phase to match the index of refraction. The interfacial tension was lowered by adding Span-80 or the combination of Span-80 and SDS. We have been able to conduct several measurements on interfaces with estimated values of $\gamma = 10^{-6}$ - $10^{-3}\,\mathrm{N\,m^{-1}}$. We find that the system is highly dependent on the different in index of refraction between the two fluids as well as the curvature of the interface. However, discrepancies between literature values and measurements arise due to the altering of the fluid properties and interfacial dimensions. We conclude that the use of optical tweezers to measure low interfacial tension is promising, however its speed and accuracy are reduced due to the strong requirement to match the index of refraction.

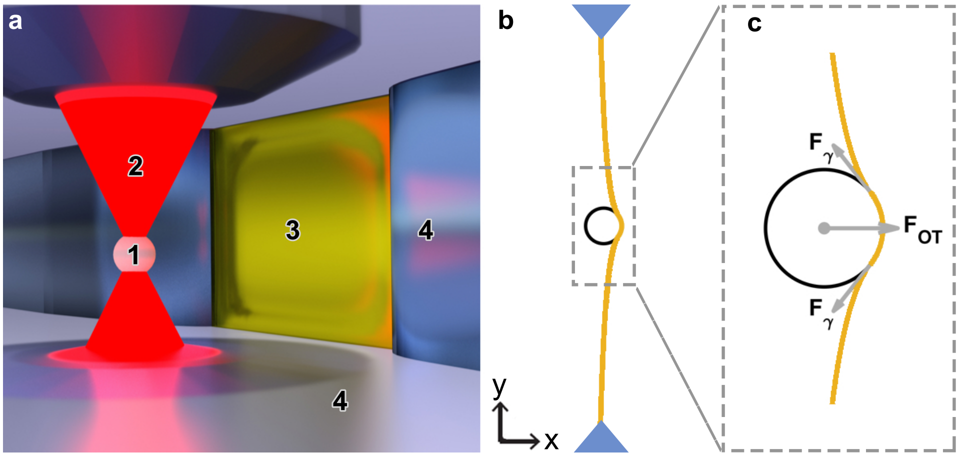

Figure 1: Graphical abstract. (a.) A side view artist impression of the experiment. A micro-sphere (1) is held by optical tweezers (2) and pushed against an interface (3) to deduce the interfacial tension. The interface is spanned along the aperture in a microfluidic device (4). Picture adapted from [1]. (b.) A schematic top view of the bead pushing the interface, top view. (c.) Force balance on the bead pushing the interface. F_γ denotes the interfacial tension, and F_{OT} the trapping force exerted by the optical tweezers on the bead.

Contents

1 Introduction **1**
1.1 Background 1
1.2 Existing methods to measure interfacial tension 4
1.2.1 Overview of methods 9
1.3 Optical tweezer tensiometry 12

2 Experimental Design **13**
2.1 Introduction to optical tweezers tensiometry 13
2.2 Background 14
2.2.1 Optical tweezers and Brownian Motion 14
2.2.2 Calibrating the trapping stiffness 16
2.2.3 Microrheology and optical tweezers 17
2.3 Experimental set-up 19
2.4 Data processing 22
2.4.1 Fitting the model to the data 23
2.4.2 Sensitivity 24
2.5 Design of experimental parameters 26
2.5.1 Estimating the index of refraction 26
2.5.2 Trapping behaviour in aqueous glycerol 26
2.5.3 Trapping near an interface with large Δn_D 27
2.6 Materials & methods 30
2.6.1 Device preparation 30
2.6.2 Liquids preparation 31
2.6.3 Setting up the optical tweezers 32

3 The Minimal Surface Model **35**
3.1 Working principle 35
3.2 Computing the shape of the interface 36
3.2.1 Results 38
3.3 Computing the force exerted on the bead 40
3.3.1 Results 40
3.4 Parametric study 42

4 Results **45**
4.1 Dodecane-water/glycerol interface containing Span-80 45
4.2 Dodecane-water/glycerol interface containing Span-80 and SDS 46
4.3 Scatterplots near the interface 47

5 Further Observations/Limitations **49**
5.1 The optical drift is proportional to the laser power 49
5.2 The optical drift differs per interface 49
5.3 The position variance increases upon touching the interface 49
5.4 The calibration curve changes per laser power 52
5.5 Surfactant-loaden interfaces are dirty 52

6 Discussion and Conclusion **55**
6.1 Discussion on the obtained results 55
6.2 Limitations 56
6.3 Are the optical tweezers suitable as a tensiometer? 57

7 Recommendations 59

A Literature values for the estimated interfacial tension 61

B Estimating the refractive index 63

C Setting up the optical tweezers 65

D Model adaptations for this thesis 67

E Full results 69
- E.1 Exp 1 - Interface containing Span-80 69
- E.2 Exp 2.1 - Interface containing Span-80 70
- E.3 Exp 2.2 - Interface containing Span-80 71
- E.4 Exp 3.1 - Interface containing Span-80 and SDS 72
- E.5 Exp 3.2 - Interface containing Span-80 and SDS 73
- E.6 The position variance is found not to vary due to noise 74
- E.7 The device does not influence the optical drift or variance fluctuations 78
- E.8 Parallel to the interface 79
- E.9 Stiffness as function of distance to interface 81

F Absorbance spectrum 83

G MATLAB code model 85

Bibliography 87

Nomenclature

γ	interfacial tension
κ_x	trapping stiffness in the x-direction
Λ	minor or major axis of scattered data
λ	wavelength of light
μ_x	mean position in the x-direction
ϕ	orientation of scattered data
σ_x^2	variance in the x-direction
θ	interface wrapping angle of A_{sphere}
θ_{min}	the minimal surface wrapping angle of A_{sphere}
A_{cat}	interfacial area that forms a catenoid
A_{min}	total minimal area
A_{sphere}	interfacial area that wraps around bead
CMC	critical micelle concentration
d_b	bead diameter
d_x	bead position relative to the focal point center, in x-direction
$displacement$	the position of the interface relative to the focal point
e	eccentricity of scattered data
F_γ	force exerted by the interface, due to interfacial tension
F_{OT}	force exerted by the optical tweezers, trapping force
$FTIR$	Fourier-transform infrared spectroscopy
$index\ matching$	matching the index of refraction by altering the fluid properties
k_B	Boltzmann constant
n	index of refraction
n_D	index of refraction at the sodium D-line, λ = 589 nm
$NOA-81$	Norland Optical Adhesive-81. The material of the channels in the microfluidic device
PSD	Position Sensitive Device
$PwSD$	Power Spectral Density
r_b	bead radius
R_{aper}	radius of aperture,
$S-80$	Span-80 or sorbitane monooleate. One of the two surfactants used in this study.

SDS	Sodium Dodecyl Sulfate. One of the two surfactants used in this study.
T	temperature
V_x	voltage in the x-direction
z_b	position of bead center

1

Introduction

Boundaries between two immiscible fluids are readily deformable: free to change their shape in order to minimize their exposed surface area. The resulting force at the interface is the interfacial tension: a key parameter for many industries, dominating the fluids mixing potential. In many every day applications it is desirable that water and oil are mixed: for example, in the food industry (mayonnaise, margarine), the cosmetic industry (lotions) and in your own kitchen, when cleaning a greasy pan. By adding soap to the dishes, the mixing potential of the water and oil is increased. The soap, or surfactant, allows the oil to be taken away by the water, and the pan can be cleaned. Such a temporary mixture of two immiscible fluids is called an emulsion, and the mixing potential is governed by a phenomenon called the interfacial tension.

In some industrial applications it is favourable to make oil-water mixtures with ultra-low interfacial tension, which is done by adding two or multiple surfactants [2]. An example occurs in industrial oil production. After the first two rounds of oil extraction from a reservoir, approximately two-thirds of the oil remains trapped [3]. By injecting a solution with surfactants, the oil can be dislodged from the reservoir pores. Ultra-low interfacial tension systems occur in many other large-scale industrial applications, such as in environmental protection (*e.g.* oil pollution remediation) or pharmaceutical industries (*e.g.* drug delivery systems). For these industries, the effectiveness and stability of the product mixture is governed by the interfacial tension as well as particular characteristics of the surfactants used.

Despite the utility of these systems, characterising ultra-low interfacial tension remains a challenge today. Traditional methods struggle to resolve the small forces involved, as can be found in Section 1.2. Many academic endeavours have been made to find a way to characterise ultra-low interfacial tension systems, indicating the need for an accurate and reliable measurement technique.

1.1. Background

Interfacial tension: a working definition

A molecule in the bulk of a fluid is surrounded by attractive neighbours, having the same chemical structure. A molecule at the boundary of a fluid has a reduced number of attractive neighbours and is thus in an energetically unfavourable state, as shown in Figure 1.1. This is the fundamental reason liquids adjust their shape to expose the smallest boundary possible: think about small fluid bodies that have the tendency to evolve into spheres. For example, a thin fluid jet coming out of a faucet will pinch off into spherical droplets in order to minimise the total surface area. The interfacial tension is a direct measure of the energy shortfall per unit area, and typically denoted by γ, having units of $\mathrm{J\,m^{-2}}$. The stronger the cohesive bonds between the molecules, the larger the excess energy at the interface will be. Also, if the molecules at each side of the boundary are very dissimilar, the remaining excess energy at the interface will be large [4]. For example, the molecules at a water-air interface have a large excess energy of $72.8\,\mathrm{mJ\,m^{-2}}$, due to the strong, cohesive hydrogen bonds between the water molecules that are unsaturated at the boundary. On the other hand, the interfacial tension is low between water and a short-chain alcohol, like 1-butanol, since both fluids form hydrogen bonds: $1.8\,\mathrm{mJ\,m^{-2}}$. In general, γ depends on the two fluids in contact, temperature and the presence of surfactants or impurities at the interface.

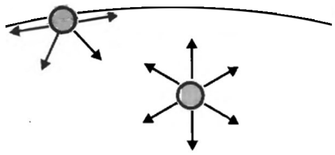

Figure 1.1: The interfacial tension is the excess energy of unsaturated intermolecular interactions at the interface and causes the fluid to minimise its exposed boundary, resulting in a curved interface. Picture adapted from [5].

Interfacial tension can also be thought of as a force per unit length. Dimensionally, $\mathrm{J\,m^{-2}}$ is equivalent to $\mathrm{N\,m^{-1}}$, and γ can be interpreted as a line force acting in all directions, parallel to the interface. As a consequence, a pressure difference occurs across curved interfaces. Consider a spherical oil droplet inside water, as in Figure 1.2, having a radius R. If p_i and p_o are the pressures on the inner and outer side of the droplets interface, then a static force balance gives Equation 1.1:

$$\gamma(2\pi R) = (p_i - p_o)\pi R^2 \tag{1.1}$$

which can be written as

$$p_i - p_o = 2\gamma/R$$

The curvature of a general surface can be expressed by the radii of curvature along two orthogonal directions, R_1 and R_2. In this case, the analysis results in an equation named the **Laplace equation**, Equation 1.2:

$$\Delta p = 2\gamma\left(\frac{1}{R_1} + \frac{1}{R_2}\right) \tag{1.2}$$

which is consistent with the previous result for a spherical droplet, where $R_1 = R_2$.

The Laplace equation is used in various interfacial tension measurement techniques to estimate the interfacial tension. For example, in the pendant drop technique (see Figure 1.6), a drop hangs from a needle and gravitational forces balance interfacial tension. A force balance can be made on the drop, as in Equation 1.4:

$$\gamma\left(\frac{1}{R_1} + \frac{1}{R_2}\right) = \Delta p = \Delta p_o - \Delta\rho g z \tag{1.3}$$

where $\Delta\rho$ denotes the difference in density between the two liquid phases, g is the gravitational constant and z the distance from the apex. Taking advantage of the drop axisymmetry, this Equation 1.4 can be expressed in cylindrical coordinates and a set of equations can be obtained, predicting the drops profile as a function of γ.

Interfacial tension can be lowered by adding a surfactant

A surfactant, or surface active agent, has the ability to lower the interfacial tension between two fluids. The surfactant molecule has a a hydrophobic, or water-hating, ”tail” and a hydrophilic, or water-loving, ”head”. When adsorbed onto an oil-water interface, the hydrophobic part aligns towards the oil side and the hydrophilic part aligns towards the water phase as shown in Figure 1.4. The surfactant molecule lowers the interfacial tension by partially satisfying the missing cohesive bonds at both sides of the boundary. The interfacial tension decreases rapidly upon increasing the concentration of surfactants. This has a limit: at a certain concentration, namely the critical micelle concentration (CMC), the interface is saturated and the interfacial tension no longer decreases upon adding surfactant. At this point, the surfactant molecules start to aggregate in the bulk fluid to form structures, such as micelles.

Different types of surfactant exists. Mainly the hydrophilic ”head” has different properties, such that it can have no polar charge (non-ionic), but can also have a net positive or negative charge (anionic). The hydrophobic ”tail” typically consists of a chain of hydrocarbons. A combination of two surfactants can lead to a lower interfacial tension compared to the equivalent mixture, containing just a pure surfactant

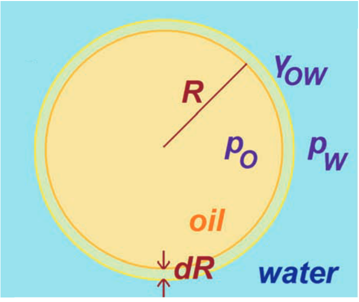

Figure 1.2: A control volume around a spherical oil droplet. Picture reprinted from [6].

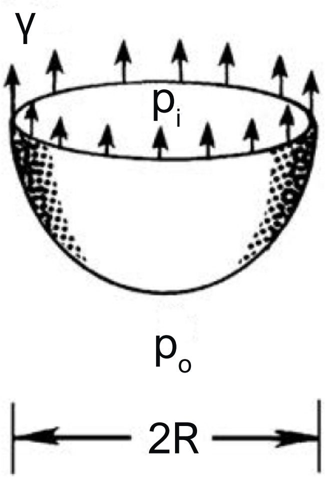

Figure 1.3: Section of a spherical droplet, showing the interfacial tension forces and resulting pressure difference. Picture adapted from [7].

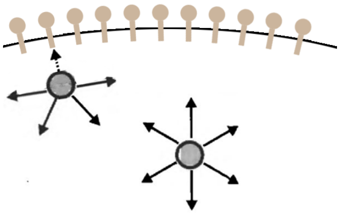

Figure 1.4: Surfactants lower the interfacial tension by partially satisfying cohesive bonds. Picture adapted from [5].

[8]. This synergy can be attributed to formation of different types of bonds, such as hydrogen bonds, but also better molecular stacking at the interface [9].

Let consider an water-hydrocarbon interface, such as water-dodecane. Without any surfactant, the resulting interfacial tension is $53 \times 10^{-3}\,\mathrm{N\,m^{-1}}$, as can be seen in Table 1.1. Upon adding the non-ionic surfactant Span-80 at the CMC, the interfacial tension drops significantly. Adding the anionic surfactant SDS also lowers the interfacial tension, but to a similar value as adding Span-80. But, if both surfactants are added at their CMC a synergy is observed: the interfacial tension drops three orders of magnitude.

Table 1.1: The interfacial tension reduces by adding a surfactant. Some combinations of surfactants cooperate such that the value of γ is reduced to far below their own. Values obtained from [10–12].

Interface	Surfactant	γ in $\mathrm{N\,m^{-1}}$
water-oil		53×10^{-3}
	Span-80	5×10^{-3}
	SDS	7×10^{-3}
	Span-80 and SDS	6×10^{-6}

1.2. Existing methods to measure interfacial tension

Immiscible fluids have a plethora of applications, and the interfacial tension is one of the fundamental properties that dictates their behaviour. Techniques for measuring the interfacial tension have been of scientific interest for over a century, since accurate and efficient methods of measuring interfacial tension are important to the development of oil-water mixtures, such as emulsions and dispersions.

This section describes various methods to measure interfacial tension and classifies them according to the core principle: an overview can be found in Figure 1.5. In absence of other forces, *e.g.* in zero gravity, the liquid has the tendency to form a spherical shape in order to minimize the excess energy of the interface. The first classification of techniques distorts the drop. The drop shape under a force is observed, and a fit of a theoretical curve, typically using the Laplace equation, is made. The second group directly measures the interfacial tension, using a microbalance or microprobe. The interface adheres to the probe, *i.e.* forms a three-phase contact line, and the resulting force per unit length is measured. The third group observes waves at the interface to deduce the interfacial tension: either present due to vibrations parallel to the gravitational field (Faraday waves) or due to random thermal fluctuations. Another way of deducing the interfacial tension follows from the break-up behaviour: as a liquid jet attempts to minimize its interfacial area, it breaks up into spherical droplets at a certain point. The fourth classification highlights a recent paper utilizing this transition. Lastly, an academic endeavour by Tsai et al. estimate the interfacial tension by analysing the dynamics of magnetic microspheres crossing the interface. It is noted that it is a conventional method for measuring surface tension includes determining the pressure due to the curvature of the interface (Figure 1.2), named capillary force techniques. Although possible, these methods are not conventional for measuring liquid-liquid interfacial tension [13].

Some of the described methods aim to be implementable onto a miniature laboratory chip in order to conduct several chemical analyses in one go. These so called ”lab-on-a-chip” devices aim to achieve automation, high-throughput and on-site analysis in, for example, the oil-industry.

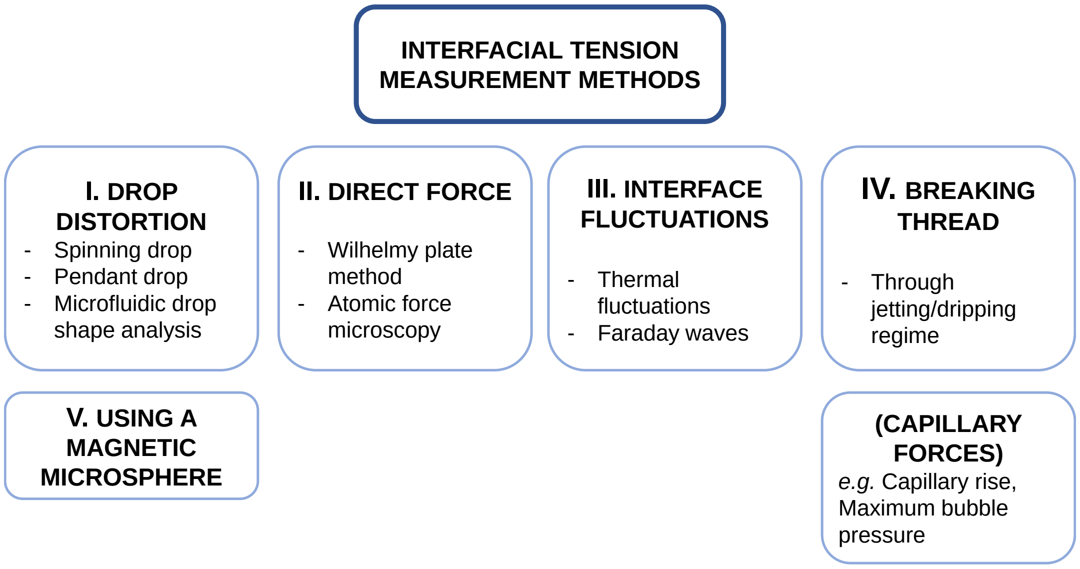
INTERFACIAL TENSION MEASUREMENT METHODS
I. DROP DISTORTION
- Spinning drop
- Pendant drop
- Microfluidic drop shape analysis
II. DIRECT FORCE
- Wilhelmy plate method
- Atomic force microscopy
III. INTERFACE FLUCTUATIONS
- Thermal fluctuations
- Faraday waves
IV. BREAKING THREAD
- Through jetting/dripping regime
V. USING A MAGNETIC MICROSPHERE
(CAPILLARY FORCES)
e.g. Capillary rise, Maximum bubble pressure

Figure 1.5: An overview of the classification for interfacial tension measurement methods.

I. Drop distortion

Pendant drop method [14]

In this simple method a drop hangs from a needle. The drop shape is determined by the balance between interfacial tension and gravitational forces, or the difference in density between the two fluids ($\Delta\rho$). A schematic of a pendant drop is shown in Figure 1.6. Using a camera, the equatorial distance D and the diameter d, at distance D from the apex of the drop, can be determined. The interfacial tension then follows from Equation 1.4:

$$\gamma = \frac{\Delta\rho g D^2}{H} \tag{1.4}$$

where H is a shape parameter dependent on d/D, and is determined by image analysis software. This software detects the edges of the drop and fits to the theoretical curve: which is governed by the Laplace equation. A widely used analysis technique is the axisymmetric drop shape analysis [15]. Drop volumes can range from 5 µL-20 µL, depending on the needle diameter, which is typically around 0.5-2 mm. The droplet volume must be sufficiently large that its shape has adjusted under the influence of gravity, *i.e.* the Bond number should be sufficiently high. On the other hand this technique is limited for Bo $\gg$ 1, when γ is very small, causing the droplet to fall. Measurement is limited for pairs of fluids with a low density contrast, interfacial tension or optical contrast. Pendant drop apparatuses and software are commercially available, where their measurement range is said to be γ = 10^{-5}-10^{-3} N m^{-1}. The lower bound on interfacial tension can only be achieved reliably for fluids that have very similar properties, *e.g.* aqueous two-phase systems [16].

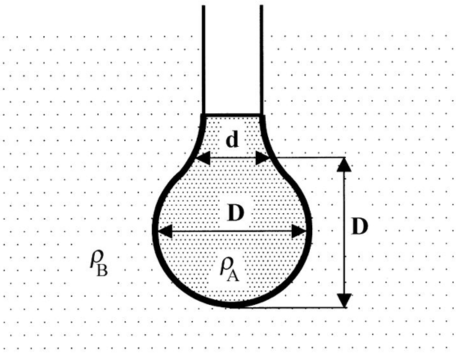

Figure 1.6: In the pendant drop method the drop deformation under gravitational forces is observed to determine the interfacial tension. Picture reprinted from [13]

Spinning Drop method [17]

In the spinning drop technique, a horizontal tube containing a dense fluid is rotated. A droplet of a less dense fluid is put inside the tube, as denoted with blue in Figure 1.7. Subject to the centrifugal forces, the droplet shape deforms to be more elongated. The elongation stops when the centrifugal forces and interfacial tension forces balance. The interfacial tension is determined by the radius (a) of the cylindrical drop, the density difference between the two fluids and the rotational velocity of the droplet (ω):

$$\gamma = \frac{1}{4} a^3 \Delta\rho\omega^2 \tag{1.5}$$

The spinning drop method is the only commercially available method to measure low interfacial tension, having a measurement range of γ = 10^{-7}- 10^{-3} N m^{-1}. The surrounding, dense fluid typically has a volume of 1 mL, whereas the droplet is on the order of several 10 µL.

Measurements using the spinning drop for low interfacial tensions < 10^{-5} N m^{-1} can have an uncertainty of 60 % [18]. Secondly, they can be time consuming: due to the low interfacial tension, it can take a up to hours before an equilibrium state has been reached [19].

Microfluidic Drop Shape Analysis

Hudson et al. [21] designed a microfluidic device based on drop-shape dynamics. Drops with certain volume and spacing are produced and decelerated under extensional flow in a microfluidic channel, as is shown in Figure 1.8. The speed is chosen relatively constant and such that the droplets do not collide, which would halt measurements. The drop deformation is computed from the drop's moments of inertia and the interfacial tension is deduced from the drop shape relaxation. The drop radius ranged from 9-220 µm. Hudson et al. were able to measure values of γ in the range 2.5-60 mN m^{-1}. This

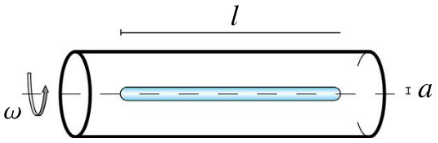

Figure 1.7: The spinning drop method exposes a droplet to centrifugal forces which counter the interfacial tension.
Picture reprinted from [20].

is limited by the viscosity of the two fluids. Also, this method is less suitable for surfactants, since gradients in the concentration at the interface may occur, resulting in fluctuations in the drop size.

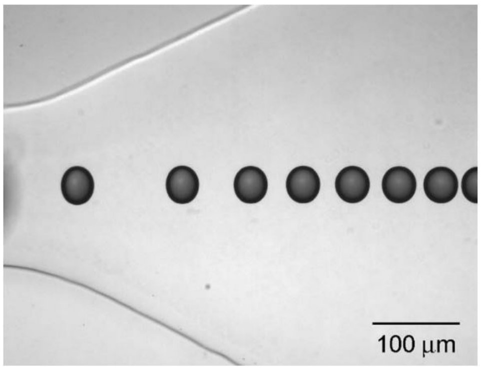

Figure 1.8: In microfluidic drop shape analysis the droplets are exposed to an extensional flow field causing the droplets to stretch in the transverse direction. Picture reprinted from [21].

II. Direct force measurement

The Wilhelmy Plate method [22]

This classic and commercially available method uses a vertical thin plate submerged in two fluids, having density ρ_A and ρ_B. The plate is put in a fixed position relative to the horizontal interface prior to conducting the measurement. The plate material is chosen such that the bottom fluid wets the material, such that the contact angle (θ) is as small as possible, preferably $\theta \approx 0$. If this approximation fails, an additional measurement determining the contact angle is needed, which proves to be cumbersome for small values of θ. The force acting vertically on the plate (F) by the liquid meniscus, due to the tendency to minimize the interfacial area, is to be measured using a microbalance, as in Equation 1.6:

$$\gamma = \frac{F}{p cos\theta} \tag{1.6}$$

where p denotes the length of the three phase contact line. In the case of Figure 1.9, $p = 2(L + t)$, where L and t denote respectively the length and thickness of the submerged thin plate. Typically, the plate has p is 2-3 centimeters and is made of roughened platinum, having an extremely high surface free energy. This technique also allows for studying the surface kinetics and surfactant adsorption for a wide variety of timescales. The method is limited to the accuracy of the microbalance: the lower the interfacial tension, the smaller F and the lower the accuracy of the measurement. The commercially available Wilhelmy Plate apparatuses have a measurement range of 1-100 mN m^{-1}.

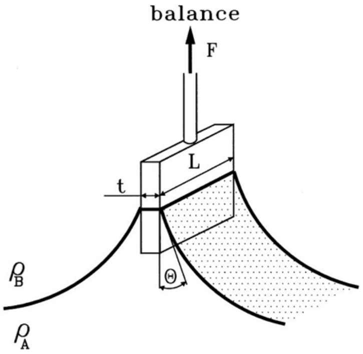

Figure 1.9: The Wilhelmy Plate method uses a microbalance to directly measure interfacial tension. Picture reprinted from [13].

Atomic Force Microscopy

Although the Atomic Force Microscope (AFM) is typically used in the field of surface physics to measure *f.e.* wetting properties on a micro- or nanoscale, it can also be utilised to measure interfacial tension [23, 24]. A micron-sized sphere, having radius R, is attached to the AFM tip. The sphere is brought into contact with a droplet to form a liquid bridge, as indicated by the blue area in Figure 1.10. Here, r_1 and r_2 are the principal radii of curvature of the bridge, θ is the contact angle at the three-phase contact line and h is the separation of the two surfaces. The AFM technique allows to resolve the small forces, in the order of piconewtons, involved in the equilibrium of the liquid bridge. Sprakel et al. [23] have measured γ=10 µN m^{-1}.

The AFM is not widely used to extract the interfacial tension due to the complexities involving the three-phase contact lines as well as complexities with electrostatic interactions between the two solids involved. For example, during wetting or de-wetting the contact line could slip over the surface of the probe [25].

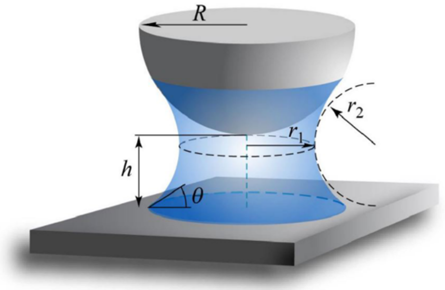

Figure 1.10: A sphere with radius R is attached to an Atomic Force Microscope (AFM) and forms a liquid bridge. The interfacial tension is deduced from the equilibrium forces. Picture reprinted from [23].

III. Interface fluctuations

Analysis of thermal fluctuations

Ultra-low interfacial tension can be determined by observing the thermal fluctuations of the interface [26–28]. For example, Bolognesi et al. measured ultra-low interfacial tension for micron-sized droplets oil droplets, see Figure 1.11. The interfacial tension is then determined by fitting the experimental results with a capillary wave model:

$$\sigma_A \propto \sqrt{k_b T/\gamma} \tag{1.7}$$

The interface fluctuation amplitudes, σ_A, were obtained using video microscopy and a contour analysis technique. Bolognesi et al. obtained values for γ 0.1-1 µN m^{-1}. The amplitude of the interfacial waves, or the intensity of the scattered light, drops readily with increasing γ, limiting this technique to the ultra-low interfacial tension.

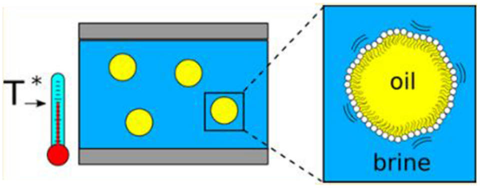

Figure 1.11: Observing the random thermal capillary waves at the droplet interface provides an estimate for the interfacial tension. Picture reprinted from [26].

Analysis of Faraday waves

Lau et al. [29] use Faraday waves for measuring ultra-low interfacial tension. Faraday waves are excited by vertically oscillating a container with two fluids, as seen in Figure 1.12. Through light reflection and image analysis, the wavelength of the Faraday waves is measured and the interfacial tension is determined using the Floquet theory by Kumar and Tuckerman (1994). The limitation for γ is determined by the density contrast between the two fluids and, for small density contrasts, by viscous dissipation. Through this technique, γ values as low as 5×10^{-4} N m^{-1} were measured. This technique is limited by surfactant dynamics at lower values of γ, and it proves experimentally difficult to set a scale for the size of the fluctuations using the scattered light.

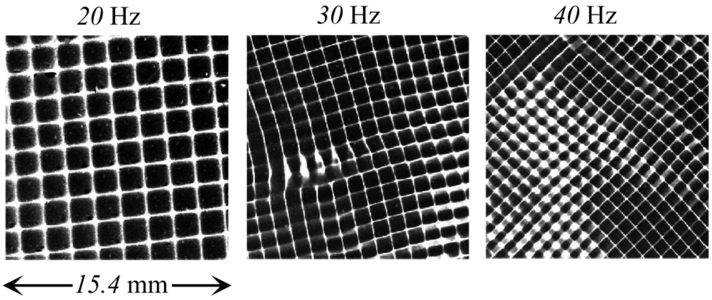

Figure 1.12: Faraday waves can be utilized for estimating γ, through observing their wavelength. The figure shows waves at three different driving frequencies for the same surfactant concentration. Picture reprinted from [29].

IV. Breaking thread method [30]

Through jetting/dripping transition

In the breaking thread method, the interfacial tension is estimated by following the breakup of an elongated drop into smaller droplets. Many academic endeavours use this principle to estimate the interfacial tension [19, 31], but an interesting microfluidic approach is highlighted below.

Moiré et al. [32] developed a microfluidic tensiometer that determines the interfacial tension by observing the point of break-up of a liquid jet. The microfluidic device is made of two coaxial capillaries, having inner diameter 250 µm and 250 µm, where the two fluids are inserted. As Figure 1.13 shows, either droplets or jetting will be observed, dependent on the flow rate. The transition between the regimes relies on the Rayleigh-Plateau instability, and experimental data points are obtained such that a flow diagram can be constructed. A model is fitted to this diagram, as well as hydrodynamic constraints such as viscosity contrast and the physical confinement, to finally obtain a value for γ. Values for the interfacial tension ranging over four decades were obtained, ranging from 0.002-30 mN m^{-1}.

The challenge of this method is to characterise the phase diagram, being strongly dependent on the combination of liquid properties, as density and viscosity. Also, the surfactant adsorption time should be sufficiently short to obtain reliable measurements through the whole flow diagram.

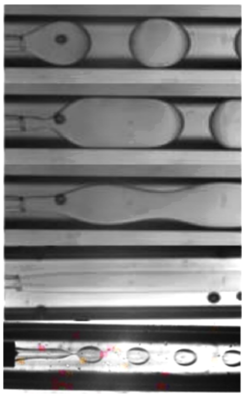

Figure 1.13: Moiré et al. use the transition from the jetting to dripping regime to estimate the interfacial tension. Different flow types in a cylindrical coaxial coflow are shown. From top to bottom: dripping, plugs, oscillating jets, straight jet and jetting behaviour. Picture reprinted from [32].

V. Deforming the interface using a magnetic microsphere

Tsai et al. [12] developed a technique to measure ultra-low interfacial tension in a microfluidic device. Paramagnetic spheres, having a radius of 2.5 µm, are suspended in one fluid. In case of Figure 1.14, the spheres are suspended in the blue, aqueous phase. As the spheres pass the co-flowing interface (50 µm x 380 µm), their behaviour is observed with video microscopy - they either pass through or are trapped in the interface. By tuning the magnet-to-interface distance, an estimate is made for the interfacial tension. Tsai et al. obtained values for γ = 10^{-6}-10^{-5} N m^{-1}.

Difficulties for this technique include the calibration of the magnetic susceptibility and the requirement of a low viscosity contrast between the two fluids.

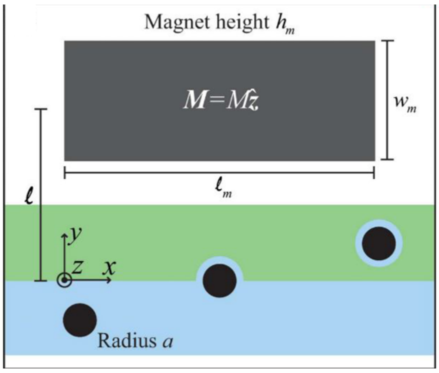

Figure 1.14: In this microfluidic approach paramagnetic spheres are pulled through the interface. Picture reprinted from [12].

1.2.1. Overview of methods

Figure 1.15 and Table 1.16 provide an overview of the discussion on the methods. Figure 1.15 shows the methods sorted on the interfacial length scale. For the same surfactant solution, the measured interfacial forces differ significantly between microscopic droplets and macroscopic drops, indicating the need to study emulsions on their relevant length scale [33–35]. Here, the interfacial length scale is defined as the volume of the droplet divided by the interfacial area. Table 1.16 shows the discussed limitations for each method. For many of the systems, the fluid properties have constraints, on their density, viscosity or optical contrast. The formation of a three-phase contact line on the measurement probe can be a source of error, *e.g.* due to difficulties determining the contact angle or slippage of the contact line. Most of the techniques use visual analysis to determine either the drop shape, break-up dynamics or the microsphere position. In the drop distortion techniques, the drops need to equilibrate before taking the measurement. At low interfacial tensions, this leads to a long relaxation time. Lastly, in the dynamic systems, surfactant dynamics can become a problem, *f.e.* by inducing Marangoni flows, resulting in a erroneous measurement.

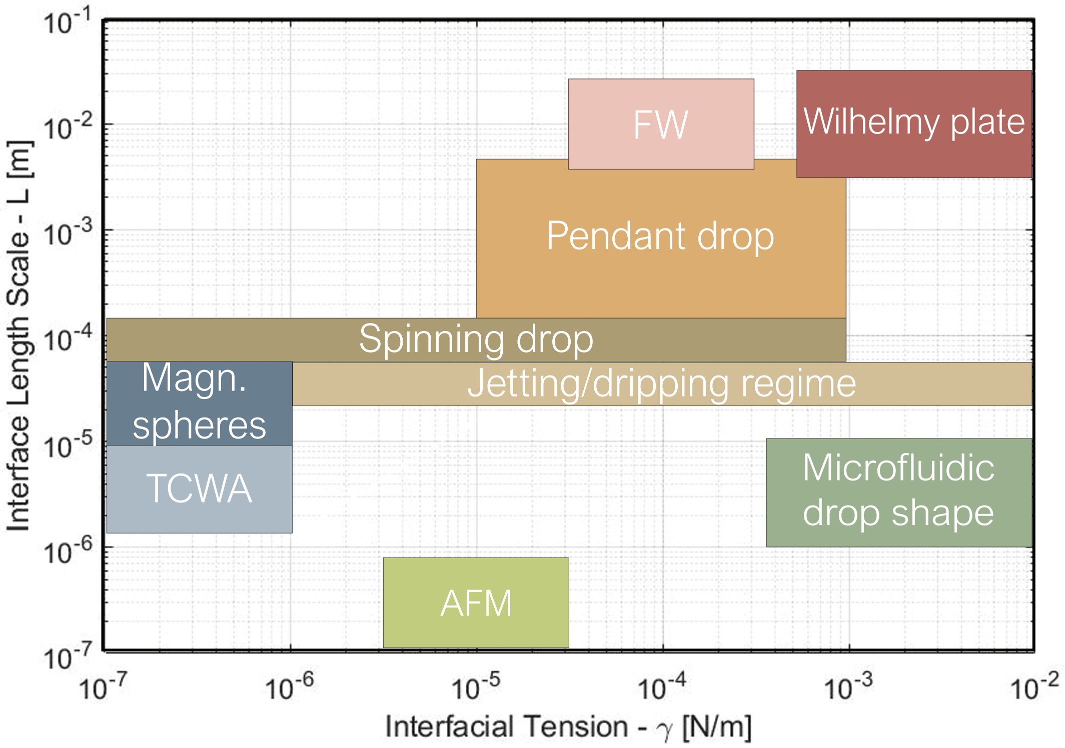

Figure 1.15: An overview of the methods studied to measure interfacial tension. **FW**: Faraday waves. **TCWA**: Thermal Capillary Wave Analysis. **Magn. spheres**: Deforming the interface using a microsphere. **AFM**: Atomic Force Microscopy.

		γ [N m-1]	Matching fluid properties	Three-phase contact line	Visual analysis	Long relaxation time	Surfactant dynamics
I. DROP DISTORTION	Pendant drop	E-5 to E-3	X		X	X	
	Spinning drop	E-7 to E-3	X		X	X	
	MDSA	E-4 to E-2	X		X	X	X
II. DIRECT FORCE	Wilhelmy plate	E-4 to E-2		X			
	AFM	E-5		X			
III. INTERFACE FLUCTUATIONS	Thermal fluctuations	E-7 to E-6			X		
	Faraday waves	E-4			X		X
IV. BREAKING THREAD	Jetting/dripping regime	E-6 to E-2	X		X		X
V. MAGNETIC MICROSPHERE		E-7 to E-6	X		X		

Figure 1.16: An overview of the discussed methods, including the measured interfacial tension (γ), in decades as well as the limitations reported for each method.

1.3. Optical tweezer tensiometry

Currently, the only commercially available method to measure ultra-low interfacial tension is spinning drop tensiometry. In this method, a droplet is distorted by exposing it to a centrifugal force field, and observing its response. Inherently, a lower interfacial tension results in a longer measurement time. The technique is further limited by the need to match certain fluid properties, such as the difference in density and viscosity. Also, the interface should be clearly visible so the drop shape can be accurately determined, which becomes a problem when surfactants are used near their CMC [12]. Due to these experimental difficulties, the measurement uncertainty can be up to 60% [18]. Lastly, spinning drop does not allow for any control over the size of the interface. The academic endeavours discussed in the previous section aim to mitigate these limitations. It is concluded that only the breaking thread method is able to measure of a wide range of interfacial tensions. However, this method is limited by the surfactant dynamics, as it is not suited for high concentrations of surfactants, or surfactant with low diffusivity, as the adsorption time is merely on the order of 100 ms. Other methods are either limited by the formation of a three-phase contact line, or rely strongly on visual analysis.

Here, we propose a microfluidic platform that utilizes optical tweezers to measure interfacial tension. The interface is formed along an aperture in the microfluidic device. An optically trapped bead is pushed against the interface, and the interfacial tension is deduced by probing the forces exerted on the bead. This technique allows for measurements over a wide range of interfacial tensions ($\gamma = 10^{-6} - 10^{-3}\,\mathrm{N\,m^{-1}}$), due to the excellent spatial and temporal resolution of the optical tweezers. It is a direct force method, but eliminates the need for a three-phase contact line. Contrary to the Wilhelmy Plate method, the measurement becomes more accurate with decreasing interfacial tension. Dols-Perez et al. [36] have measured the interfacial tension of a lipid bilayer using the optical tweezers, obtaining an interfacial tension of $2.1 \times 10^{-6}\,\mathrm{N\,m^{-1}}$. We describe modifications to utilize optical tweezers in a two-phase system and deducing the interfacial tension. Specifically, we adjust the fluid properties such that the optical contrast is sufficient, and identify key experimental outputs that indicate a reliable outcome.

2

Experimental Design

In this chapter, we detail our experimental approach to measuring interfacial tension using the optical tweezers. The first two sections provide introductory information about the experiment, the optical tweezers, constrained Brownian motion and a summary of the existing literature utilizing optical tweezers to probe interfacial tension. Section 2.3 describes the experimental set-up and defines the important notations. The data processing is described in Section 2.4, where the main variables used for the analysis are explained. The design of the experiment mainly consists of choosing certain parameters, for which the motivation can be found in Section 2.5. Lastly, Section 2.6 elaborates on the experimental procedures.

2.1. Introduction to optical tweezers tensiometry

We utilize the excellent spatial and temporal resolution of the optical tweezers to measure interfacial tension. A spherical bead, denoted by (1) in Figure 2.1.a, is trapped in the focal point of the optical tweezers (2). The microfluidic device is moved by a piezo electric stage, until the bead is pushed against an oil-water interface (3). A second laser, along the same path as the optical tweezers, is used for position detection on a Position Sensitive Device (PSD). By observing the particles deviation from the center of the trap, as well as estimating the laser trapping stiffness, an estimate of the trapping force is made. In this thesis, the bead does not pass through the interface, but merely indents it, meaning that a model is needed to obtain the interfacial tension. The measured deviation from the center is compared to this model.

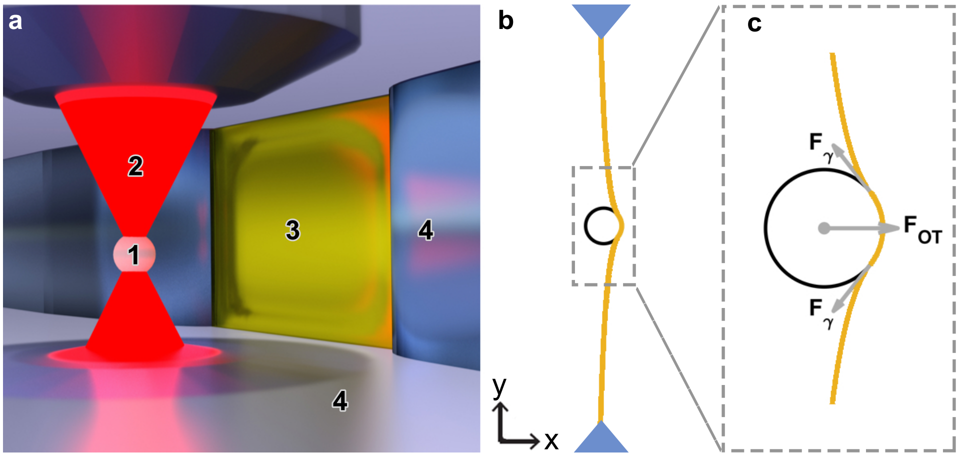

Figure 2.1: (a.) A side view artist impression of the experiment. A spherical bead (1) is optically trapped by optical tweezers (2) and pushed against an interface (3) to deduce the interfacial tension. The interface is spanned along the aperture in a microfluidic device (4). Picture adapted from [1]. (b.) A schematic top view of the bead pushing the interface, top view. (c.) Force balance on the bead pushing the interface. F_γ denotes the interfacial tension, and F_{OT} the trapping force exerted by the optical tweezers on the bead.

2.2. Background

2.2.1. Optical tweezers and Brownian Motion

Optical tweezers are a laser-based method for trapping and manipulating microscopically small particles, using the ability of light to exert force. Since the discovery in 1970 by Ashkin [37, 38], the optical tweezers have revolutionised the field of biophysics, allowing for trapping of viruses, bacteria and atoms. His discovery granted Ashkin part of the 2018 Nobel Prize in Physics. The optical tweezers consist of a single focussed laser beam, producing attractive forces on trapped dielectric objects, including viruses, bacteria, living cells and even strands of DNA. In this thesis, the trapped object is is a polystyrene spherical bead. The trapping force is generated when light refracts through the dielectric sphere, due to the difference in index of refraction between the sphere and surrounding fluid. The laser light carries momentum proportional to its energy and direction of propagation. When the light refracts and reflects through the dielectric sphere, the momentum of the photons changes. Conservation of momentum states that this must result in an equal and opposite momentum change, which gives rise to the trapping force.

Figure 2.2 shows a force balance on a trapped dielectric sphere, where the trapping laser has a Gaussian intensity profile. As can be seen in Figure 2.2.a, when the dielectric sphere is displaced from the center, the resulting momentum due to refraction attracts the bead back to the center. The radial force is referred to as the gradient force. In reality, the laser beam is focused, such as in Figure 2.2.b. The resulting momentum change in the axial direction, or scattering force, keeps the dielectric sphere in place slightly above the beam waist.

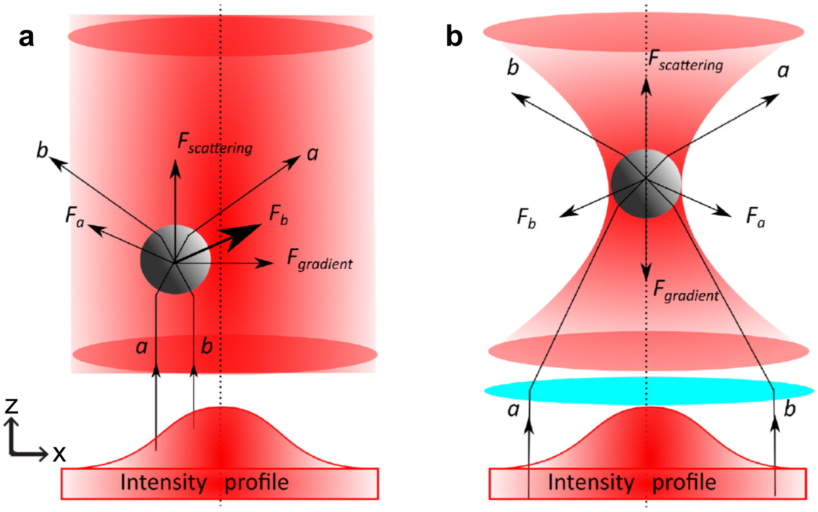

Figure 2.2: A force balance based on the ray optics explanation of the working principle of the optical tweezers, which is valid when the bead diameter is larger than the wavelength of the light. (a.) Unfocused laser with a Gaussian intensity profile. Two light rays *a* and *b*, where the intensity of *b* > *a*, refract through a bead. The change in momentum of the light ray *b* is larger than *a*, resulting in a net restoring force towards the center ($F_{gradient}$). There is also a net force in the axial direction, so the bead can not be hold in place. (b.) A focused laser beam can hold a bead in place by fixating the axial position. The bead stays slightly above (or below) the beam waist, where $F_{gradient}$ balances the force in the axial direction ($F_{scattering}$). Both pictures reprinted from [39].

For small displacements from the trap center, the trapping force can be described by Hooke's Law, as in Equation 2.1:

$$F_{OT} = \kappa_x d_x \tag{2.1}$$

where F_{OT} is the trapping force, typically 0.1 to 100 pN, κ_x is the trapping stiffness in pN nm^{-1} (see Section 2.2.2) and d_x is the bead displacement from the trap center (with a maximum of 150 nm).

The optically trapped particle undergoes random motion, due to thermal agitation, also called Brownian motion. Figure 2.3 shows a simulation done by Volpe et al. [40] on an optically trapped Brownian particle. In the simulation, the trapping stiffness in the x and y-direction is the same, resulting in a spherical probability density function in the x-y plane. Note that, in the set-up used for this thesis $\kappa_x \neq$

κ_y, and the probability density function in the x-y plane appears slightly oval. The set-up used for this thesis typically has an axial trapping stiffness 3.6 times smaller than the radial stiffnesses.

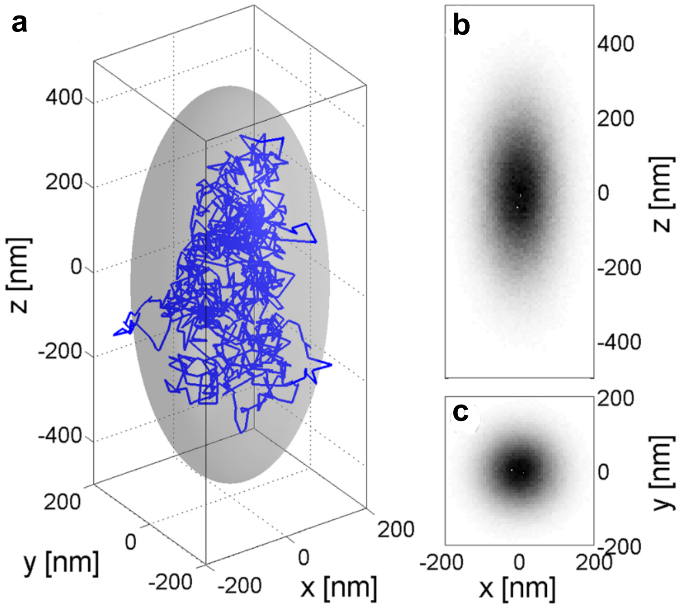

Figure 2.3: Simulated trajectory of a Brownian particle in an optical trap. Here, κ_x = κ_y = 1.0 x 10^{-9} pN nm^{-1}, and k_z = 0.2 x 10^{-9} pN nm^{-1}. The particle explores an ellipsoid space around the center of the trap, indicated by the shaded area in (a.), representing an equiprobability surface. Figures (b.) and (c.) show the probability distributions in respectively the x-z and x-y plane, that follow a two-dimensional Gaussian distribution around the trap center. Picture reprinted from [40].

2.2.2. Calibrating the trapping stiffness

The optical tweezers force is directly proportional to the trapping stiffness. So, in order to determine F_{OT}, an accurate estimate of the trapping stiffness (κ) must be made. The trapping stiffness is dependent on various factors:

- The laser emission. The experimentalist sets the power to be emitted by the laser. In this thesis, the power typically varies from 0.5-1.5 W.
- The bead size. The diameter of the bead is inversely proportional to the trapping power: $F_{OT} \propto 1/d_b$.
- The difference in refractive index between the surrounding fluid and the bead. The larger Δn_D, the more the light is refracted, the larger the trapping force.
- The microfluidic device. Surface contamination on the bottom of the microfluidic device can refract part of the laser light, resulting in less momentum transfer to the bead. The higher the position in the device, the larger the chance of surface contamination. The trapping stiffness decreases as a function of height in the device.

Since the trapping stiffness is dependent on factors out of control for the experimentalist, the calibration procedure for the stiffness is repeated prior to each measurement. Several methods have been reported for the calibration, amongst which this thesis highlights the variance method and analysis of the power spectral density. Other methods include applying an external force to the optically trapped bead, such as the Stokes drag, to deduce the trapping force [41, 42].

The variance method analyses the thermal fluctuations of the trapped bead. The equipartition theorem states that a particle in thermal equilibrium with its surroundings has an energy of $1/2k_BT$ for each degree of freedom. By computing the position variance in one direction, the trapping stiffness can be computed using the equipartition theorem as stated in Equation 2.2:

$$\frac{1}{2}k_BT = \frac{1}{2}\kappa_x\sigma_x^2 \tag{2.2}$$

where σ_x^2 denotes the variance in nm^2, κ the trapping stiffness in pN nm^{-1}, k_B the Boltzmann constant and T the absolute temperature in Kelvin. Equivalently, the variance (σ_y^2) and trapping stiffness (κ_y) are determined for the y-direction. In this thesis, the variance method is preferred over the other methods, due to its simplicity and independence on fluid viscosity [43]. Also, at low laser powers the equipartition method is found to be in good agreement with the existing alternative methods, although at higher laser power discrepancies become apparent [44].

The Brownian motion of a particle in an optical trap can be described by the Langevin equation. For particles in low Reynolds number fluids, the power spectrum of the Brownian motion is a Lorentzian function as in Equation 2.3:

$$E(f) = \langle|\tilde{x}(f)|^2\rangle = \frac{k_BT}{\pi^2\beta(f^2+f_c^2)} \tag{2.3}$$

where the trapping stiffness can be deduced from the corner frequency, or sometimes called the roll-off frequency :

$$\kappa = 2\pi\beta f_c$$

with

$$\beta = 6\pi\eta r_b$$

where η the dynamic viscosity and r_b the radius of the particle. At low frequencies ($f \ll f_c$) the spectrum reaches its asymptote $E(f) = \frac{4\beta k_BT}{\kappa^2}$, whereas it decays with $1/f^2$ for high frequencies. Examples of PwSD's can be found in, for example, Section 2.5.2. The integral of a spatial PwSD is equal to the position variance. The results are averaged using a moving average with an exponentially increasing window size.

2.2.3. Microrheology and optical tweezers

In this work, the optical tweezers are used as a microrheology tool to measure interfacial tension. The field of microrheology has been utilizing the optical tweezers for interface manipulation. Microrheology probes material response on micrometer length scales with microliter sample volumes: allowing for local measurements in inhomogeneous systems. Working on a small scale enables the study of rare or precious materials, such as biological samples or gels [45]. There are two broad classes of microrheology methods: those involving active manipulation of probes while monitoring their response or **active microrheology**, and those relying on the passive motion of particles due to Brownian Motion or **passive microrheology**. Traditionally, magnetic tweezers have been used in active microrheology since they can provide larger forces than optical tweezers. The magnetic tweezers can manipulate super-paramagnetic particles and uses video microscopy to measure the displacements. Nowadays the magnetic tweezers and the optical tweezers are widely used to study a wide variety of biological processes [46]. However, the magnetic tweezers have a lower temporal and spatial resolution than the optical tweezers [47].

Optical tweezers have been used to study particle behaviour near a variety of interfaces. Table 2.1 provides a short description of the existing research, including a graphical presentation of the alignment of the optical tweezers to the interface. From this table, it can be concluded that the main novelty in this thesis is the behaviour of the laser light passing through the two fluids, since the membranes studied typically have a thickness much less than the wavelength of the laser light. First, literature reporting on diffusivity near an interface or boundary is discussed. Lastly, the two academic endeavours have measured membrane interfacial tension using the optical tweezers are considered.

The diffusivity (D_0) of the spherical bead, far away from any boundary, can be determined by balancing the thermal kinetic motion with the viscous drag force. The Equation 2.4 is named the Stokes-Einstein relation:

$$D_0 = \frac{k_B T}{6\pi\eta r_b} \tag{2.4}$$

where D_0 the diffusion constant. Equivalently, the diffusion constant in a certain direction can be defined as a function of the position variance, as in Equation 2.5:

$$D_x = \frac{\sigma_x^2}{2t} \tag{2.5}$$

where t denotes the measuring time for the position variance σ_x^2. When the particle is in the vicinity of a solid boundary, the Brownian motion can be hindered and the diffusivity is expected to decrease [48, 49]. Yang et al. [48] report a decrease in parallel diffusivity of $0.4D_0$ at 1.2 particle radii near the solid boundary. Boatwright et al. [50] and Shlomovitz et al. [51] find that the parallel particle diffusivity increases near a free water-air interface, until a maximum of 1.3 D_0 at two particle radii from the interface.

In the above-mentioned papers the set-up has the laser of the optical tweezers perpendicular to the interface or surface and the bead is not actively perturbed. Shitamichi et al. [52] studied the mechanical properties of a liposome vesicle. The vesicle is deformed from the inside using two beads. Upon closing the access of the laser light, the surface relaxation dynamics are studied, and the interfacial tension and bending rigidity of the membrane can be extracted. Dols-Perez et al. [1] were able to trap a bead whilst penetrating a lipid bilayer, allowing for a mechanical characterisation of the membrane. In this case, the laser is oriented parallel to the membrane. Note that, in the latter two papers align the direction of propagation perpendicular to the laser orientation, since the laser trapping stiffness is lower in the parallel compared to the perpendicular direction.

Interface	Type	Graphical Illustration	Notes
Glass plate wall	Passive microrheology	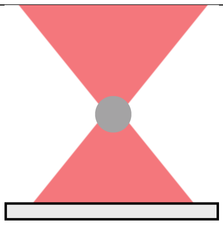	Schaffer et al. [49] used the optical tweezers to study passive fluctuations in a bead near a solid wall.
Water-air interface	Passive microrheology	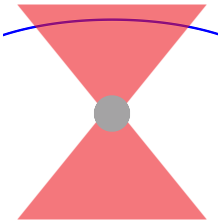	Boatwright et al. [50] and Shlomovitz et al. [51] studied the response function of a particle near a water-air interface to characterise the interface dynamics and mechanics.
Water-air interface, Langmuir monolayer	Passive microrheology	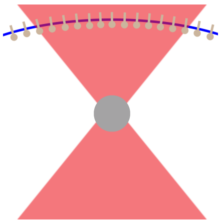	Shlomovitz et al. [35] measured the viscosity of a Langmuir monolayer with passive microrheology.
Spherical unilamellar liposome	Active microrheology	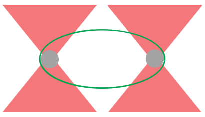	Shitamichi et al. [52] measured the mechanical properties of a vesicle from a lipid bilayer. The vesicle is deformed using two optical traps and the relaxation behaviour is observed.
Lipid bilayer membrane	Active microrheology	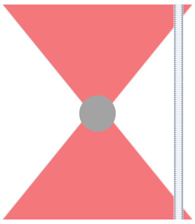	Dols-Perez et al. [1] pushed an optically trapped bead through a lipid bilayer, extracting its mechanical properties. An interfacial tension as low as $\gamma = 2.1 \times 10^{-6}\ \mathrm{N\,m^{-1}}$ was measured.

Table 2.1: Tabulated overview of existing interfacial microrheology research using optical tweezers and their laser orientations.

2.3. Experimental set-up

The interface is formed inside a microfluidic device, sometimes referred to as a flow cell: Figure 2.4.a shows a schematic of such a microfluidic device. There are three inlets of which two are used to insert the organic phase, or oil, and the aqueous phase, or the water-glycerol mixture. The channels of the microfluidic device are formed by the polymer Norland Optical Adhesive-81 (NOA-81), which is sandwiched between two microscopic glass slides (see Section 2.6). The two parallel channels in the device are connected by 21 rectangular apertures of 85 µm by 100 µm (y by z). The two fluids meet along the apertures to form the interface as in Figure 2.4.b. The x-direction is defined as the direction perpendicular to the interface, whereas the y-direction denotes the direction parallel to the interface. Beads are suspended in the aqueous phase.

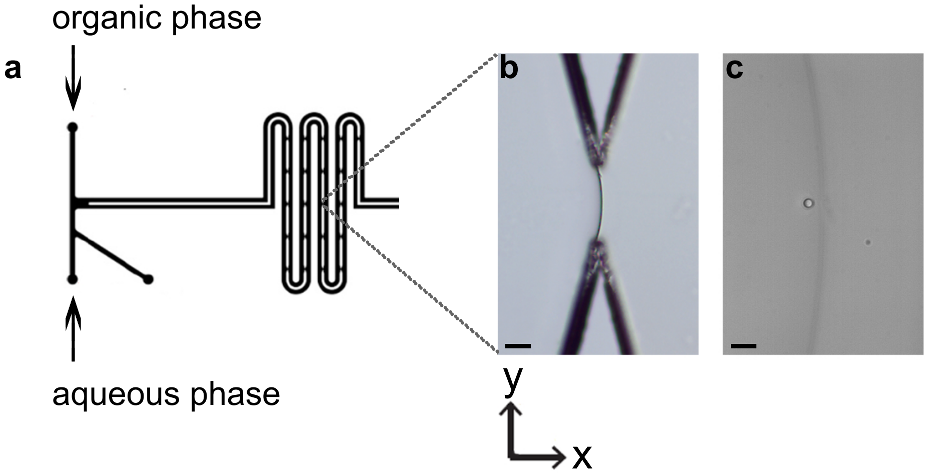

Figure 2.4: The interface is formed in a microfluidic device. (a.) Schematic of a microfluidic device, consisting of two parallel channels, connected by 21 rectangular apertures. Two of the three inlets are used to insert the organic and the aqueous phase. Picture adapted from [39]. (b.) The two fluids meet along the apertures to form the interface. Scale bar 20 µm. This interface is not index matched. (c.) An optically trapped bead near an interface. Scale bar 5 µm. This interface is not index matched.

The set-up for the optical tweezers is quite complex and contains many components. The relevant components are highlighted below and numbered as indicated in Figure 2.5.

(1.) **Trapping laser** at λ = 1064 nm. This high-power laser is used to trap the bead.

(2.) **Detection laser** at λ = 830 nm. Just as the trapping laser, this laser is focused on the bead. The light scattering behaviour, as the bead moves away from the focal point, is used for position detection.

(3.) **Piezoelectric stage**. A motorized piezoelectric stage is used to move the device relative to the trapped bead. The piezo electric stage can be moved in three dimensions, with nanometer precision.

(4.) **Position Sensitive Device** (PSD). The PSD sensor measures the two-dimensional position of the detection laser spot. The PSD output is an analog electric signal in voltage and a calibration is needed to extract the spatial dimensions (nm).

- **Regular and high-speed camera**. (not shown in figure) A regular Thorlabs camera is available for easy and quick observations. The high speed PCO camera can record for thousands of frames per second, allowing for high speed observation of the interface. The latter can also be used for post-processing purposes.

In the experiment, the piezo electric stage is moved such that the interface is pushed against the optically trapped bead. When the interface is pushed against the bead, *i.e.* a force is exerted on the bead, the bead is moved from the focal point. Figure 2.6 shows the bead at three different positions, indicating the nomenclature for the mentioned dimensions. In these three positions, the following three parameters vary:

- **Displacement**. The displacement denotes the position of the focal point relative to the interface. During the experiment, the interface is actuated by the piezo electric stage and so the interface moves in the eyes of the observer. However, in this thesis, a frame of reference moving with the microfluidic device is preferred. This means that the displacement refers to the position of the focal point relative to the interface. A negative displacement indicates that the bead is not touching the interface yet, whereas a positive displacement indicates that the bead has touched the interface. For example, at a displacement of $-r_b$, the bead starts to touch the interface.
- **Relative bead position (d_x)**. This denotes the position of the bead relative to the focal point. When the bead is not touching the interface, the bead is in the center of the focal point and $d_x = 0$. Note that a relative bead position in the y-direction (d_y) is also possible.
- **Actual bead position (z_b)**. The actual bead position is the displacement minus the relative bead position, or the bead position in the observer's frame of reference. This is mainly an important parameter for the model.

Figure 2.6.a shows the bead near the interface, but is not yet touching the interface. The displacement is −0.7 µm, $d_x = 0$ and z_b equals the displacement. When the bead touches the interface, such as in Figure 2.6.b, the three parameters start to vary. Here, the displacement 0.05 µm and d_x has increased to 150 nm. This means that the actual bead position is −0.1 µm. Figure 2.6.c shows a case exaggerated for illustrative purposes.

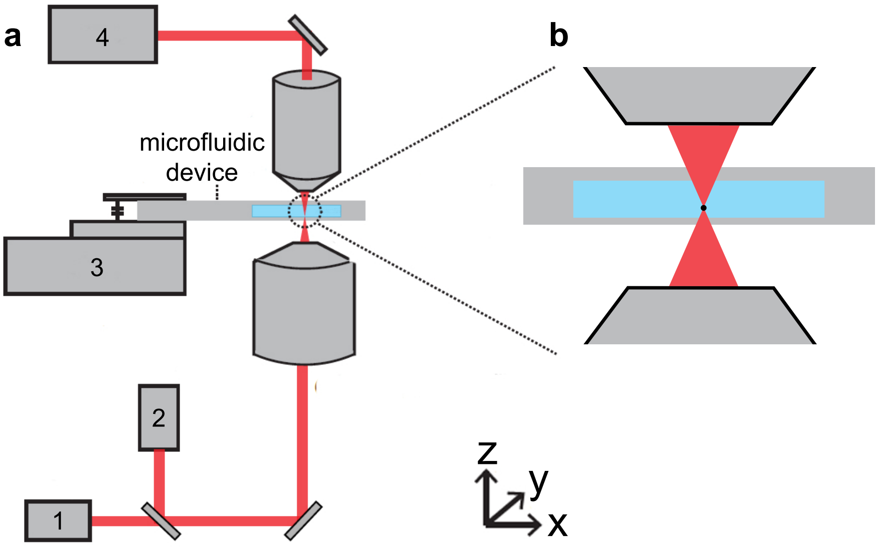

Figure 2.5: Schematic of the optical tweezers set-up. (a.) Light from the trapping laser (1) and detection laser (2) are focused by a high-quality regular microscope objective to trap the bead. The microfluidic device is moved with the piezo electric stage (3) to push the bead against the interface. The light of the detection laser scatters through the bead, through the condenser on to the position sensitive device (4). As the bead is pushed against the interface, it displaces from the focal point as well as the corresponding light spot on the PSD, measuring the position of the bead. Picture adapted from [53]. (b.) Zoomed in cross section of the microfluidic device and an optically trapped bead. The bottom objective is water immersed to increase microscope resolution. The condenser is oil immersed, but both immersion liquids have an index of refraction close to water. The bottom of the microfluidic device has a thickness of only 160 µm. Images not to scale.

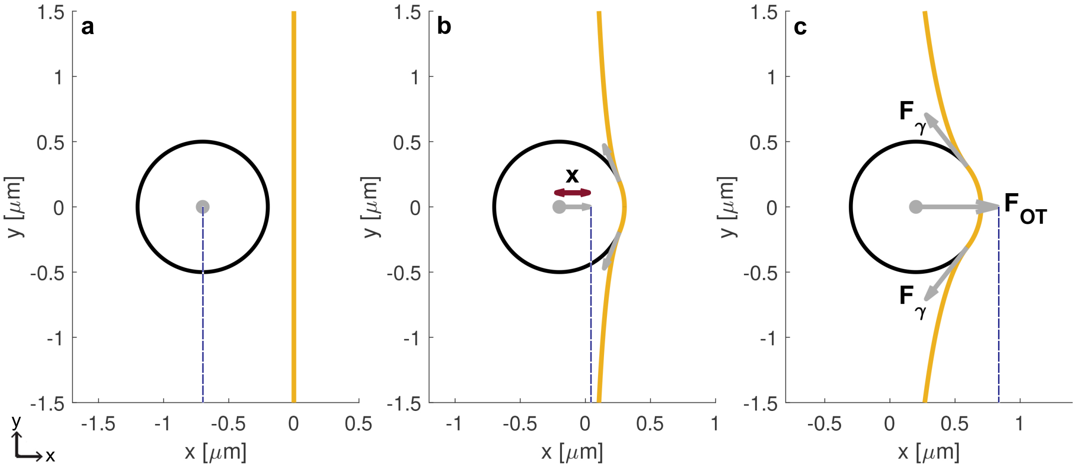

Figure 2.6: A schematic of three bead positions. The position of the focal point is denoted by the blue, dashed line. In the experiment, the focal point is displaced by a piezo electric stage. The distance from the focal point to the bead center is denoted by d_x and proportional to the trapping force: $F_{OT} = \kappa_x d_x$. (a.) At a displacement of −0.7 µm, the bead does not touch the interface yet, and x = 0 nm. (b.) At a displacement of 0.05 µm the bead touches the interface and the relative bead position increases: d_x = 150 nm. (c.) Force balance on the bead: the interfacial tension forces (F_γ) are balanced by the optical tweezers trapping force (F_{OT}).

2.4. Data processing

The obtained experimental data is analysed using five parameters, which can be found below. Typically, experiments in the optical tweezers are conducted with a bead suspension in water. To eliminate optical aberrations of the focal point as the bead approaches the interface, the refractive index of the aqueous phase needs to match the refractive index of the organic phase. This requires to add glycerol to the aqueous phase, which changes the viscosity of the aqueous phase and thus affecting the measurement time scale (see Section 2.5.2). Secondly, no literature is present on the laser behaviour in the presence of an interface between two fluids. In order to reliably measure the interfacial tension, the optical aberrations caused by the presence of the interface should be minimal. Section 2.5.3 analyses the laser behaviour in the presence of an interface.

Using a custom-built LabView program, the fluctuations of the bead are measured over either one or three seconds, with a sampling frequency of 50 kHz. The data is analyzed using the five characteristics explained below. The optical aberrations are expected to be dependent on the distance to the interface, thus the laser behaviour is probed by analysing the relative bead position, variance, eccentricity of the voltage and power spectrum near and far from the interface. In the case of optical aberrations, these parameters are expected to vary. At the positions where the bead touches the interface, the bead fluctuations are shown in scatter plots, together with the relative bead position. The latter is fitted to the Minimal Surface Model (Chapter 3) to extract the interfacial tension. The fitting procedure, as well as a short note on the sensitivity to the estimate of κ, is explained in Section 2.4.1.

- **Relative bead position.**
  The relative bead position, denoted by (d_x), is the position of the bead relative to the focal point. When calibrating the set-up, the detection laser and trapping laser are aligned such that $d_x = 0$. However, as the lasers propagate through the interface, they can refract differently, causing $d_x \neq 0$. As the calibration from the analog electrical signal to spatial dimensions is only valid for a certain domain, d_x should not deviate more than $\pm$ 150 nm from zero before touching the interface. The spatial parameters are computed in the direction perpendicular to the interface, or the x-direction, and the direction parallel to the interface, or the y-direction.

- **Position variance.**
  The position variance is an important parameter as it provides us information about the laser momentum transfer to the bead as well as the beads mobility upon touching the interface.
  The variance of the bead position (σ^2 in nm^2) is the average of the squared difference from the mean, as in Equation 2.4:

  $$\sigma_x^2 = \frac{1}{N}\sum_{i=1}^{N}(d_{x_i} - \mu_x)^2 \tag{2.6}$$

  where N denotes the number of samples, and μ_x denotes the average value of d_{x_i}. Equivalently, the position variance in the direction parallel to the interface is denoted with σ_y. When the bead is far from the interface, the position variance is directly proportional to the trapping stiffness (κ_x) via the equipartition theorem, Equation 2.7:

  $$\sigma_x^2 = \frac{k_B T}{\kappa_x} \tag{2.7}$$

  where k_B denotes the Boltzmann constant and T the absolute temperature. Upon approaching the interface, when the stiffness of the interface becomes significant in κ_x, or equivalently the diffusivity decreases, the variance is expected to decrease.

- **Eccentricity of the voltage on the PSD.**
  The coordinates of the bead position relative to the trap center follow from two voltage signals on the position sensitive device (PSD). The signals are converted to spatial dimensions through a calibration procedure, which is roughly linear. It is noted that the PSD is mounted under an angle of 45°. The raw voltage data is analysed before conversion to prevent calibration biases, in case of contamination of the device or interface. The signal is analyzed by computing the eccentricity and orientation. Figure 2.7 shows an exemplary voltage reading for 150000 points, measured

over three seconds. A multivariate normal distribution is fitted to the dataset by computing the covariance matrix. The eigenvectors and eigenvalues of the matrix correspond respectively to the direction and length of the distribution. The eccentricity (e) is a function of the length of the minor axis (Λ_1) and the major axis (Λ_2) as in Equation 2.8:

$$e = \sqrt{1 - \left(\frac{\Lambda_1}{\Lambda_2}\right)^2} \tag{2.8}$$

The orientation (ϕ) is the angle of the major axis with the horizontal axis where $[-\frac{\pi}{2} < \phi < \frac{\pi}{2}]$.

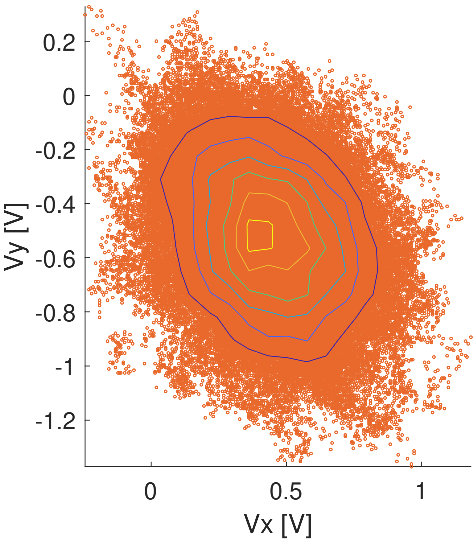

Figure 2.7: Example of scattered voltage set as measured directly by the PSD. Each orange dot represents a measurement for the bead position, where V_x and V_y are measured simultaneously. e = 0.84, ϕ = $-\pi/4$. Ellipsoid contour lines of the covariance matrix are also plotted. The sampling time was three seconds, recording a total of 150000 points.

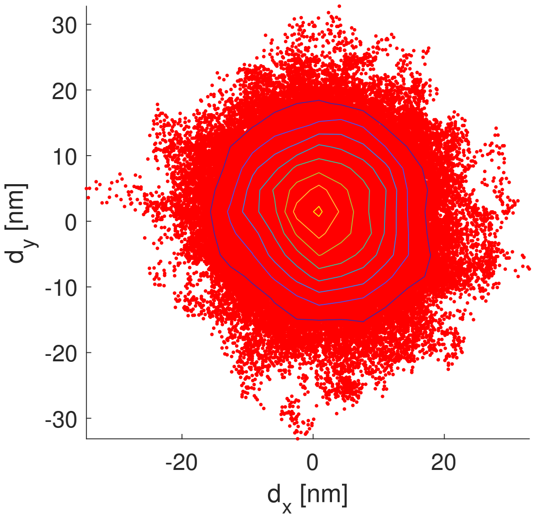

Figure 2.8: The PSD signal in voltage from Figure 2.7 converted to spatial dimensions using the calibration method. Each red spot denotes a measurement for the bead position.

- **Power spectral density.**
  The power spectral density (PwSD) can be used for calculating the stiffness as well as observing the influence of noise. The spectrum is obtained by computing the Fourier transform of the voltage variations or the spatial data.

  An example of a PwSD is given in Figure 2.12, where it can be seen that the cut-off frequency for the viscous liquid is much lower than for purely water, indicating a lower diffusivity. By computing the PwSD, an estimation of the contribution of noise to the variance can be made. The results are averaged using a moving average with an exponentially increasing window size.

- **Scatter plot of position data at the interface.**
  When the bead is starts to interact with the interface - which is when $\langle d_x \rangle$ rapidly changes - the interfacial tension can be estimated using the model. In order to visualize the bead-interface interaction, the spatial data points are shown in a scatter plot, as in Figure 2.8. Far away from the interface, the scatter plot is expected to have e close to zero, *i.e.* appear circular, as in Figure 2.8. Upon touching the interface, the scatter plot is expected to change shape.

2.4.1. Fitting the model to the data

If the mentioned parameters are minimally varying we have minimal optical aberrations. If the position variance is decreasing upon touching the interface, we expect a good measurement of the interfacial tension. This section describes how to deduce the interfacial tension from a successful experiment.

Since it has not been possible to push the bead through the interface, but merely indent the interface, a model is needed to deduce the interfacial tension. The experimental results for the relative bead position (d_x) versus the displacement of the focal point, together with the estimate for the trapping stiffness, result in a force curve. Figure 2.9.a shows an exemplary d_x vs. displacement curve. The black, dashed line denotes the expected behaviour if the bead were to touch a completely rigid interface. In this case, Δx = Δdisplacement and the interfacial tension can not be deduced. It can be seen that the experimental data has a lower slope, so the interface is expected to be indented. Figure 2.9.b shows an exemplary force curve. The actual bead position is plotted on the x-axis, which is equal to the displacement minus the relative bead position. The optical tweezers are reported to have a linear stiffness up to 100 nm distance from the trap center.

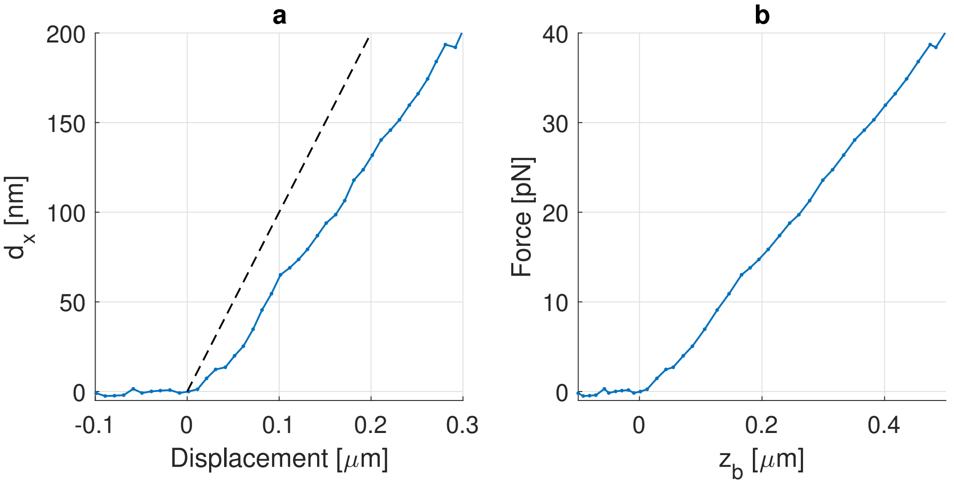

Figure 2.9: An exemplary force curve for an estimated stiffness of 0.2 pN. (a.) The raw experimental data. At displacement = 0 µm the bead touches the interface and is moved away from the focal point of the trap. The black, dashed line denotes the line where Δd_x = Δ displacement, or as if the bead were to be pushed against a solid wall. (b.) The force curve for the data in (a.).

The interfacial tension is extracted by fitting the experimental results with the model. The input for the model is a set of actual bead positions and interfacial tensions. By calculating the equilibrium forces, the model determines the values of d_x, κ and the position of the focal point. A full explanation of the Minimal Surface Model can be found in Chapter 3. First, a linear fit is made to the x-displacement data, indicated by the dotted, red line in Figure 2.10.a. The linear fit is made using the MATLAB function *polyfit*, between the first measurement point after displacement = 0 µm and the point where d_x = 100 nm. The model computes for the experimental estimate of the stiffness the interfacial tension as a function of the slope of the d_x vs. displacement curve, as in Figure 2.10.b, denoted by the asymptotic curve. The model is computed for several values, denoted by the small dots in Figure 2.10.b. The intersection between the asymptotic curve computed by the model and the vertical line, denoting the experimental outcome, indicates the estimate for the interfacial tension. In Figure 2.10.a, the slope of the linear fit is 0.66. In Figure 2.10.b, this corresponds to an interfacial tension of 4.2 x 10^{-4} N m^{-1}.

2.4.2. Sensitivity

The optical tweezers have an excellent spatial and temporal resolution. The piezo electric stage can be moved with an accuracy up to one nanometer. However, our estimate of the trapping stiffness using the equipartition method is quite inaccurate and can deviate up to 20% from other methods [39]. We compute Figure 2.10.b for the estimated κ_x ± 20 %. The result is shown in Figure 2.11. We find that γ = 3.4 and 4.9 × 10^{-4} pN nm^{-1}, which is also about ± 20% from our earlier estimate of γ. As we were unable to obtain validation measurements on our exact fluids properties, *f.e.* using spinning drop tensiometry, these margins are already below our resolution.

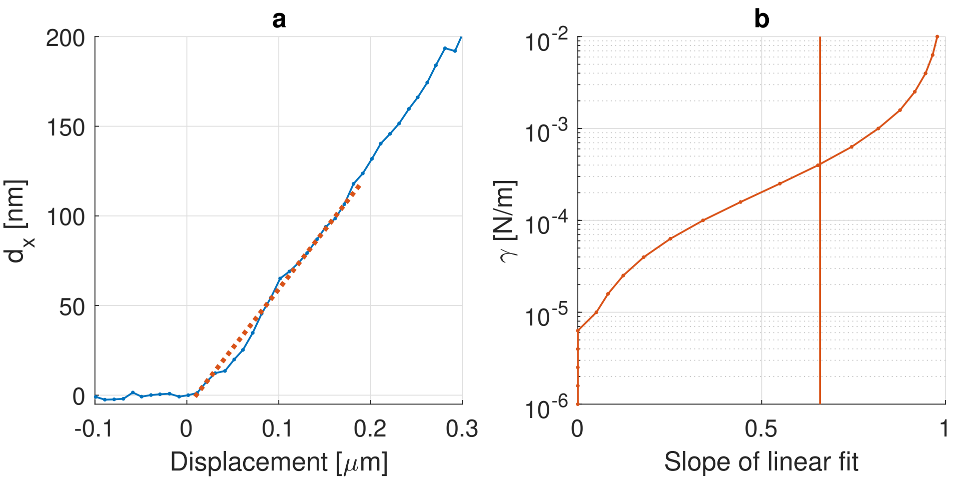

Figure 2.10: Fitting of the model to the experimental data. (a.) A linear fit is made to the experimental data. The fit is denoted with a red, dotted line. (b.) The curve denotes the slopes for the experimental estimate of κ_x, for various interfacial tensions. The slope for the line fitted in (a.) is 0.66, which provides an estimate for γ of 4.2×10^{-4} pN nm^{-1}.

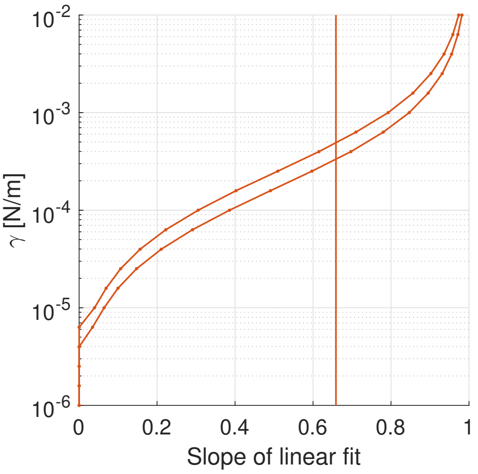

Figure 2.11: The data from Figure 2.10.b with the estimate of $\kappa_x \pm 20$ %. We find that γ = 3.4 and 4.9×10^{-4} pN nm^{-1}, which is an acceptable range for our experiments.

2.5. Design of experimental parameters

2.5.1. Estimating the index of refraction

The refractive index describes how fast light propagates through a medium. n is a dimensionless number, defined as the speed of light in vacuum over the phase velocity, or the light rate of propagation through a medium. At the interface, the difference in refractive index determines the refraction as well as the amount of light that is reflected. In this thesis the difference in refractive index between the organic and the aqueous phase should be small enough so that the working of the optical tweezers is not opposed.

The refractive index (n) is a material property and strongly dependent on the wavelength of the incident light (λ) as well as temperature. The symbol n_D denotes n in the middle of the visible spectrum, or at the so-called sodium D-line: λ = 589 nm. The set-up has two lasers at different wavelengths: the detection laser at λ = 830 nm, and the trapping laser, at λ = 1064 nm.

Appendix B discusses the reported values for n for the aqueous phase, being a mixture of water and glycerol, and for the organic phase, consisting mainly of the oil dodecane. There are no exact literature values present for our wavelengths. Since it has been observed early in the thesis that optical trapping is still possible with a difference as large as Δn_D = 0.015, the matching of the refractive index focuses mainly on the detection laser to ensure accurate position detection. The temperature in the lab is climate controlled at 20 $\pm$ 1°C.

Table 2.2 shows an overview of the obtained values for n, from the literature. For water and glycerol, the values as experimentally determined are chosen, instead of the estimates. Also, glycerol and dodecane seem to have a similar difference for n_D and n at λ_{830}. This is not the same for water.

If we were to index matched based on these literature values, a mass fraction of 61.4 wt% glycerol would be needed to index match the dodecane at λ_{830}. As can be seen later on in the thesis, in Section 2.5.3, the bead is not properly trapped.

The fifth column in the table shows the measured values of n_D for the fluids used in the experiments. It can be seen that the values obtained for water and dodecane are reasonably close to the reported literature values. The value for glycerol is significantly less. Glycerol is hygroscopic, thus it is hypothesised that the stock of glycerol might have absorbed water from the air over time, or is otherwise contaminated, reducing n_D.

It is concluded that index matching in the near infrared is not trivial. Prior to each experiment n_D is measured and matched using a regular Abbe refractometer. Later in the thesis we will conclude that matching the index using n_D does not provide good results.

	n_D literature	est. of n at λ_{830}	$n_D - n_{830}$	n_D experimental
water	1.3334	1.3287	0.0047	1.3333
glycerol	1.4746	1.467	0.0076	1.4722
dodecane	1.4216	1.4136	0.0080	1.4218

Table 2.2: The refractive indices n for the main fluids. The experimentally obtained n_D is measured using a regular Abbe refractometer, using a white light source.

2.5.2. Trapping behaviour in aqueous glycerol

The use of glycerol also changes the difference in index of refraction between the bead and surrounding fluid, changing the trapping stiffness and possibly the accuracy in the position sensing, since this is done by acquiring the scattered light.

Typically, the optical tweezers are used in solutions with similar rheology as water. For this thesis, the aqueous phase is a mixture of water and glycerol. Table 2.3 displays the difference in properties between the two mixtures. The trapping behaviour is probed in a device containing just one fluid, either water or the aqueous glycerol. Three data sets for the water device are compared to four data sets for aqueous glycerol.

Figure 2.12 shows the PwSD for both systems, in both directions. The difference in mobility in x and y direction seems to be larger for the aqueous glycerol mixture compared to the pure water. Secondly, as expected, the cut-off frequency is much lower for viscous aqueous glycerol, indicating a lower trapping stiffness as well as a lower diffusivity. Table 2.4 summarizes the measured trapping stiffnesses and eccentricity of the voltage plot, for both systems. The standard deviation for κ_y and the eccentricity appears to be much larger for the aqueous glycerol. Figure 2.13 shows the PwSD for the four data sets for the aqueous glycerol. High frequency noise seems to be significant in two of the data sets, contributing to a larger position variance.

Property	Water	Water-Glycerol (67% wt)
Dynamic viscosity (20 °C)	1.002 mPa s^{-1}	18.32 mPa s^{-1}
Index of refraction (λ = 587.56 nm)	1.333	1.426

Table 2.3: Viscosity and index of refraction for a typical working fluid (water) and one of the fluid mixtures used in this thesis. The index of refraction of the polystyrene beads is n_D = 1.587.

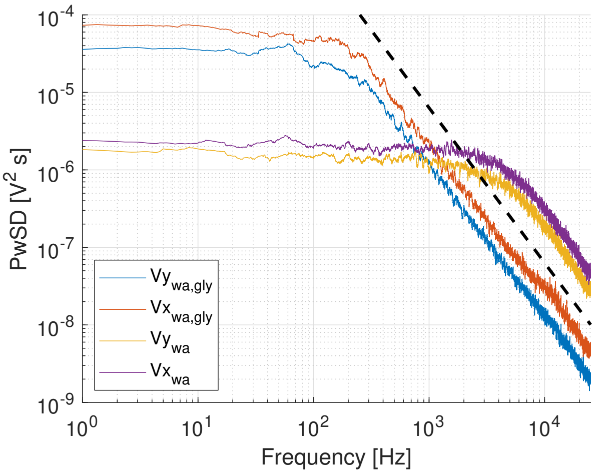

Figure 2.12: Power Spectral Density (PwSD) for a bead in water and water-glycerol (67% wt) mixture. The dashed line denotes $1/f^2$. F$_s$ = 50 kHz, sampling time 3 seconds.

Property	Water	Water, 67% wt glycerol
κ_x [pN nm^{-1}]	0.2437 ± 0.0047	0.1588 ± 0.0049
κ_y [pN nm^{-1}]	0.2868 ± 0.0023	0.1568 ± 0.0100
Eccentricity	0.4193 ± 0.0020	0.5303 ± 0.0620

Table 2.4: Tabulated values for the trapping stiffness κ_{OT}, obtained via the equipartition method, and the eccentricity for the analog voltage signal on the Position Sensitive Device. For water N = 3, for the mixture N = 4.

2.5.3. Trapping near an interface with large Δn_D

Optical trapping is also possible when the difference in index of refraction appears to be large. Figure 2.14 shows the development of the relative bead position and variance when the difference in index of refraction for λ = 589 nm is Δn_D = 0.007. Figure 2.15 shows the appearance of the bead at different positions, denoted by the letters in Figure 2.14. The appearance changes visibly from e or ≈ 35 μm distance to the interface. Figure 2.16 shows that the voltage data fits a normal distribution, despite the clear optical aberrations.

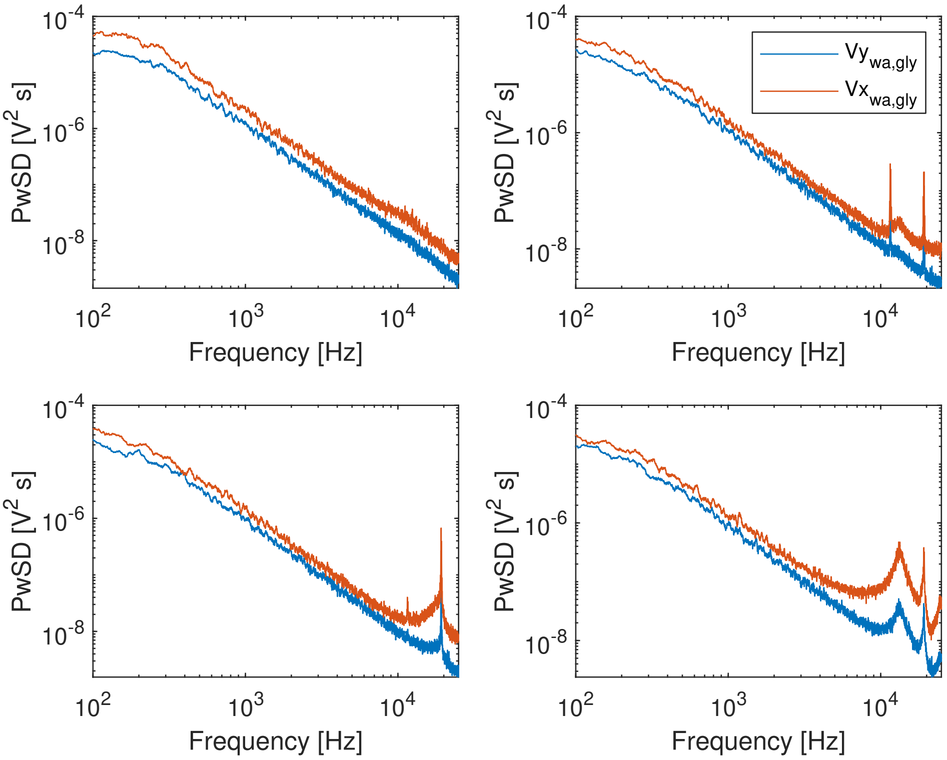

Figure 2.13: Centered Power Spectral Density (PwSD) for a bead in water-glycerol (67% wt) mixture. The bottom two spectra show significant high frequency noise, decreasing the accuracy of the measurement. F_s = 50 kHz, sampling time 3 seconds.

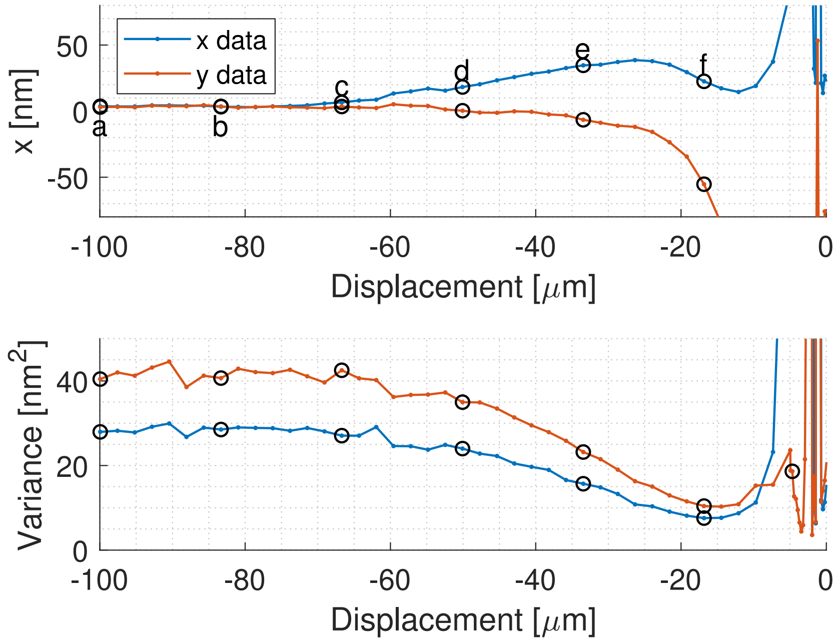

Figure 2.14: The bead position relative to the focal point (d_x) for an interface with a significant difference in index of refraction.

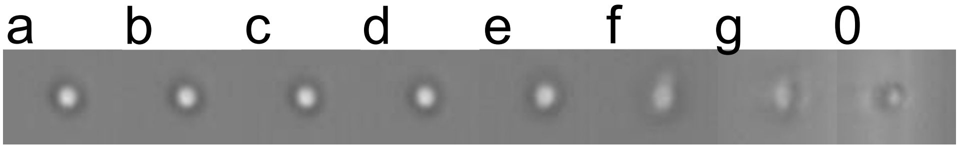

Figure 2.15: Pictures from the bead at the circles positions in Figure 2.14 and touching the interface.

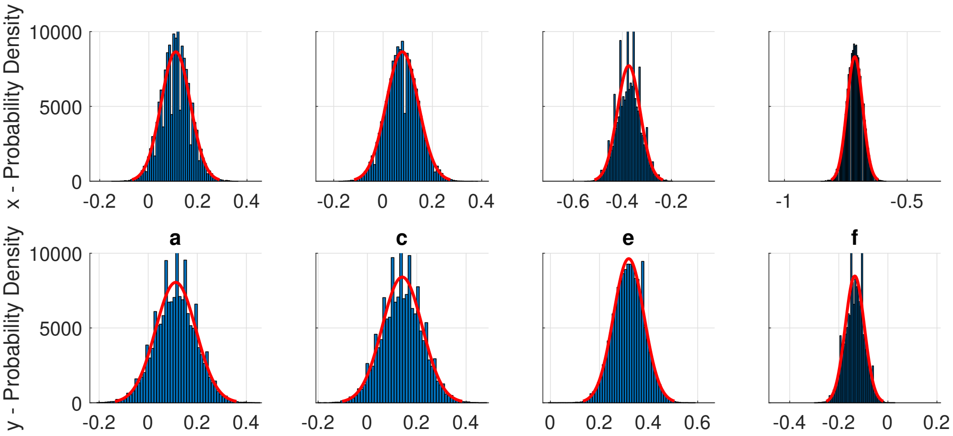

Figure 2.16: The voltage data for the four indicated positions fits a normal distribution, even when there are clear optical aberrations as in e and f.

2.6. Materials & methods

This section details the experimental procedures involved, including the manufacturing of the microfluidic device, the preparation of the liquids and handling the optical tweezers.

A typical experiment starts with a microfluidic device, prepared and cleaned as described in Section 2.6.1. A printed guide is taken into the lab, where the intermittent and end values of interest are noted down. The device is finished by glueing lasercut PMMA inlets to the device using NOA-81. The inlets guide a microfluidic tube, that is used to insert the fluids. The tube is also glued into the inlets using NOA-81, to be able to build up pressure in the device, if needed. Next, the liquids that are prepared according to Section 2.6.2 are put in an 1 mL plastic syringe. Using a syringe pump with a 1 mL BD Microlance 3 needle, the fluids are pumped into the microfluidic device. Since the NOA-81 is hydrophobic, the flow rate for the organic phase is typically two times larger than the aqueous phase. Preferably, a low flow rate of about 0.4 µL is used. However, this is dependent on each experiment, since the flow rates are adjusted so that mixing is minimal. The interfaces will form at random along the 21 apertures that the microfluidic device has. The success rate is dependent on the combinations of fluids used, but is on average 5 interfaces. It has never occurred that no suitable interface has formed. The device inlets and outlets are closed using NOA-81. Span-80 is known to have an adsorption time in the order of 10 minutes, so the device is rested for a minimum of 20 minutes prior to the experiment [54]. After resting, a regular microscope is used to examine the location of the formed interfaces and the quality of the interfaces. This is noted down per interface on the printed guide. Next, the device is taken to the optical tweezers and the setting up the experiment is finished per Section 2.6.3.

2.6.1. Device preparation

A typical microfluidic device is fabricated from an externally produced SU-8 2075 photoresist layer on a silicone wafer, see Figure 2.17.a. This high quality and expensive mould is not used to produce the devices directly, but a second, flexible and cheap mould is made from the organosilicone polydimethylsiloxane (PDMS) (Figure 2.17.b). We use a 1:10 ratio of curing agent and corresponding elastomer base (SYLGARD® 184, Sigma Aldrich). This ratio results in a device that is flexible, but not too frail and strong but not too brittle. The mixture is poured over the SU-8 mould and put under low pressure multiple times in a desiccator until bubbles form no longer. The bubbles change the shape and resilience of the PDMS mould, so it is preferred to remove them completely prior to curing. The PDMS mould is then polymerised in a regular convection oven at 80 °C for 1.5 hours. The SU-8 mould and the PDMS mould should be handled with care, since small damage at this stage can be disastrous for the quality of the device.

The PDMS mould is used to make the microfluidic device from an ultra-violet curing liquid adhesive: Norland Optical Adhesive 81, referred to as NOA-81 (Figure 2.17.c). The NOA-81 is poured onto the PDMS mould and air bubbles are removed using pasteur pipettes. All air bubbles should be carefully removed, since their presence will interfere with the formation of the interface as well as the position resolution. For rigidity, a thoroughly cleaned thick microscope glass side is added (Corning Incorporated, 75 mm × 24 mm). The cleaning process for the microscope slides is explained later in this section. The NOA-81 is cured under ultraviolet light (λ = 340 nm, 36 W) for 5 minutes. The NOA-81 is separated gently from the PDMS mould and covered with tape. Next, holes for the inlets and outlet (1.2 mm) are drilled using a regular drill. While drilling, there is a constant flow of demineralised water to carry dirt away. The drilling is done from the NOA-81 side. The drilling process is one of the main sources of dirt particles in the device, sometimes leading up to a congestion in the inlets or outlet. After the drilling, the device is cleaned using compressed nitrogen and carefully examined by eye for residual dirt. If needed, dirt is removed using no-residue tape.

The final step in finalising the microfluidic device starts with a thin microscopic plate (Menzel-Glazer, 60 mm x 24 mm (No. 1.5) with thickness of 170 ± 5 µm) that is spincoated with a thin layer of NOA-81 (≈ 3 µm) (Figure 2.17.d). This layer is partially cured under UV-light for about 30 seconds, so that the NOA-81 is thick enough to be able to form square channels, but sticky enough to cure to the other half of the device. The partially cured, thin slide with NOA-81 is put on to the rest of the device with extreme care. With a plastic Eppendorf tube, having a round end, the two parts are pushed together. The device is cured for another 10 minutes under UV light. Lastly, the device is finished overnight by curing on a hotplate at 80 °C. When the device is to be used, pure ethanol is flushed through as a last cleaning step. Using a low flow rate of compressed nitrogen, most of the ethanol is removed. The device is put on a hot plate at 80 °C for 1 hour to evaporate the remaining ethanol.

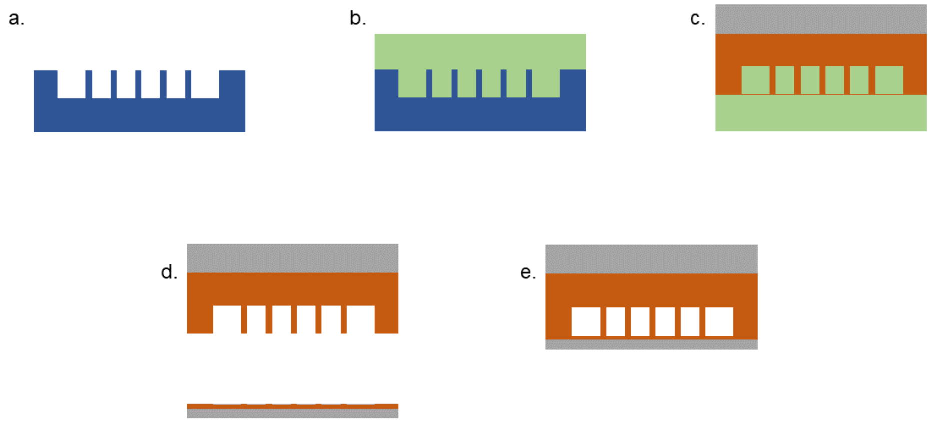

Figure 2.17: Overview of the manufacturing procedure for a typical microfluidic device. (a.) An SU-8 pattern (blue) on a silicone wafer provides the channel lay-out. (b.) The polymer PDMS (green) is used to fabricate a mold from the wafer. (c.) The NOA-81 (red) is poured on to the PDMS mould and a microscope slide (grey) is added for rigidity. (d.) NOA-81 is spin-coated on a very thin microscope slide. (e.) The parts are combined to form a closed microfluidic device.

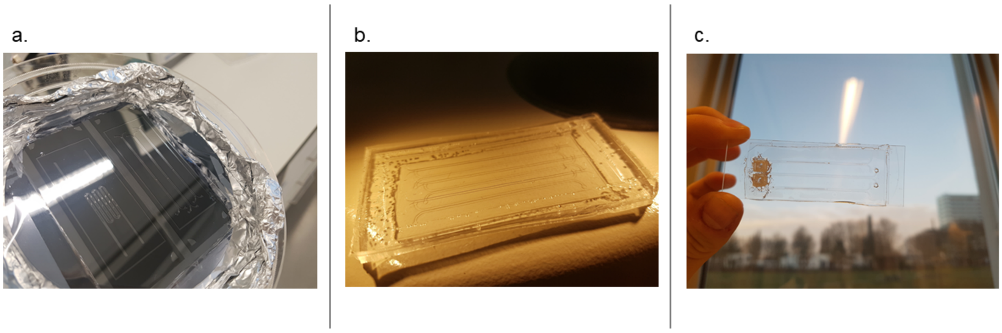

Figure 2.18: Pictures of the manufacturing steps. (a.) An SU-8 mould on a silicone wafer. (b.) A PDMS mould. (c.) A microfluidic device with inlets.

The cleaning of the microscope slides should be done thoroughly. The presence of microscopic dirt will prevent the NOA-81 from bonding properly to the glass, and, more importantly, it interferes with the lasers. This procedure starts with putting the both types of microscope slides in a beaker with demineralised water and $\approx$ 5 mL strong detergent (Hellmanex III, Sigma Aldrich). The beaker is closed using parafilm and put in an ultrasonic bath for 20 minutes after which the slides are rinsed ten times using fresh demineralised water. Then, the slides are put in the same beaker, but with fresh demineralised water, and put in the ultrasonic bath for another 20 minutes. Lastly, the slides are rinsed ten times again with demineralised water and blown dry using pure compressed nitrogen. The slides are stored in air-tight plastic tubes, typically used for centrifuging. Before using the slides to make the microfluidic device the last surface impurities are removed in a plasma cleaner, which enhances the bonding of the NOA-81 to the glass slides. The sample is put in the plasma cleaner, and a vacuum pump brings the chamber to a low pressure of at least 150 mTorr. Then, the room is flushed with pure oxygen, whereafter the pump brings the chamber to again at least 150 mTorr. Then, the plasma is turned on: the ionized gas flows in the chamber. This treatment removes very fine dirt and leaves no residual.

2.6.2. Liquids preparation

An interface is formed between the two phases: an aqueous phase and an organic phase. The organic phase contains dodecane (Sigma Aldrich) and the surfactant sorbitane monooleate or commercially known as Span-80® (obtained from Sigma Aldrich). The aqueous phase consists of ultra-pure MilliQ water, glycerol ($\geq$ 99.5 %, Sigma Aldrich) and, dependent on the type of experiment, a concentration of sodium dodecyl sulfate (SDS). The SDS is available in powder form (Sigma Aldrich).

The liquid preparation follows the experimental plan as described in the beginning of this chapter. It starts with an Eppendorf tube on a micro-balance, where a small quantity of Span-80 is weighed (≈ 0.06 µg). Since it is experimentally difficult to dispose such a small volume, a large deviation is found in the starting mass. From the value of the added mass of Span-80 and the desired concentration of the surfactant (0.05 w/w %) the needed mass of dodecane can be calculated. The mixture is vortex mixed for 30 seconds. If the experiment matches the index of refraction in the visible light, a volume of about 2 µL of the aqueous phase is made, consisting of 67 wt% glycerol. Using a regular Abbe refractometer, the index of refraction of the two mixtures a measured. The index of refraction of the aqueous phase will be slightly lower than the index of refraction of the organic side, and very small volumes of glycerol are added until the index of refraction of the organic phase is matched.

Parallely to this, a fresh batch of beads is prepared. 5 µL is micropipetted from the cooled polystyrene bead solution (Polybead) and diluted with 45 µL MilliQ water. First, this mixture is put in the ultra-sonicator for 10 minutes to break up possible clumped bead clusters. After vortex mixing for 30 seconds, this mixture is centrifuged at 6700 rpm. A high concentration of beads has formed at the bottom: 4 µL is pipetted out and washed again. The procedure is repeated two times more to further wash the surfactants from the bead. Lastly, dependent on the bead diameter the solution is diluted, see Table 2.5. For example, if a bead solution with 2 µm beads is prepared, the pure solution is diluted in two steps. First, 4 µL of the concentrated bead solution if diluted with 1 mL of MilliQ (ratio 1:250). Then, from this mixture 1 µL is taken and diluted with 1 mL of MilliQ to obtain a final dilution ratio of 1:25,000.

Bead Diameter	Final Dilution
1 µm	1:100,000
2 µm	1:25,000
5 µm	1:5,000

Table 2.5: Dilution ratio's for different bead diameters.

2.6.3. Setting up the optical tweezers

Lastly, an acousto-optic deflector (AOD) is used to move the trapping laser relative to the detection laser. Starting an experiment takes roughly four steps. The first step has to be done only once, but the other three are done prior to every measurement. For every step the virtual instrument (VI) that is used, made using program Labview, is listed. All VI's are provided by the lab.

- Upon warming up the laser, the set-up can be started. The Krohn-Hite filter is set to a Nyquist frequency of 24.5 kHz and a gain of 10 dB. The power emission is set in the laser, typically either 20% emission which equals 0.5 W, or 30% emission which equals 1.8 W. For the maximum trapping stiffness the amplification is set to 2.2 mW (see Appendix C, Figure C.1) and the frequency to 26 MHz for both channels. For measurements with a very low stiffness the amplification is set to 0.7 mW and 20% emission.
  VI used: *001_ DVE_ control.vi*

- Alignment of detection laser and trapping laser.
  Using the AOD, a trapped bead is swept through the detection laser focus point. The center of the detection laser is aligned with the center of the trapping laser. Major adjustments are made directly to the PSD mount and minor adjustments are made using a digitally steered mirror. The alignment is accurate when the signals in the two directions align with the center of the detection laser as in Appendix C, Figure C.2.
  VI used: *002_AOD-2Waysweep.vi*

- Voltage to nanometer calibration.
  This step calibrates the analog voltage output from the PSD with the spatial movement from the bead. Using the AOD, a grid is scanned of known spatial dimensions. The grid dimensions are set to have 20x20 points, with a size of 0.016 MHz (about 20 nm). A fifth order polynomial is fit to the PSD output after scanning for a complete conversion from voltage to nanometer. During this step the variance is also probed, providing a trapping stiffness in two directions.

The following conversion coefficients were used:
AODtonmx = 1286.00 nm/MHz; AODtonmy = 1278.40 nm/MHz
VI used: *Variance_shared_singlerun_psd2.vi*

- Data Acquisition.
  After starting up the piezoelectric stage and the interface is brought to touch the bead. The VI that is used records the bead fluctuations, or Brownian motion, per bead position. The VI is set to acquire at 50 kHz. When the bead is further than ~1 µm the step size is coarse: 5 µm. When the bead is near the interface the step size is decreased to be 10 nm.
  VI used: *axispiezomvtPSDrawdataWithOldAcqFunction.vi*

3

The Minimal Surface Model

The model uses the principal of a minimal surface, in this case a catenoid, to compute the interface expansion as the bead pushes the interface. The force exerted by the interface on the bead is used to compute the interfacial tension. The basics are explained in Section 3.1. Results are derived for the main parameters which are used to extract a value for the interfacial tension from the experimental results. The model has been originally developed by dr. D.S.W. Tam and dr. G.J. Amador. An overview of the adaptations made by the author of this thesis can be found in Appendix D.

3.1. Working principle

The interface minimises its exposed area due to interfacial tension, which is why we assume that the interface takes the shape of a minimal surface. We have developed a model that determines the shape of the surface as the spherical bead is pushing the interface. There are two parts to the geometry of the surface: a spherical cap, where the interface wraps around the bead, and a minimal surface between the bead and aperture. For the spherical cap, we assume no interaction between the bead and the interface. This assumption is two-fold: there is no wetting of the bead, *i.e.* no three-phase contact line is formed, and other attractive or repulsive forces between the bead and interface are negligible. Secondly, we assume the pressure in both channels in the microfluidic device, *i.e.* on both sides of the interface, to be equal. Recalling the Young-Laplace equation, Equation 1.2, this interface should have zero-curvature. Such a minimal surface, having zero curvature, is named a **catenoid**.

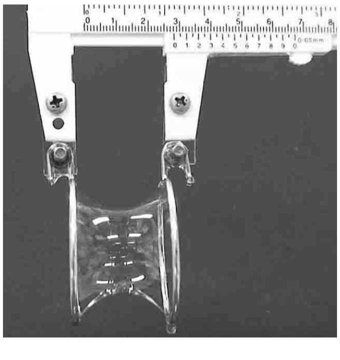

Figure 3.1: A soap film minimizes it interfacial area to form a catenoid shape. Picture reprinted from [55].

The catenoid shape is obtained by rotating a catenary curve (as in Equation 3.1) around its base. The parameter b determines the width of the catenary. Figure 3.1 shows a physical example of a catenoid: this minimal surface is formed when a soap film is spanned between two rings, where both sides of the film are exposed to ambient pressure, causing a zero-curvature surface. As the rings are moved further apart, b increases.

$$h = b\ cosh\left(\frac{x}{b}\right) \tag{3.1}$$

Recalling Section 1.1, the resulting free energy of an interface is γA. In the case of our model we can write the free energy as the sum of A_{cat} and A_{sphere}. We need to minimise this sum to obtain the geometry of the minimal surface (Section 3.2). We define an angle θ that determines the interface wrapping around the bead and thus the geometry of the catenoid. So, the free energy to minimise is: $\gamma\left(A_{cat}(\theta) + A_{sphere}(\theta)\right)$. We define the coordinate of the bead center z_B. For different values of z_B, the shape of the minimal interface is computed. From the resulting interface expansion (dA) we deduce the resulting interfacial tension force ($F(z_B)$) , as can be read in Section 3.3.

3.2. Computing the shape of the interface

For an input of various bead positions (z_B), the minimal surface is determined. Figure 3.2 shows an example for z_B = 0.5 µm. The interfacial area that wraps around the bead (A_{sphere}) is denoted by the blue line, where the red line denotes the part of the interface that forms a catenoid. The yellow circles denote the points between which the catenoid is formed. The catenoid is formed between a point far away, [0, R_{aper}], indicating the edge of the aperture, and a point on the bead: [$x(\theta)$, $y(\theta)$]. The dotted line denotes the angle θ with the horizontal, where θ is defined anti-clockwise.

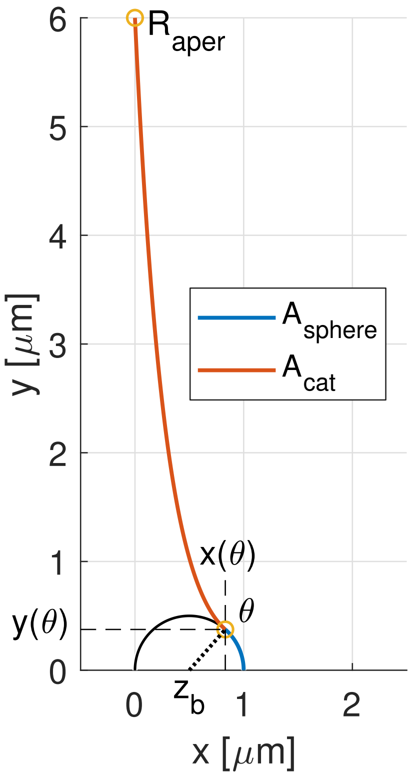

Figure 3.2: A minimal surface for bead position z_b = 0.5 µm. Part of the interface wets the bead ($A_{sphere}(\theta)$) and part of the interface is modelled as a catenary ($A_{cat}(\theta)$). The model fits catenaries between [0; R_{aper}] and [$x(\theta)$; $y(\theta)$] for θ = [0, $\frac{\pi}{2}$] and then determines the corresponding surfaces (A_{total}) to finally obtain the minimal surface (A_{min}).

The first part of the model computes the geometric minimal surface per bead position z_b. The minimal surface is dependent on the wetted angle θ:

$$A_{total}(\theta) = A_{sphere}(\theta) + A_{catenoid}(\theta) \tag{3.2}$$

The part of the interface that wets the bead is easily determined using simple geometry:

$$A_{sphere} = 2\pi r_b^2(1 - cos\theta) \tag{3.3}$$

A catenary is fit between a point far away [0, $R_{aperture}$] and [$x(\theta)$, $y(\theta)$], which provides us the parameters a and b describing the catenary geometry.

$$y_{catenary} = b\ cosh\left(\frac{x_{catenary} - a}{b}\right) \tag{3.4}$$

A_{cat} is obtained by integrating the catenary equation, with our obtained values for a and b, around the horizontal axis.

$$A_{catenoid} = \left|\frac{\pi b^2}{2}\left(sinh\frac{2(x(\theta) - a)}{b} + sinh\frac{2a}{b} + \frac{2x(\theta)}{b}\right)\right| \tag{3.5}$$

where

$$x(\theta) = z_b + r_b \cos\theta \tag{3.6}$$

For a given bead position z_b, the minimal A_{total} is found with corresponding parameters. Not every $x(\theta)$ has a solution to the catenary equation as is shown in Figure 3.3. Even so, some solutions to the catenary equations are unphysical: the catenary passes through the bead. For some $x(\theta)$, two solutions exist: see Figure 3.4. The unstable solution, denoted by purple, passes through the bead.

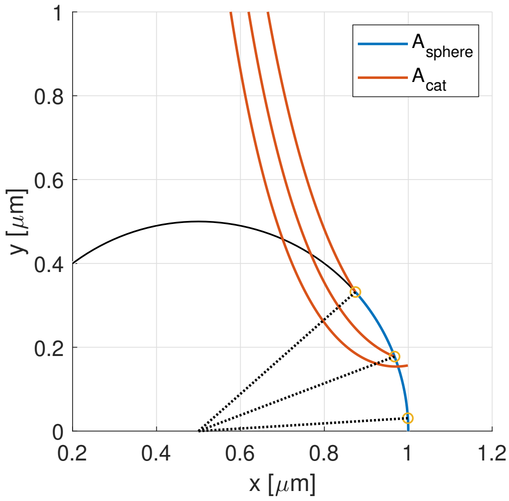

Figure 3.3: Different $x(\theta)$: for some values no solution can be found, for other values solutions pass through the bead and are unphysical.

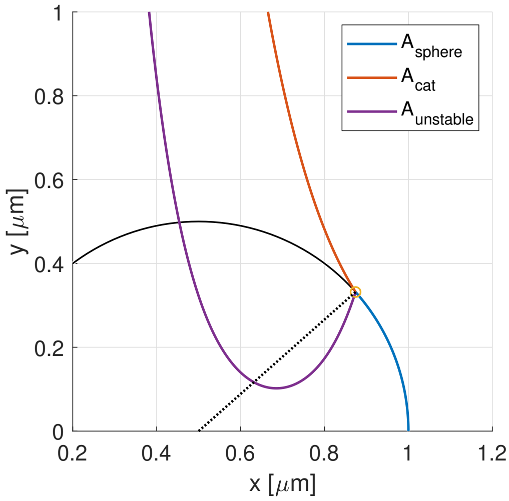

Figure 3.4: For some $x(\theta)$ two solutions to the catenary equation exist: an unstable solution, shown in purple, and a stable solution, shown in red.

The model eliminates solutions that are unphysical, such as in Figure 3.3, and adapts the initial condition for the solver when two solutions exist and the unstable solution is found, as in Figure 3.4. The initial condition is a set of a_0 and b_0 (see Equation 3.4), where a denotes a translation in the x-direction, and b is proportional to the width of the catenary curve. An overview of the geometric part of the model can be found in Figure 3.5.

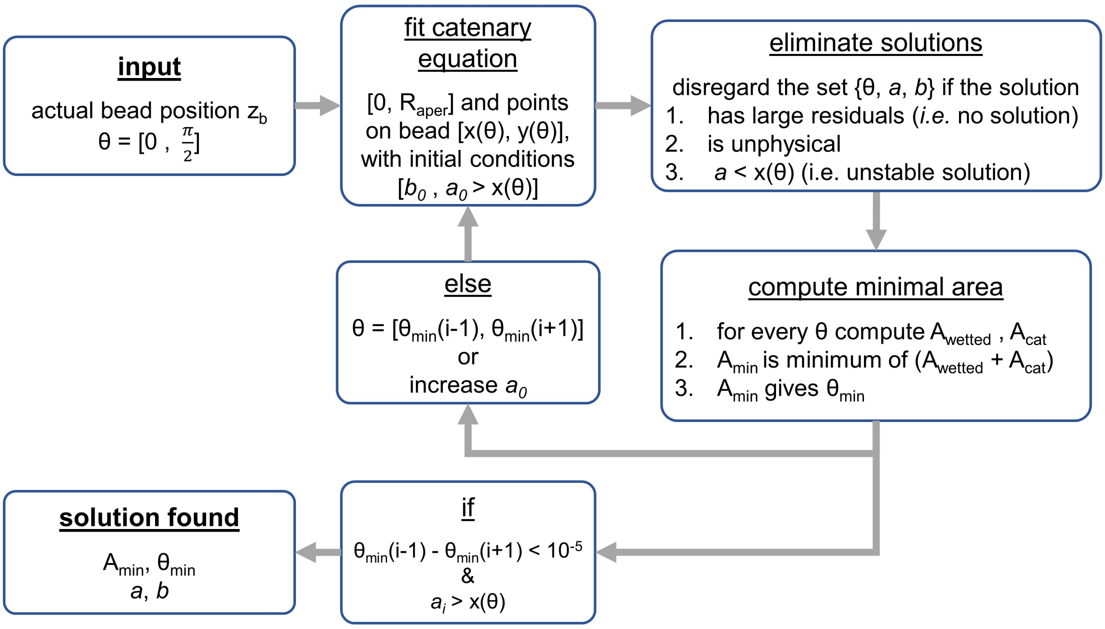
input
actual bead position z_b
θ = [0 , π/2]
fit catenary equation
[0, R_aper] and points on bead [x(θ), y(θ)], with initial conditions [b_0 , a_0 > x(θ)]
eliminate solutions
disregard the set {θ, a, b} if the solution
1. has large residuals (i.e. no solution)
2. is unphysical
3. a < x(θ) (i.e. unstable solution)
compute minimal area
1. for every θ compute A_wetted , A_cat
2. A_min is minimum of (A_wetted + A_cat)
3. A_min gives θ_min
else
θ = [θ_min(i-1), θ_min(i+1)]
or
increase a_0
if
θ_min(i-1) - θ_min(i+1) < 10^-5
&
a_i > x(θ)
solution found
A_min, θ_min
a, b

Figure 3.5: A compact overview of the geometrical part of the model.

3.2.1. Results

Figure 3.6 shows the interface wrapping around the bead for two different bead positions, z_B. In the model, the bead is moved solely the x-direction. The results shown are for the experimental values where r_b = 0.5 μm and R_{aper} = 42 μm. Figure 3.6.a shows the instance where θ = 2π/5 and Figure 3.6.b where θ = π/2. The dotted line denotes the angle θ with the x-axis. Figure 3.7 shows the main result of the geometrical model: θ versus the bead position z_b, normalised with the bead radius r_b. The zero is defined as the point where the bead starts to touch the interface. It can be seen that the interface breaks up from the bead, not at θ = π/2 but at approximately 1.15π/2. The bead position is at z_b/r_b = 6.4 just before break-up. Figure 3.8 shows the increase of interfacial area due to the bead pushing against the interface. The red curve denotes the area of the catenoid minus the area of a flat interface: it can be seen that just upon touching, the area of the catenoid becomes smaller than πR_{aper^2}. The dashed line denotes the surface area of the bead: it can be seen that way before pinch-off the minimal surface area would be complete wrapping of the bead and a flat area, but this is confined by geometry. For z_b/r_b < 2.34 the A_{sphere} contributes more to A_{tot} than the catenary.

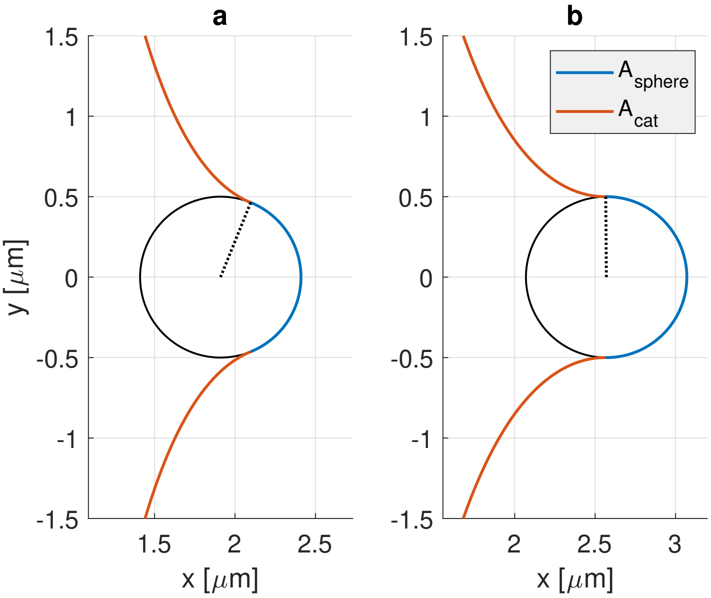

Figure 3.6: The outcome of the model visualised for two bead positions. (a.) The area that wraps around the bead (blue), forms the catenoid (red) and the angle (dotted line) for z_b = 1.9 μm, or z_b/r_b = 3.8. (b.) At z_b/r_b = 5.2, θ_{min} = $\pi/2$, the interfacial tension force is maximum.

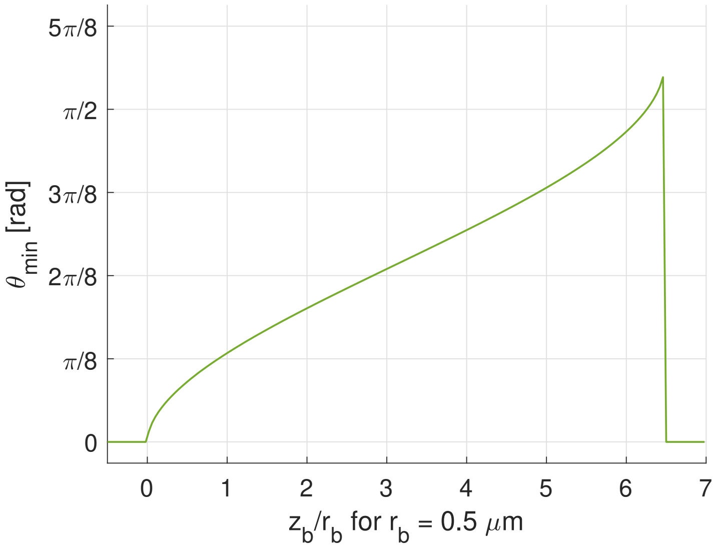

Figure 3.7: θ_{min} development versus bead position z_b for r_b = 0.5 μm. At z_b/r_b = 0, the bead touches the interface and at z_b/r_b = 6.4 the interface breaks up from the bead.

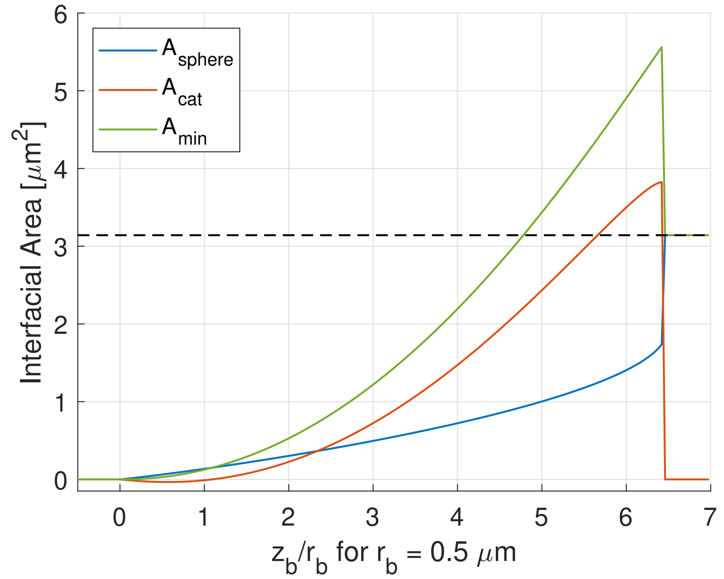

Figure 3.8: Increase in interfacial area as the bead pushes the interface. The blue line denotes the interface that wraps around the bead A_{sphere} and the red line the interface that forms the catenoid shape A_{cat} minus the area of the flat interface πR_{aper}^2. The green line is the sum of both A_{tot}. The dashed line denotes the limit where the minimal interface is a flat surface and a fully wrapped bead.

3.3. Computing the force exerted on the bead

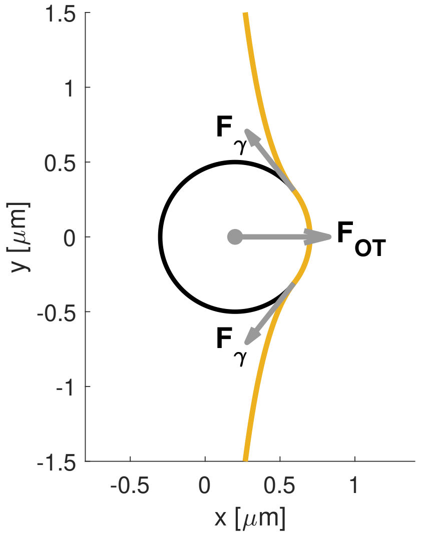

Figure 3.9: A graphical presentation of the force balance on the optically trapped bead: interfacial tension forces (F_γ) are balanced by the trapping force (F_{OT}).

From the free energy as a function of the bead position we can derive the generalised force required to deform the interface. The force is given by Equation 3.7, or the differential of the work done by the bead:

$$F_{OT} = \frac{\gamma \delta A_{min}}{\delta z_b} \tag{3.7}$$

The geometrical part of the model provides us with the interfacial area (A_{min}) as a function of the bead position (z_b). From this, a trapping force is deduced, using the measured estimate of the trapping stiffness (κ_x). In pseudocode, where j denotes the value corresponding to a certain z_b, Equation 3.7 yields:

$$F_{OT}(j-1) = \gamma \frac{A_{min}(j) - A_{total}(j-1)}{z_b(j) - z_b(j-1)} \tag{3.8}$$

The experimental output is given in the relative bead position to the focal point (denoted with d_x). For small displacements from the focal point (~150 nm) the trapping force can be thought of as a Hookean spring, and so the relative bead position to the focal point can be modelled of as a fictive spring elongation:

$$F_{OT} = \kappa_x d_x \tag{3.9}$$

Equivalently, looking at the force balance on the bead as shown in Figure 3.9, the maximum relative bead position (d_x) can be determined using the measured trapping stiffness (κ_x):

$$d_x = \frac{2\pi r_b \gamma sin\theta(z_B)}{\kappa_{OT}}$$

Using d_x, a fictive position of the focal point can be traced, so the model can be plotted conveniently with the experimental data.

3.3.1. Results

In Figure 3.10 we present the outcome of the force conversion from the determination of the shape. The figure has on the vertical axis the spring elongation, or the bead position relative to the focal point d_x, which is proportional to the trapping force by the spring stiffness κ_x. The figure shows the outcome for κ_x = 0.2 pN nm^{-1}. Here, a negative d_x means a deviation of the bead away from the focal point, so an elongation of the fictive spring. The horizontal axis shows the bead position z_b normalised by the bead radius r_b. The various colors denote different values of the interfacial tension, γ: it can be seen that the higher the value of the interfacial tension, the higher the slope of the d_x, z_b/r_b curve. However, this in itself is not a linear relationship. The slopes of the lines of the highest two decades (10^{-3} - 10^{-4} N m^{-1}) are much more similar than the slopes of the lower modelled decades.

Figure 3.11 shows the laser force exerted on the bead: $F_{OT} = -\kappa_x d_x$ versus the displacement for a trapping stiffness of κ_{OT} = 0.2 pN nm^{-1}. Both graphs use the experimental conditions r_b = 0.5 µm and R_{aper} = 42 µm.

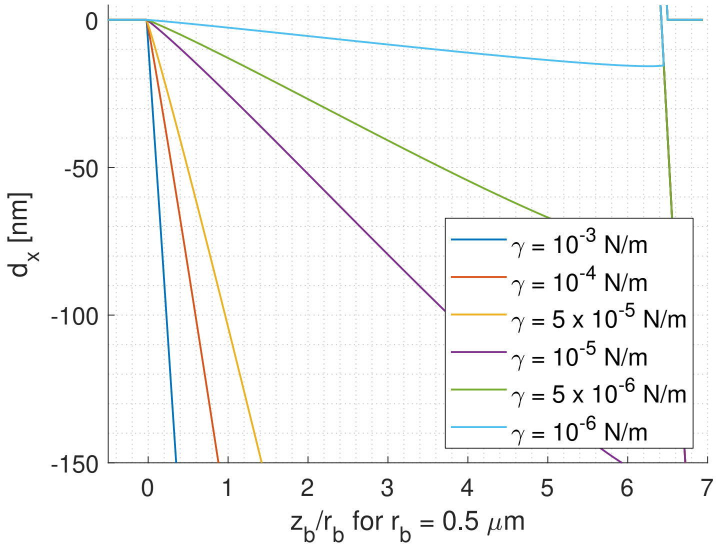

Figure 3.10: The bead position relative to the focal point (for r_b = 0.5 µm) is directly used to compute the trapping force: $F_{OT} = \kappa_x d_x$. A negative bead position denotes the bead is pushed away from the interface.

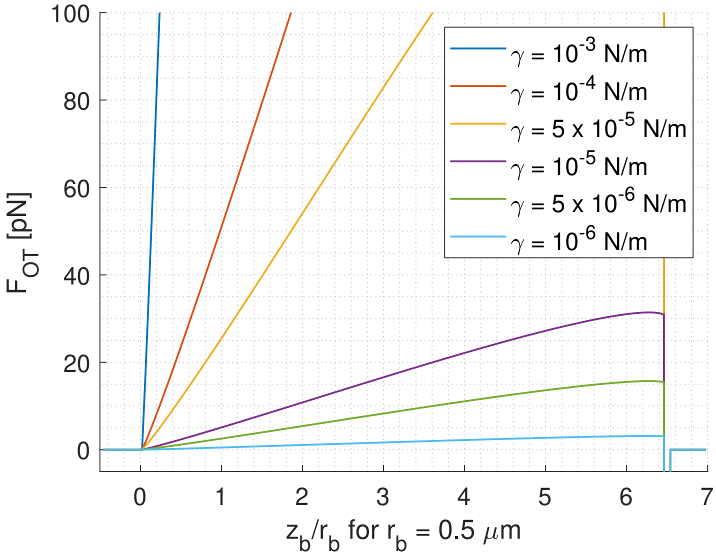

Figure 3.11: The force exerted by the optical tweezers on the bead F_{OT} versus the bead position z_b/r_b, for a trapping stiffness κ_x = 0.2 pN nm^{-1}.

3.4. Parametric study

In the previous sections, we have presented the results for the experimental conditions of r_b and R_{aper}. Namely, in the actual experiment, the aperture is rectangular, 85 µm × 100 µm. The modelled value should be along the shortest length, so we chose to model the aperture as R_{aper} = 42 µm. However, it is arguable whether this is the case: other factors such as the capillary length could reduce the actual length of the free interface. Also, we are interested to see how the model behaves for different values of r_b, which is the motivation for a small parametric study.

Figure 3.12 shows the value of θ_{min} for different values of R_{aper}. Here, the result is plotted only until θ_{min} = π/2, since the model does not converge for small ratios of R_{aper}/r_b past θ_{min} = π/2. This does not change the outcome for the force conversion, since the force is maximum at θ_{min} = π/2. We observe that for larger values of the ratio the curve becomes more similar, indicating a conversion. The conversion occurs when the slope at the far away point where the catenoid is fitted, *i.e.* [0, R_{aper}], approaches infinity.

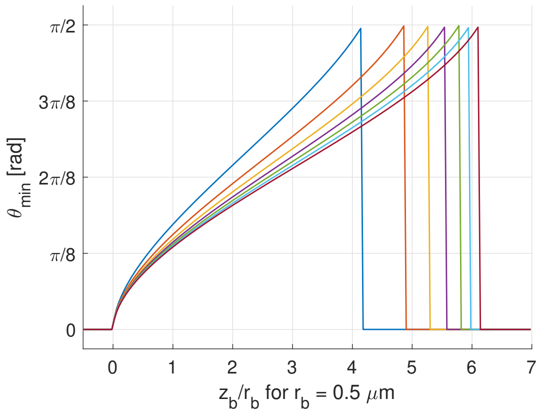

Figure 3.12: θ_{min} versus bead position for different aperture to bead ratios. In the previous sections, R_{aper}/r_b = 42/0.5 = 84.

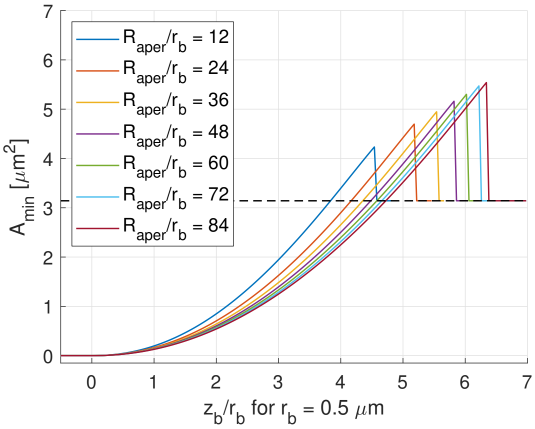

Figure 3.13: The increase in interfacial area for different ratios of R_{aper}/r_b.

Figure 3.14 shows the development of θ_{min} for three different bead radii r_b = 0.5 µm, r_b = 1 µm and r_b = 2.5 µm, with the experimental condition of R_{aper} = 42 µm. Again, for r_b = 2.5 µm so for a small ratio, the model does not converge for θ_{min} > π/2. Figure 3.15 shows the area increase per bead position for the two smaller bead radii. The work needed for obtaining θ_{min} at pinch-off, or the difference between A_{max} and the dashed line, does not scale linearly with the bead radius, but it scales with R_{aper}/r_b.

Figure 3.14, showing the experimental condition of R_{aper} = 42 µm, the aperture to bead ratios are varying significantly. In the conversion to force, it is assumed that the infinity condition is met, so at $[0, R_{aper}]$ the slope is ≈ 0. The results for the three bead radii are shown in Table 3.1.

Bead Radius	1/slope at $[0, R_{aper}]$
0.5 µm	-0.0020
1 µm	-0.0150
2.5 µm	-0.0260

Table 3.1: The residual slope at the extreme point where the catenoid is fit, $[0, R_{aper}]$, is approximated by zero. Values are for θ = $\pi/2$.

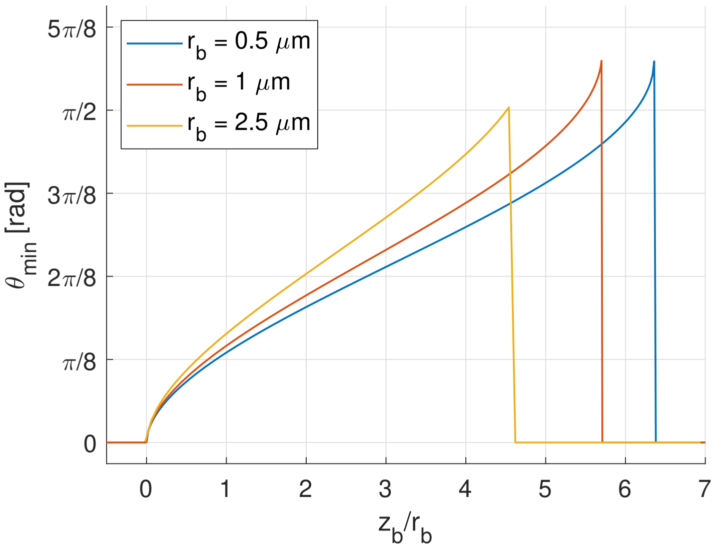

Figure 3.14: θ_{min} develops different for three different bead radii with respectively R_{aper}/r_b = [84, 42, 16.8].

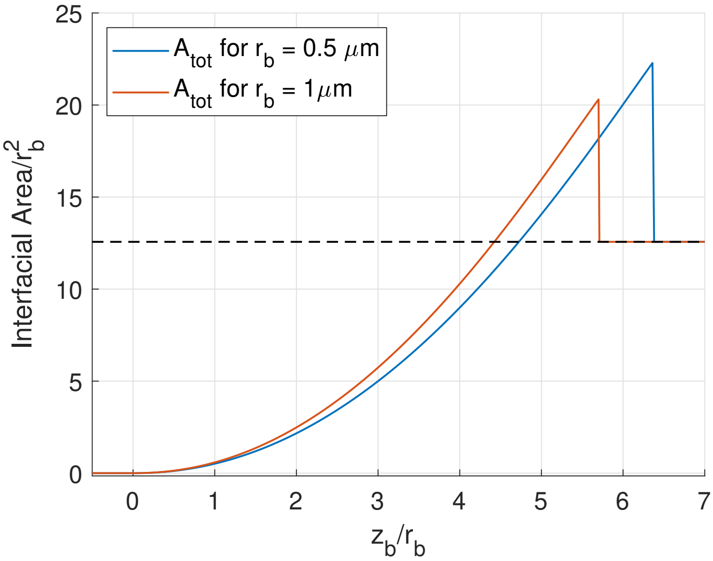

Figure 3.15: Increase in interfacial area normalized by the squared bead radius, for two different bead radii. The dashed line denotes the area equal to complete wetting of the bead.

4

Results

4.1. Dodecane-water/glycerol interface containing Span-80

Three measurements for the interfacial tension were obtained for a dodecane-water/glycerol interface, containing Span-80 at the CMC. We present the outcomes of these measurements in Figure 4.1. The red curves denote two measurements obtained in the same experiment and same interface. The bottom red curve (Exp2.1), is obtained with a lower trapping power, resulting in a lower stiffness (Table 4.1). The red model curve from Exp2.2 overlaps mostly with the blue curve from Exp1, since a similar estimate for the trapping stiffness was obtained. As can be seen in Table 4.1, the obtained values for γ range over a decade. Unexpectedly, the slope upon pushing the interface is similar in Exp2 for the medium and high trapping stiffness. One would expect a lower slope for a higher stiffness. The full results can be found in Appendix E.

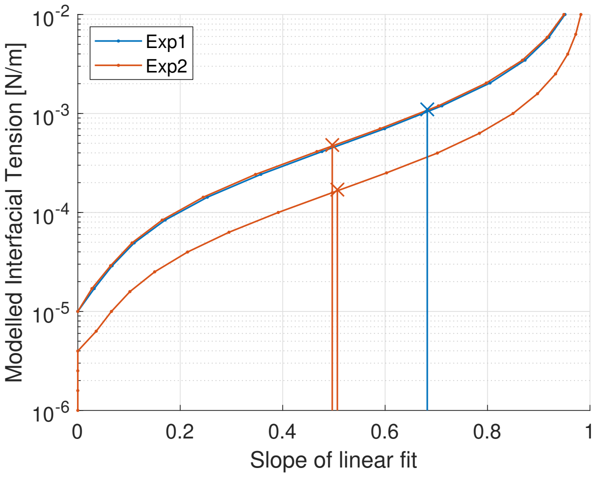

Figure 4.1: Interfacial tension measurements for an interface with expected $\gamma \approx 5 \times 10^{-3}\,\mathrm{N\,m^{-1}}$ [11]. The red curves denote the same experiment, but two different measurements, obtained at the same interface. The blue curve is a separate experiment in a different microfluidic device but exactly the same fluids.

Table 4.1: The obtained values from Figure 4.1.

	est. κ_x [pN nm^{-1}]	Measured γ [N m^{-1}]	$n_{D,aq.}$ - $n_{D,or.}$
Exp1	0.471	1.1 x 10^{-3}	2 x 10^{-4}
Exp2.1	0.166	1.7 x 10^{-4}	2 x 10^{-4}
Exp2.2	0.493	4.8 x 10^{-4}	2 x 10^{-4}

4.2. Dodecane-water/glycerol interface containing Span-80 and SDS

Two measurements were obtained for an interface containing two surfactants, with an interfacial tension estimated to be in the ultra-low regime. The two yellow vertical lines in Figure 4.2 denote the slopes obtained in the same microfluidic device, but at two interfaces. Although the applied trapping stiffness was the same, the estimated value for κ_x was significantly different, as can be seen in Table 4.2. A similar value for the interfacial tension was obtained, which is about 1.5 decade higher than expected. Note that, the expected value for the interfacial tension is based on an aqueous phase containing 25 wt% glycerol, whereas this thesis has uses 67 wt% glycerol to match the index of refraction on both sides. The full results can be found in Appendix E.

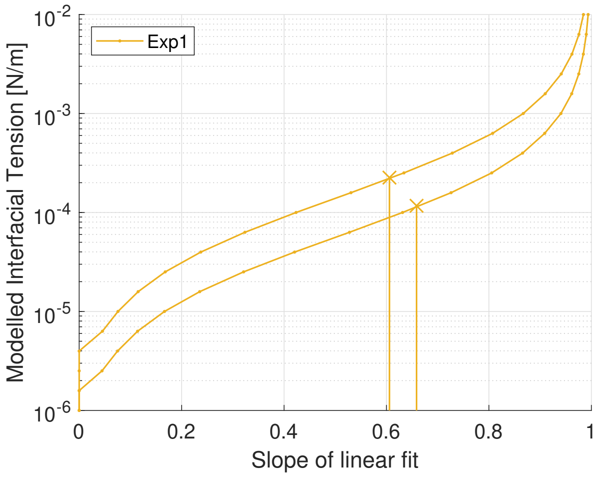

Figure 4.2: Interfacial tension measurements for an interface with expected $\gamma \approx 7 \times 10^{-6}$ N m^{-1} [12] . Both measurements were done at a similar trapping stiffness, but at a different interface.

Table 4.2: The obtained values from Figure 4.2.

	est. κ_x [pN nm^{-1}]	Measured γ [N m^{-1}]	$n_{D,aq.}$ - $n_{D,or.}$
Exp3.1	0.144	2.3 x 10^{-4}	2 x 10^{-3}
Exp3.2	0.058	1.2 x 10^{-4}	2 x 10^{-3}

4.3. Scatterplots near the interface

As a side-result to measuring interfacial tension, we have been able to measure the Brownian motion near the oil-water interface. To the best of our knowledge, this is the first time the variance in the direction perpendicular and parallel to the interface have been measured. Figure 4.3 shows the scattered bead position for three different bead positions at an oil-water/glycerol interface, without surfactant. γ for a dodecane-water interface is $53 \times 10^{-3}\,\mathrm{N\,m^{-1}}$ [10]. In the left image, the bead is positioned $-2\,\mu\mathrm{m}$ from the interface, so the bead is not yet touching. The position data is evenly scattered around the mean: the contour lines form a circle. The bead position is measured over three seconds per position, at a sampling frequency of 50 kHz. Each red dot denotes a single measurement and density contour lines are drawn to visualise the distribution. Upon touching the interface, at 0 µm, the bead position variance in the y-direction is increased, whereas it has decreased in x-direction. Moreover, the position variance in the x-direction appears to be asymmetric. At 0.017 µm, the position variance has increased. Upon interacting with the interface, the bead is exposed to the interface stiffness, so the position variance is expected to decrease. Observing an increase in position variance leads us to eliminate this data set from analysis to determine the interfacial tension.

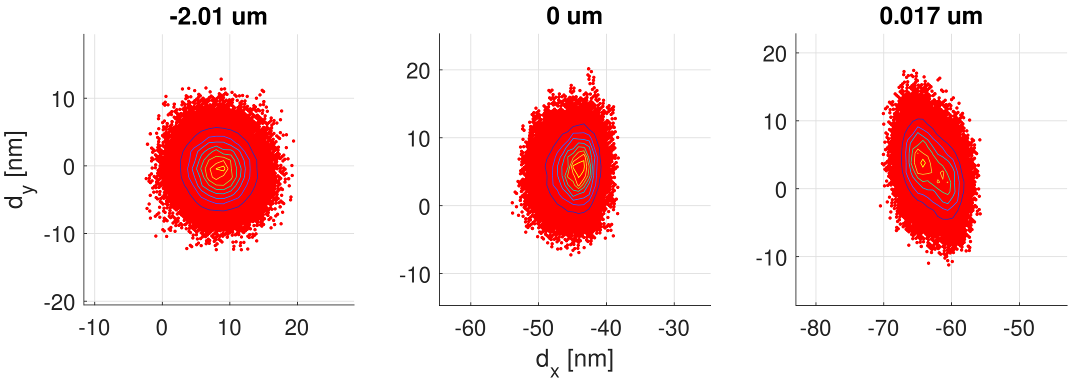

Figure 4.3: Scattered bead position for three positions (-2, 0 and 0.017 µm) from a dodecane-water/glycerol interface, without surfactant. The trapping stiffness is estimated to be κ_x = 0.494 pN nm^{-1}. Each position was sampled for three seconds at 50 kHz.

Figure 4.4 shows the scattered bead position near a dodecane-water/glycerol interface, containing the two surfactants Span-80 and SDS. The applied trapping force is lower than in Figure 4.3, thus increasing the position variance, *i.e.* the spread of the red spot. For this interface, we have measured a γ of $2.3 \times 10^{-4}\,\mathrm{N\,m^{-1}}$. In literature, for the same surfactant concentrations but an aqueous phase containing 75 wt% water, γ is reported to be 7 □N/m [12].

At $-2.37\,\mu\mathrm{m}$ from the interface, we observe an even spread of the observed positions, obtaining quite circular contour lines. As the bead touches the interface, the spread appers to become more oval: σ_y^2 increases slightly, but σ_x^2 decreases. These scatter plots correspond to Exp3.1 from Table 4.2.

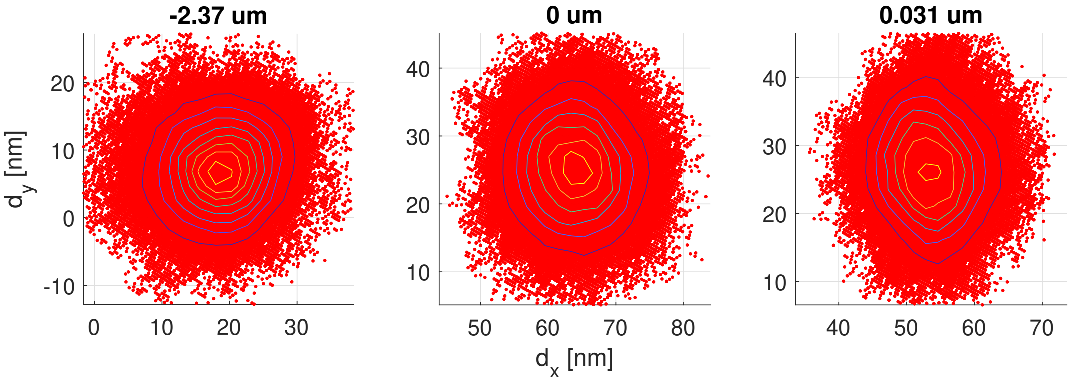

Figure 4.4: Scattered bead position for three positions (-2.37, 0 and 0.031 µm) from a dodecane-water/glycerol interface, without surfactant. The trapping stiffness is estimated to be κ = 0.144 pN nm^{-1}. Each position was sampled for three seconds at 50 kHz.

5

Further Observations/Limitations

5.1. The optical drift is proportional to the laser power

We have observed that the optical drift, *i.e.* the deviation from the calibrated alignment of the detection and trapping laser where d_x = 0 nm, varies dependent on the applied laser power. Figure 5.1 compares three experiments, that were done over the same path, but with different laser power. It is observed that the drift increases with decreasing trapping power. The variance remains relatively constant, indicating that the focal point hold its shape. The fluctuations observed in the variance are hypothesised to be due to contamination of the device or micelle agglomeration on the interface (see Section 5.5). The drift for the low and medium laser power increases rapidly when near the interface, lowering the success rate of experiments. The eccentricity and orientation of the focal point are found to stay constant, indicating that the optical aberrations are minimal. It should be noted that the drift is not observed to be dependent on Δn_D, if one compares, for example, Section 2.5.3 to Figure 5.1. We note that a large, asymmetric drift also occurs when the bead is moved parallel to the interface (see Appendix E.8). Also, we moved beads through an empty aperture and did not observe a drift. We conclude that the drift is not originating from the device itself (Appendix E.7).

5.2. The optical drift differs per interface

The data for medium trapping power in Section 5.1 is repeated at exactly the same conditions, but at a different interface, having a different curvature. Figure 5.2 shows that for the second interface the drift is less, but the variance is about twice as high. The variance could be increased due to noise or contamination: in the PwSD no source of noise is found. As is discussed in the Chapter 4, these experiments yield the same slope for the x versus displacement curve, despite having significantly different variances and thus estimated κ_x.

5.3. The position variance increases upon touching the interface

In most of the experiments, the position variance is observed to increase upon touching the interface. This is opposite of what it theoretically predicted: the bead is expected to be less mobile when touching a significantly stiff interface. Figure 5.3 shows the scatter plots of a bead touching the interface with a high trapping power. It can be directly seen that the position variance increases upon touching, indicated by the spread of the red blob, which becomes larger after 0 µm. The gradual appearance of a second spot, at an angle of approximately 45°, is observed in other experiments too.

Recalling Section 2.2.1, the trapping stiffness in the z-direction is found to be lower than then trapping in the x- and y-direction. It is hypothesised that in the cases where the variance increases upon touching the bead slips in the z-direction prior to indenting, possibly causing the frequently observed optical aberration. However, one of the two successful experiments in the two-surfactant interface, where the variance was found to decrease, was conducted along the same trajectory.

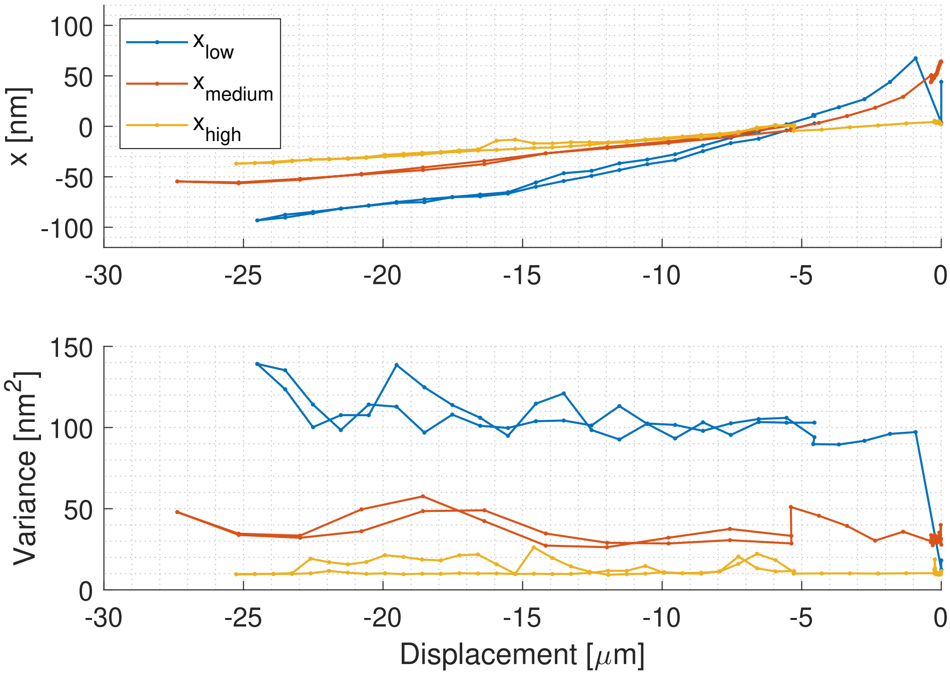

Figure 5.1: The relative bead position versus displacement for three different laser powers: low power (estimated κ_x = 0.033 pN nm^{-1}), medium power (estimated κ_x = 0.124 pN nm^{-1}) and high power (estimated κ_x = 0.372 pN nm^{-1}). The three experiments are conducted on the same trajectory and thus interface. It is observed that the optical drift, *i.e.* the variation from d_x = 0 or the point of calibration, varies per laser power. Secondly, for the low and medium power the drift increases non linearly closer to the interface.

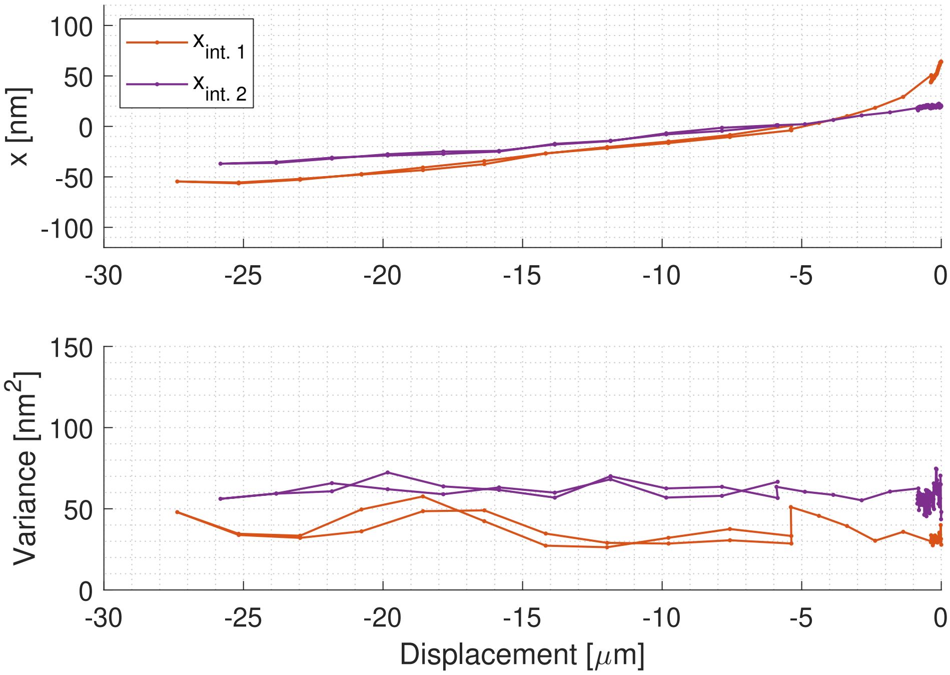

Figure 5.2: The relative bead position versus displacement for two interfaces (*int. 1* and *int. 2*), but the same laser power. The optical drift and variance differs for both measurements. The estimated stiffnesses are respectively κ_x = 0.144 pN nm^{-1} and κ_x = 0.058 pN nm^{-1}.

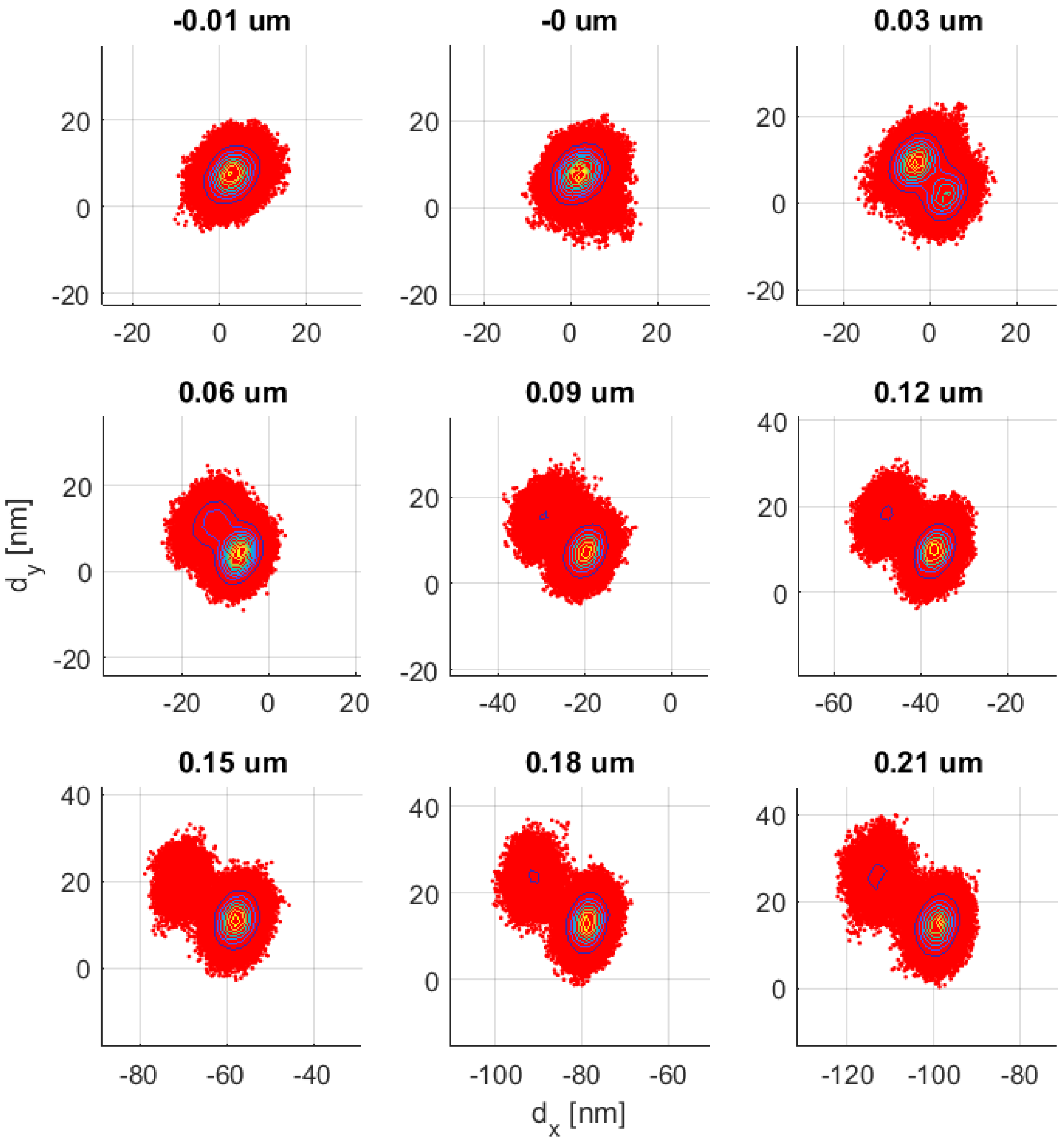

Figure 5.3: Scattered position data for a two-surfactant interface, using a high trapping power with estimated κ_x = 0.370 pN nm^{-1}. Each dataset was recorded for three seconds at 50 kHz. It can be seen that upon touching the interface at 0 µm the position variance, *i.e.* the spread of the red cloud, increases. This indicates a higher mobility of the bead, which is opposite of what is expected.

5.4. The calibration curve changes per laser power

The bead position is determined by converting the PSD voltage reading to spatial dimensions via the calibration procedure. The calibration procedure is carried out using a custom-built LabView VI, where the trapped bead is moved along a grid of known spatial dimensions, as the detection laser is kept stationary. This VI is built for water solutions, having a lower viscosity and a higher difference in index of refraction between the fluid and bead, thus having a higher resolution and stiffness. The VI could not be modified within the scope of a MSc thesis.

It is observed that the calibration curve is different per applied laser power. The calibration curve is obtained using three powers: low trapping power (C_{low}), medium trapping power (C_{medium}) and high trapping power (C_{high}). Table 5.1 shows the average position μ and variances (σ_x^2,σ_y^2) for a voltage reading close to the point of calibration. It can be seen that the differences in the calibration are small and random. However, when the bead has moved in the trap or the detection laser and trapping laser have moved, such as in Table 5.2, the difference becomes big. It seems that for these calibration curves the variance is overestimated. It is noted that the grid dimension in the VI is set to 572 nmx572 nm.

Table 5.1: The output of the voltage to nanometer conversion for a dataset close to the calibration point. The different calibration curves are obtained with three laser powers: C_{low}, C_{medium} and C_{high}.

	μ [nm]	σ_x^2 [nm^2]	σ_y^2 [nm^2]
C_{low}	[1.11 , 19.72]	36.97	44.67
C_{medium}	[-7.97, 11.70]	37.65	48.57
C_{high}	[-8.87, 11.36]	36.91	47.52

Table 5.2: The output of the voltage to nanometer conversion for a dataset with a large deviation from the calibration point, which occurs in the optical drift. The different calibration curves are obtained with three laser powers: C_{low}, C_{medium} and C_{high}.

	μ [nm]	σ_x^2 [nm^2]	σ_y^2 [nm^2]
C_{low}	[17.60 , 105.74]	55.86	37.14
C_{medium}	[6.55, 97.68]	46.41	30.40
C_{high}	[4.34, 93.68]	41.69	26.39

5.5. Surfactant-loaden interfaces are dirty

The fluctuations in the variance in Figure 5.1 are hypothesised to be due to local contamination. Micelle clusters are observed on the interface and appear to be induced by high laser powers. Figure 5.4 shows an interface with a micelle cluster, where the length is about 200 nm. Over the duration of three seconds, the cluster appears to have moved about 50 nm. These pictures were taken under a microscope without laser.

Secondly, it is observed that micelle growth is induced at high laser powers, as in Figure 5.5. This picture shows a bead, trapped with a very high laser power of 40 % emission near an interface containing SDS and Span-80 at 5 wt%. Over the course of about five minutes, micelles have agglomerated on the organic side.

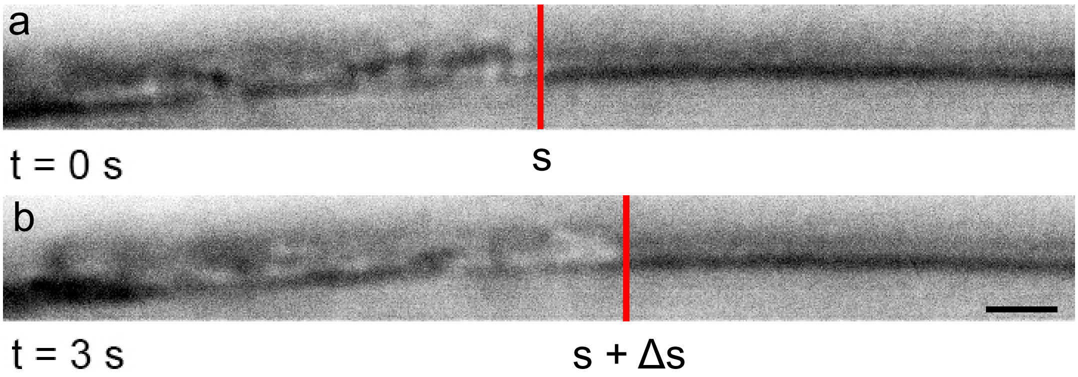

Figure 5.4: A high magnification picture of the SDS and Span-80 interface where n_D is slightly mismatched for visualisation. The red line denotes the side of the micelle cluster. Over the duration of three seconds, the cluster moves about 2 µm. The concentration of Span-80 was 0.05 wt% and 6 mM SDS. This interface was not exposed to a laser. Scalebar 2 µm.

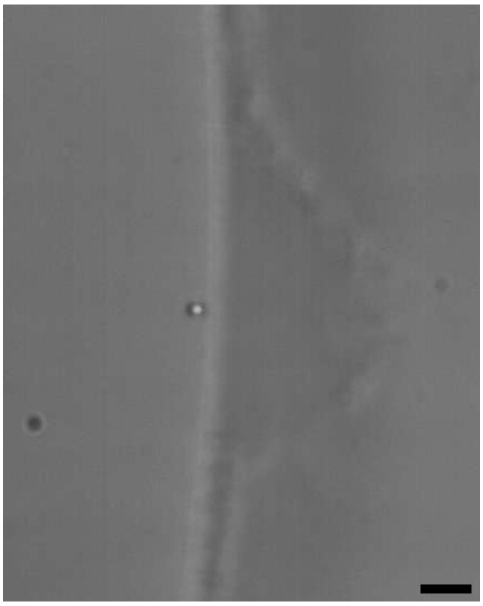

Figure 5.5: Picture of a trapped bead near an interface containing Span-80. The bead is trapped near the interface for about five minutes, causing surfactants to agglomerate on the organic side. Scale bar 5 µm.

6

Discussion and Conclusion

6.1. Discussion on the obtained results

By utisiling the optical tweezers, we have obtained measurements for two estimated interfacial tensions. For the interface containing only Span-80, one measurement is similar to the expected value, but the two others are about a decade lower. Potentially, the bead is also moving in the z-direction, but we do not have resolution along this axis. Movement in the z-direction is expected to underestimate the stiffness, as we record an apparent indentation of the interface, whereas this does not need to be the case. It is remarkable that the measured slopes of Exp2.1 and Exp2.2 are so similar even though the stiffness varies by a factor 3. The stiffness in the z-direction, counteracting the slipping, is also three times higher in Exp2.2. Recall that experiments are conducted at approximately the middle of the microfluidic device, but the pinning of the interface at the top and bottom varies per interface and is random. This means that the interface is probably not tangent to the beads path. Thus the hypothesis is that for Exp2.1 and Exp2.2 the interface was locally curved and k_z was in neither cases high enough to indent the interface in the z-direction. The decrease of the position variance upon touching can be explained by the bead being pushed towards the beam waist. The gradient force is stronger at axial positions closer to the waist, resulting in a larger apparent stiffness or a lower position variance. We think the initial assumption that slipping along the z-direction would always come with an increase in position variance was not entirely correct as it does not cover the bead being pushed towards the bead center.

On the other hand, the measurements for the two-surfactant interface seem to overestimate the interfacial tension by approximately 1.5 decade. Although not impossible, slipping on the interface is not the probable cause: a similar slope is measured on two different interfaces. Recall that we compare our obtained value for the interfacial tension with Tsai et al. [12], where we use exactly the same concentration of surfactants, but a much higher concentration of glycerol (25 wt% versus 67 wt%). We find that the reported values of γ upon increasing 25 wt% glycerol are much lower (see Appendix A) than for the same system, with pure water as the aqueous phase. However, as surfactant dynamics are complex, we doubt our assumption that the interfacial tension from a 67 wt% glycerol aqueous solution would be similar to a 25 wt% glycerol aqueous solution. Secondly, in their experimental design the interface is formed dynamically in a co-flow approach, so surfactant and glycerol adsorption and absorption time is limited. As discussed in the Introduction, the addition of two surfactants lowers the interfacial tension from $\mathcal{O}(10^{-3})$ N m^{-1} to $\mathcal{O}(10^{-6})$ N m^{-1}. The glycerol-dodecane interface has a significantly lower interfacial tension, due to the weaker hydrogen bonds [56]. In addition, high mass fractions of aqueous glycerol change the local properties of the interface, possibly influencing the interfacial tension [57].

Next to this, the mixture is prepared using SDS in solid state. As this the final mixture only contains a very small amount of this powder, small discrepancies can result in large deviations of the final solution. For example, the SDS powder form is not preferred for measurements of interfacial tension, since it absorbs water from the atmosphere when kept over a long time, reducing the actual SDS content in the mixture. In this thesis, there was no possibility of using a pre-made SDS solution in liquid form. As this is an empirical observation by colleagues in the lab, no quantitative dataset can be presented.

We do not expect that the accuracy of our estimate of the trapping stiffness is responsible for the discrepancy. As we have seen in Chapter 2, a difference of 20 % in stiffness does typically not give a difference of a decade for the reading of the interfacial tension. It should be noted that the variance method is not the most accurate method for determining κ.

We hypothesise that the origin of the discrepancy comes from a geometrical point of view. Namely, for the estimated interfacial tension, the aperture dimensions are smaller than the capillary length. Although we estimate the curvature to be about two orders of magnitude smaller than the bead, we wonder whether our assumption that the pressure difference across the interface is negligible. If this assumption fails, our model is inaccurate and this can explain the large discrepancy.

To conclude, we hypothesise that the values obtained in Exp2 for the one surfactant system are erroneous, since the slope is too similar for the two estimates of the stiffness. An explanation could be that the bead has moved in the z-direction, towards the beam center, which would decrease the position variance. The result for Exp1 matches the expectations. In the case of the two-surfactant system, a validation measurement with for example the spinning drop method is needed, to quantify the actual value of γ. Then, if the measured value is still significantly different from the expectation, the secondary hypothesis is that the model has failed.

6.2. Limitations

As per the observations in Chapter 5 and the numerous experimental attempts needed to attain the five measurements, we discuss some limitations to optical tweezers tensiometry.

- **The shape of the interface is random and experimentally hard to determine.** The interface is formed along the apertures in the microfluidic device, which all have the same dimensions. However, it is observed that the three-phase contact line, *i.e.* the point where the organic phase, aqueous phase and the microfluidic device meet, is formed at random. The pinning of the three phase contact line is not governed by the liquid-liquid interfacial tension and the liquid-solid interfacial tensions, but mostly dependent on hysteresis, depending on the history of the contact line motion [25]. The origin of the hysteresis is the physical roughness and chemical heterogeneity of most solid surfaces [58]. The contact line is formed upon filling the device and dependent on macroscopic and microscopic impurities and imperfections. We end up with different, but observable, curvatures in the x-y-plane, and unknown, but presumably random, curvatures in the z-direction. This is a limitation for determining the force vector exerted on the bead, as well as minimising bead slipping on the interface and the validity of the model.

- **Minimising Δn_D means altering the fluid properties drastically.** We had to add a mass fraction of 0.67-0.69 glycerol to water to satisfy the refractive index difference. This drastically increased the viscosity and difference in refractive index between the bead and surrounding fluid. The increased viscosity mainly influenced our sampling time, meaning we increased τ_s from 1 to 3 seconds, which seemed to be sufficient. However, the in-built calibration procedure is not modifiable within the scope of a MSc thesis: we speculate this has minimal effect on the presented outcomes. More importantly, the decrease in Δn_D between the bead and surrounding fluid lowered the trapping stiffness at the usual emission powers [59]. In the Section 2.5 we have discussed our observation of reduced trapping stiffness of 2/3. Moreover, it is hypothesised that in our system the resolution on the PSD is lower, since we found a higher standard deviation for our values. This is again explained by a lower difference in index of refraction: less light is scattered through the bead on to the sensor of the PSD. Lastly, we observe that even though the fluids index of refraction is matched, they have a distinctly different absorbance spectrum (Appendix F).

- **The operating measurement range for γ is limited by the model accuracy.** Recall Section 3.1 about the working principle of the model. The Young-Laplace equation is derived, and we assume the interface to be flat, thus have zero pressure difference. We can fit a minimal surface with zero curvature: a catenoid. This model was an initial guess towards estimating the interfacial tension. As the experiments proceeded, it seemed experimentally very difficult to control the interface curvature and contact angle. For example, the device was treated with the hydrophilic S100d or trichlorosilane, increasing the surface roughness, but no significant reduction in the curvature was observed. In none of the experiments a flat interface was obtained. Recalling Equation **??**, the work needed to expand the interface is:

$$dW = -p_o dV_o - p_w dV_w + \gamma_{ow} dA \tag{3.1}$$

where our model assumes a zero curvature interface thus $-p_o dV_o - p_w dV_w = 0$. However, if we look at curvatures obtained in the x-y-plane, we see this is not the case. Taking the average of some of the typical obtained curvatures of the interface, we find an average of about 100 µm, which corresponds to, for $\gamma = 10^{-3}\,\mathrm{N\,m^{-1}}$, to 20 Pa, and for for $\gamma = 6\mathrm{x}10^{-6}\,\mathrm{N\,m^{-1}}$, to 0.12 Pa. It should be remarked that the curvature in the z-direction could not be determined experimentally and is thus possibly smaller than the named value. More importantly, the capillary length is respectively 475 µm and 37 µm. This means that the tension measured not of a free interface.

- **It is desirable to operate the laser at medium trapping power.** It is observed that at very high trapping power the laser becomes asymmetric, less reproducible and unstable (see Appendix E.9). Moreover, micelles are observed to develop rapidly, despite the surfactant concentration being below the CMC. Thus it is desirable to operate the laser at emission powers 20% to 30%, referred to in this thesis as ”medium” and ”high” trapping power, corresponding to stiffnesses 0.1-0.5 $\mathrm{pN\,nm^{-1}}$ in aqueous glycerol. If one wishes to measure the maximum force, that is when the bead penetrates the interface, and omits to consider surfactant agglomeration due to heat, the interfacial tension measurement range would be $\gamma = 3.2 \times 10^{-6}\,\mathrm{pN\,nm^{-1}}$ to $1.6 \times 10^{-5}\,\mathrm{pN\,nm^{-1}}$.
- **The optical drift is observed to be dependent on Δn_D, the laser power and the orientation of the interface.** This drift becomes a problem when the average bead position is translated out of the linear calibration regime before touching the interface. Since in the current experimental set-up Δn_D is unknown and the orientation of the interface is random, it is experimentally difficult to obtain a small optical drift before touching the interface. It should be noted that the calibration, *i.e.* the point where the detection laser and trapping laser are aligned so the set zero, should be sufficiently far from the interface to avoid complex corrections using Faxèns Law.

6.3. Are the optical tweezers suitable as a tensiometer?

In Chapter 1 we discussed the existing methods to measure (ultra-low) interfacial tension. The potential of the optical tweezers lays in accurate determination of the interfacial tension, especially in the ultra-low regime. Although the obtained measurements for the interfacial tension are not conclusive, we developed an experimental procedure that is promising to be able to measure ultra-low interfacial tension. However, as the need in industry lays in researching ultra-low interfacial tension for specific emulsions, the measurement accuracy for optical tweezers tensiometry is reduced due to the strong requirement on the fluid properties. The index of refraction needs to be matched for the two sides to the interface. In the cases researched for this thesis, we added 67%wt glycerol to water. Although it is unknown by exactly how much the adding of glycerol alters the interfacial tension, it will indefinitely reduce the accuracy of the measurement.

We believe there is great potential in utilizing the optical tweezers to study interfacial phenomena: this is not limited to merely tensiometry. The optical tweezers lack flexibility and speed for good suitability as a tensiometer. Since we have seen that the optical tweezers can be modified to operate in a two-fluid, hydrocarbon-water system, they can be utilized to study, for example, droplet coalescence or pinch-off phenomena. Another option is to study interfacial phenomena in systems that consists of two phases that are very similar, such as aqueous two-phase systems. In Chapter 7 we further develop the potential of the optical tweezers as an academic tool to study interfacial phenomena.

7

Recommendations

We find that the optical tweezers are a versatile and precise tool suitable for tensiometry. A tensiometer requires rapid and accurate determination of the interfacial tension, which is difficult in optical tweezers tensiometry since the fluid properties need to be altered drastically, in order to match the index of refraction, The optical tweezers might find better applicability on studying other interfacial phenomena. For example, challenges remain in the experimental studies of near-boundary Brownian motion, whereas this is of great academic interest [60–62]. Several academic endeavours have probed the diffusion parallel to a variety of interfaces, but no research is found that was able to probe the perpendicular Brownian motion near an oil-water interface. Secondly, since the optical tweezers have been modified to work in a two-phase system, the interfacial tension can be varied. Other examples include studying the controlled merging of oil-water interfaces, or studying the interface pinch-off dynamics at lower interfacial tensions.

If one wishes to continue to utilise the optical tweezers using the proposed methodology, several improvements can be made to the existing experimental procedure.

- **Measure n at λ = 830 nm.** In this thesis we have only been able to determine the refractive index difference in the visible light, Δn_D, which is not necessarily similar for the near-infrared range, where the lasers operate. An option is to modify an Abbe refractometer such that it can operate at λ = 830 nm [63] or develop a technique to estimate refractive index using the optical tweezers [64]. If the refractive index is matched well, there will be minimal optical drift and the laser will not induce micelle formation at the interface. The need to control the curvature of the interface is then also eliminated. Preliminary experiments using an unmodified Abbe refractometer, near-infrared light source and sensor did not deliver reproducible results. The modification as proposed by Rheims et al. [63] to correct for the dispersion in the glass prism is thus needed and easy to implement.

- **Develop a microfluidic device that allows for control over the shape and pinning of the interface.** Preferably, one would want to push the bead against a free interface. This means that the smallest length scale of the interface is > 2 x l_{cap}. The capillary length relates gravitational forces and interfacial tension forces, and is thus dependent on the density difference and interfacial tension. If the interfacial tension is low, and the aperture dimensions are much larger than l_{cap}, the interface is prone to be unstable. It is thus desirable to have a variety of aperture sizes available, if one wishes to measure a range of interfacial tensions, varying over decades. The set-up used for this thesis has been used by others for microfluidic devices with a depth of 2 mm: this means that a design for the microfluidic device is not limited by the set-up.
  Secondly, in order to control the shape of the interface, it is needed to control the position of the three-phase contact line. Random pinning at high surfactant concentrations can not be controlled by exerting a higher pressure on one side of the microfluidic channel, as this can induce micelle formation. However, a local roughness in the microfluidic device could drastically increase the chance of pinning there.

- **Use different organic phase.** Using a different organic phase with a lower refractive index means that less glycerol has to be added to the aqueous phase. The sampling time can be shorter and the acquired trapping stiffness will be higher. For example, if one were to use heptane instead of dodecane, this would require about 45 wt% glycerol on the aqueous phase.

- **Use two fluids that are more similar, such as aqueous two-phase systems (ATPS).** ATPS form when two polymers are added to water, this forms two aqueous phases. The more dilute the polymers, the lower the interfacial tension between the two phases. The advantage of researching an ATPS system is that the two phases have similar properties: the contact angle will be closer to $\pi/2$ and no surfactant is needed. However, there is a risk of a three-phase contact line forming on the bead, and a proper coating should be researched. Moreover, adding polymers can induce non-Newtonian behaviour in the surrounding fluid, providing problems with calibrating the optical tweezers. Several methods have been proposed to accurately calibrate the optical tweezers in non-Newtonian fluids [65].

- **Develop a model to study laser behaviour through a curved interface.** We conclude that the uncertainties in the experimental outcome, *i.e.* the variance going up upon touching the interface or the bead drifting our of the calibration domain, are dependent on Δn_D, the curvature and the laser power. In order to research which of these is dominant, a model would be the place to start. It should be noted that a simple ray-tracing model is not appropriate, since focused laser beams are limited by diffraction [66].

- **Calibrate for the z-coordinate.** Calibrating the relative bead position in the z-direction is cumbersome and less accurate than for x and y, but possible. Not only would this increase the accuracy of the measurement, but also other factors such as distortions in the z-direction could be characterised.

A

Literature values for the estimated interfacial tension

This appendix reports the obtained literature values for relevant fluids. We conclude that adding one surfactant, either Span-80 or SDS, can lower the interfacial tension by approximately an order of magnitude. Adding both Span-80 and SDS has a synergetic effect: the interfacial tension is reduced by several orders of magnitude. Also, we conclude that adding 25 wt% glycerol to the two-surfactant system lowers the interfacial tension relative to pure water.

Table A.1: Literature values for water-dodecane systems containing Span-80 and/or SDS.

Aqueous phase	Organic phase	Surfactant(s)	γ in $\mathrm{N\,m^{-1}}$	Source
water	dodecane	[-]	5.3×10^{-2}	Zeppieri et al. [10]
water	hexadecane	0.05 wt% Span-80 (CMC)	5×10^{-3}	Cortés-Estrada et al. [11]
water	hexadecane	8 mM SDS (CMC)	7×10^{-3}	Cortés-Estrada et al. [11]
water	dodecane	10 wt% Span-80	2.7×10^{-3}	Shum et al. [67]
water	dodecane	2 wt% Span-80 4 mM SDS	3.0×10^{-5}	Shum et al. [67]
water 25 wt% glycerol	dodecane	10 wt% Span-80 4 mM SDS	7.5-9.5 $\times 10^{-6}$	Tsai et al. [12]
water 25 wt% glycerol	dodecane	10 wt% Span-80 6 mM SDS	7×10^{-6}	Tsai et al. [12]

B

Estimating the refractive index

The aqueous phase

The aqueous phase consists of a mixture of water and glycerol. At λ = 1550 nm, the relation between the mass fraction of glycerol in aqueous solution and refractive index is reported to be linear [68]. For simplicity, this result is assumed to be valid at λ = 830 nm. So, the necessary weight fraction of glycerol to match n on the organic phase is calculated using a linear approximation. For pure glycerol and pure water, the refractive index changes as a function of wavelength as per Figure B.1 for water, and Figure B.2 for glycerol. For water, the two values are reported at λ_{830}, which differ by 0.004. For glycerol, there is only one experimentally determined value for λ_{830}, which differs from the estimate by 0.005. The other literature values present are measured at different temperatures.

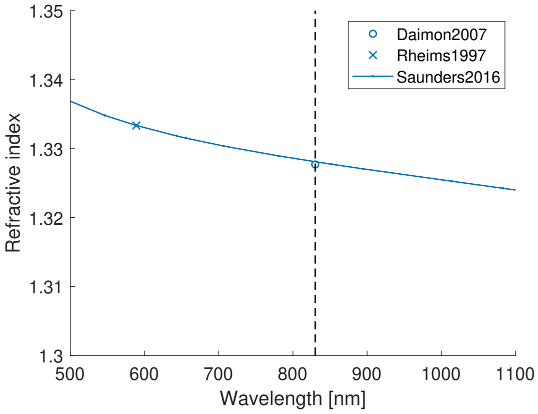

Figure B.1: Index of refraction of water versus wavelength for various literature sources [63, 68, 69] at 20°. The black, dashed line denotes the wavelength of the detection laser.

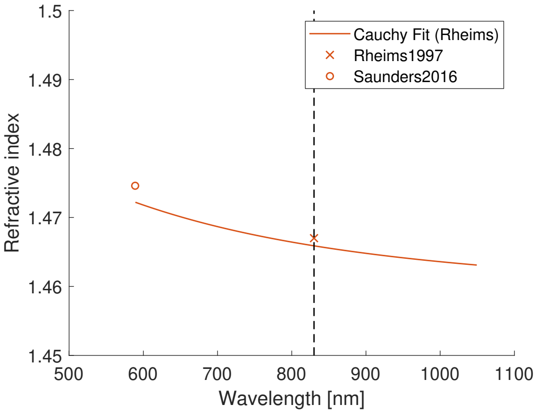

Figure B.2: Index of refraction of glycerol versus wavelength for various literature sources [63, 68] for 20°. The black, dashed line denotes the wavelength of the detection laser.

The organic phase

There is little literature present on the refractive index of dodecane in the near infrared spectrum. Figure B.3 shows the values reported in the two literature sources obtained at a temperature of 25°C. Figure B.4 shows obtained values for n as a function of temperature, at wavelengths unimportant to this thesis. A linear fit is made to the data points, and it is observed that the slope is similar. This slope is used to estimate n for λ_{830}.

First, the data points from Figure B.3 at λ_{670} and λ_{925} are linearly interpolated, to obtain a value of n = 1.4157 at λ_{830}. This value is corrected for the temperature using the slopes obtained in Figure B.4: n = 1.4136 for λ_{830} at 20°C.

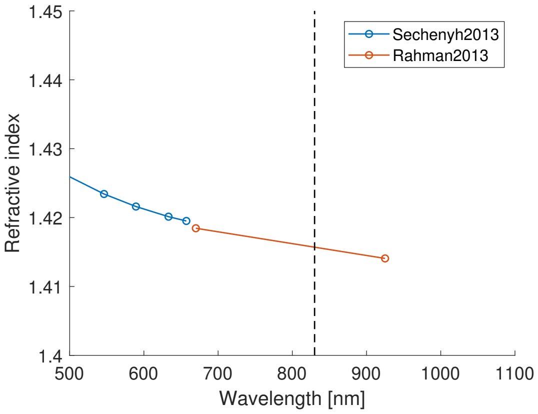

Figure B.3: Index of refraction of dodecane versus wavelength for various literature sources, for 25°C. The dashed line denotes the wavelength of the detection laser.

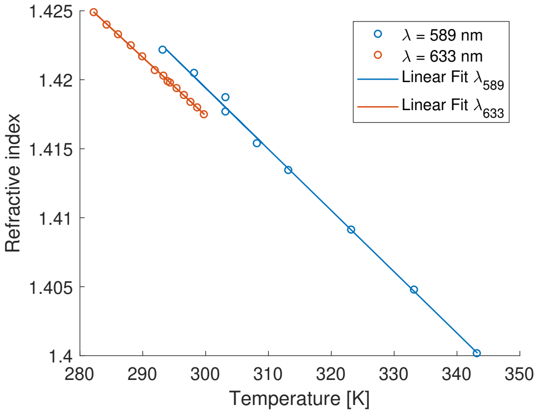

Figure B.4: Index of refraction of dodecane versus temperature for two wavelengths. The dashed line denotes the wavelength of the detection laser. The slope for λ_{633} = -4.2111e-04 and λ_{589} = -4.4440e-04.

C

Setting up the optical tweezers

This appendix shows the experimentally determined κ versus the amplitude as set on the AOD (Figure C.1). It can be seen a maximum is obtained at 2.2 mW. The ultra-low stiffness experiments are conducted at 20% emission and 0.7 mW. Figure C.2 shows a correct alignment of the trapping laser and the detection laser. The blue and red curve should overlap, meet at (0,0), and should be sufficiently linear. This is for a bead with r_b = 0.5 µm, so it should be linear for at leasat $\pm$0.1 MHz.

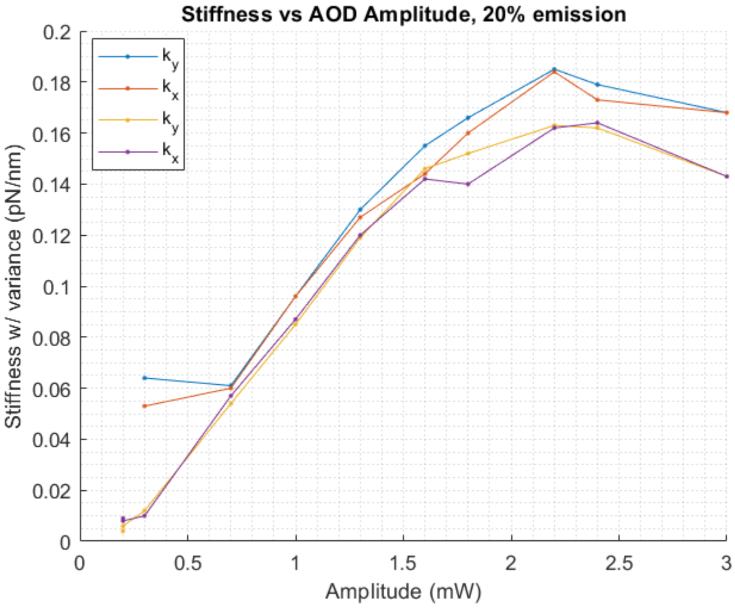

Figure C.1: The trapping stiffness κ for various amplifications, two experiments. For both experiments the maximum trapping stiffness is at 2.2 mW.

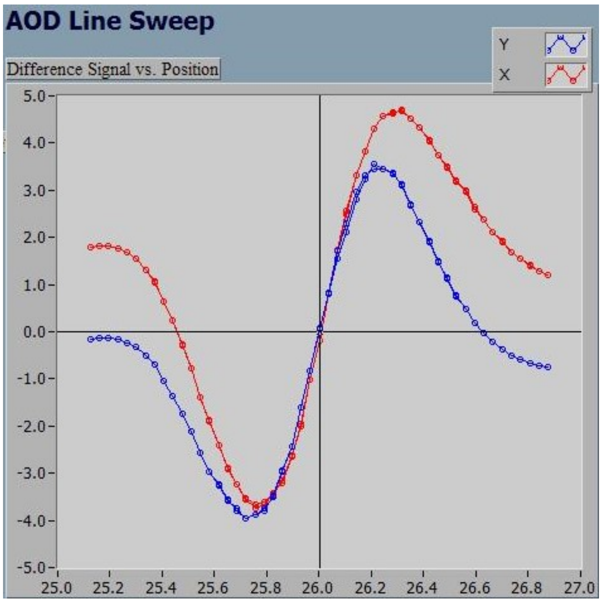
AOD Line Sweep
Difference Signal vs. Position
Y
X
5.0
4.0
3.0
2.0
1.0
0.0
-1.0
-2.0
-3.0
-4.0
-5.0
25.0
25.2
25.4
25.6
25.8
26.0
26.2
26.4
26.6
26.8
27.0

Figure C.2: An exemplary PSD reading from an AOD line sweep in the x-direction, for a bead of d_b = 1 µm.

D

Model adaptations for this thesis

In the previous model θ_{min} was discretized. For this thesis an addition to the previous model has been made to solve for θ with a reasonable accuracy. An extra nested while-loop has been implemented, as can also be seen in Figure 3.5. This required resetting the solver settings. In addition, the previous model followed a minimization of energy to obtain the interfacial tension. This model was made to research lipid bilayers, and thus included bending rigidity for nanotube extension. The part of the model that converts the geometrical parameters z_b and θ_{min} to energy, was rewritten according to Equation 3.8.

Figure D.1 shows the difference between the discretized θ_{min} and the improved solution. As can be seen in Figure D.2, this makes a minor difference in development of the area. The total area A_{tot} is differentiated over z_b and for both models the curve is smooth. Figure D.3 shows the resulting difference in force for three different γ. The higher the interfacial tension, the larger the difference in the models. It should be noted that the old model was originally developed for r_b = 2.5 μm and is now run with the same discretization for r_b = 0.5 μm. The improvements will be more visible for a larger radius.

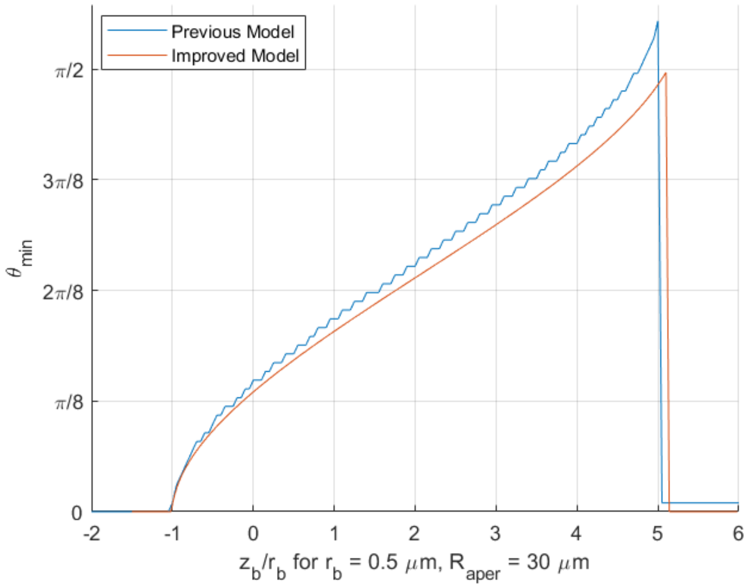

Figure D.1: The improved model solves for θ instead of discretizing.

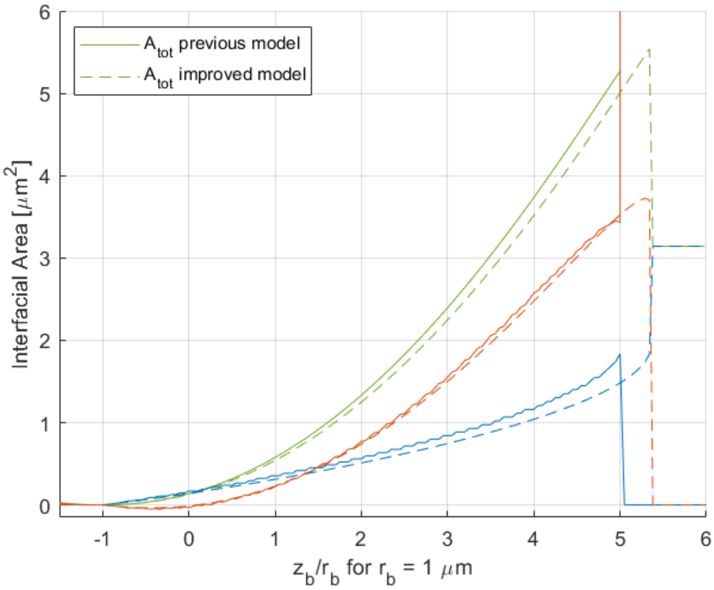

Figure D.2: Interfacial area for the two models. The previous model discretized θ, but a smooth curve of A_{tot} is obtained.

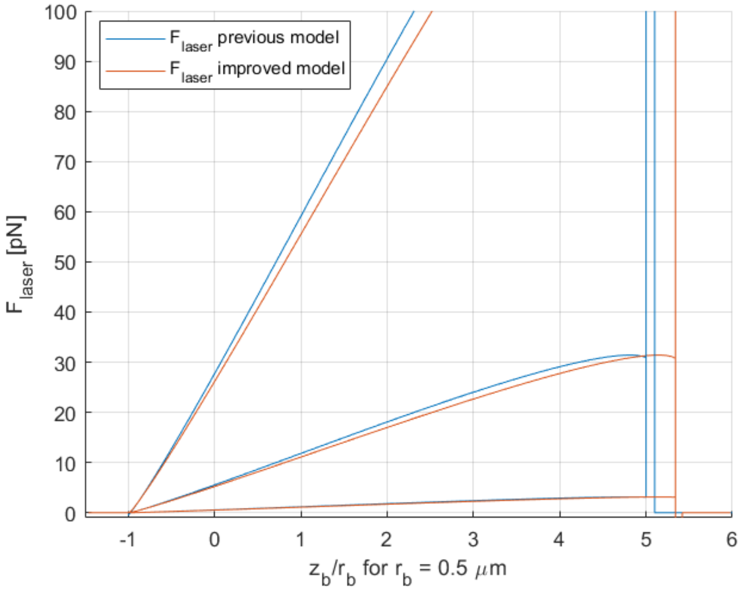

Figure D.3: Difference in modelled F_{OT} for γ = 10^{-4}, 510^{-5}, 10^{-5} N m^{-1}. The higher the interfacial tension, the bigger the difference in the two models.

E

Full results

This Appendix provides the full experimental details. We present the relative bead position and variance versus the bead position near the interface and touching. For the experiments with an interface containing solely Span-80, we only have the variance in voltage due to an error in the LabView program. We also present the obtained estimates for the trapping stiffness in the two directions mentioned in this thesis, as well as rotated $\pi/2$. If all four estimates for the variance are similar, the resulting spot will be circular upon calibration.

E.1. Exp 1 - Interface containing Span-80

Table E.1: The calibrated values for the trapping stiffness in four directions. All values are in pN nm^{-1}.

κ_x	κ_y	$\kappa_{x'}$	$\kappa_{y'}$
0.482	0.455	0.532	0.418

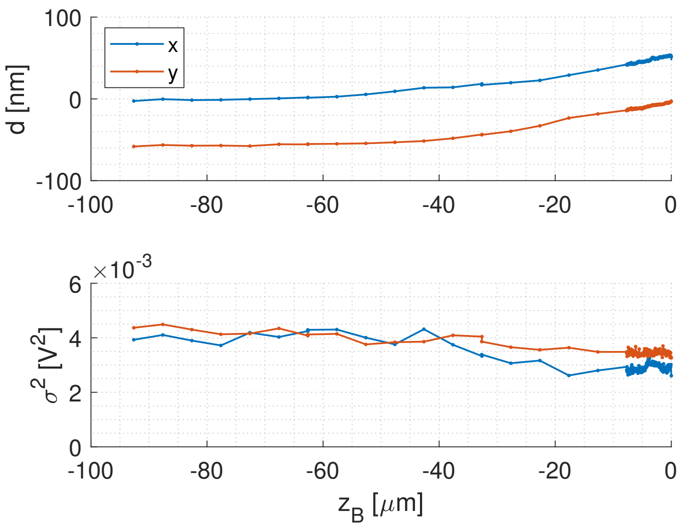

Figure E.1: The relative bead position versus actual bead position and variance for Exp 1.

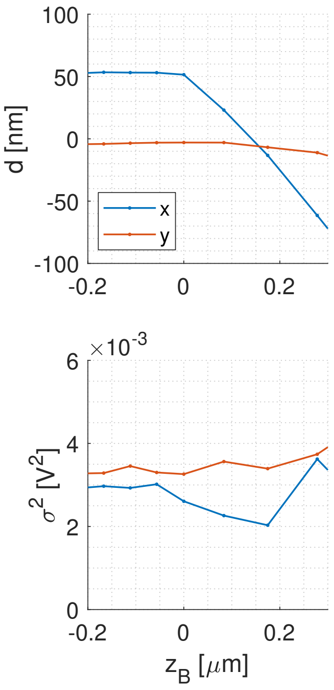

Figure E.2: The relative bead position versus actual bead position and variance for Exp 1.

E.2. Exp 2.1 - Interface containing Span-80

Table E.2: The calibrated values for the trapping stiffness in four directions. All values are in pN nm^{-1}.

κ_x	κ_y	$\kappa_{x'}$	$\kappa_{y'}$
0.123	0.166	0.139	0.143

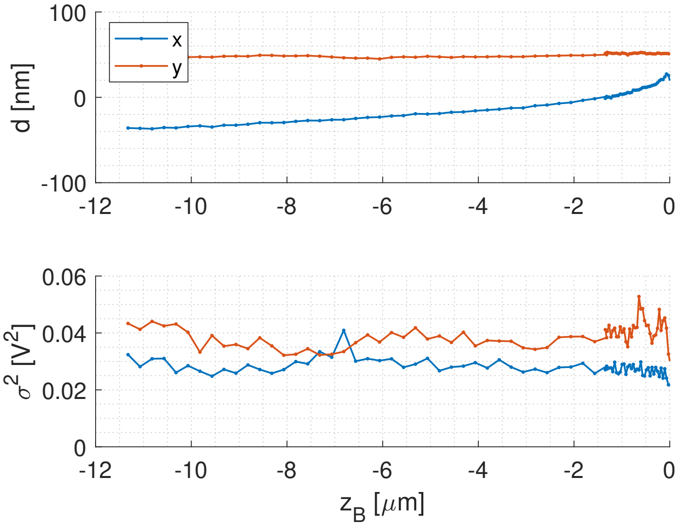

Figure E.3: The relative bead position versus actual bead position and variance for Exp 2.1.

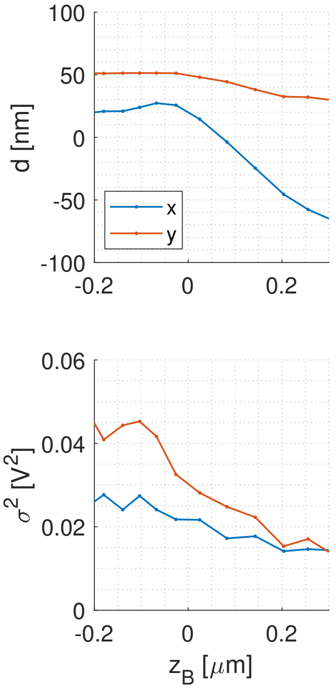

Figure E.4: The relative bead position versus actual bead position and variance near the interface for Exp 2.1.

E.3. Exp 2.2 - Interface containing Span-80

Table E.3: The calibrated values for the trapping stiffness in four directions. All values are in pN nm^{-1}.

κ_x	κ_y	$\kappa_{x'}$	$\kappa_{y'}$
0.369	0.493	0.418	0.426

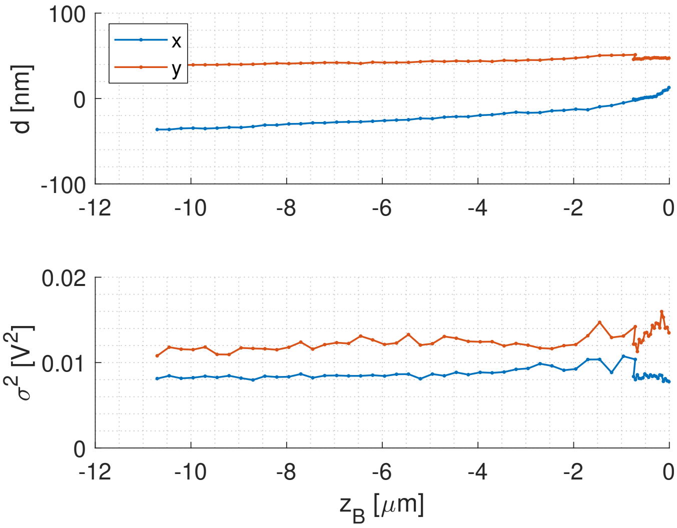

Figure E.5: The relative bead position versus actual bead position and variance for Exp 2.2.

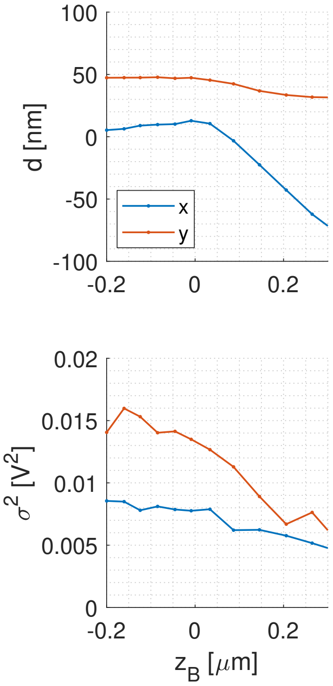

Figure E.6: The relative bead position versus actual bead position and variance near the interface, for Exp 2.2.

E.4. Exp 3.1 - Interface containing Span-80 and SDS

Table E.4: The calibrated values for the trapping stiffness in four directions. All values are in pN nm^{-1}.

κ_x	κ_y	$\kappa_{x'}$	$\kappa_{y'}$
0.124	0.095	0.109	0.106

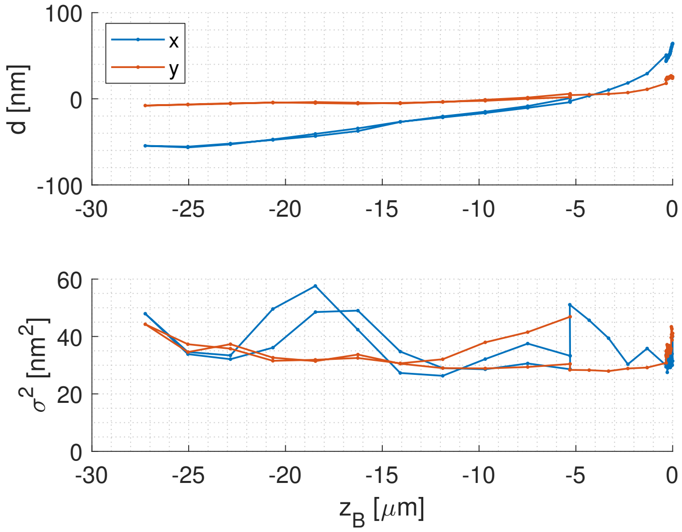

Figure E.7: The relative bead position versus actual bead position and variance for Exp 3.1.

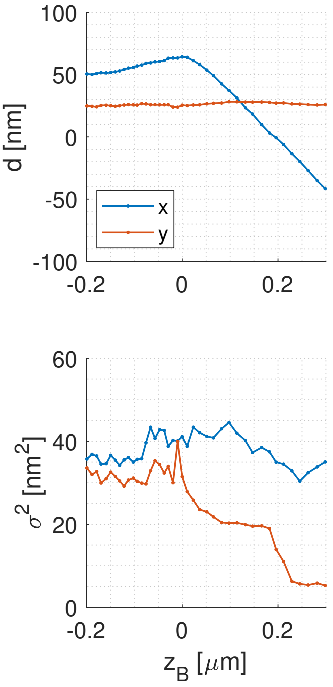

Figure E.8: The relative bead position versus actual bead position and variance near the interface, for Exp 3.1.

E.5. Exp 3.2 - Interface containing Span-80 and SDS

Table E.5: The calibrated values for the trapping stiffness in four directions. All values are in pN nm^{-1}.

κ_x	κ_y	$\kappa_{x'}$	$\kappa_{y'}$
0.058	0.067	0.061	0.063

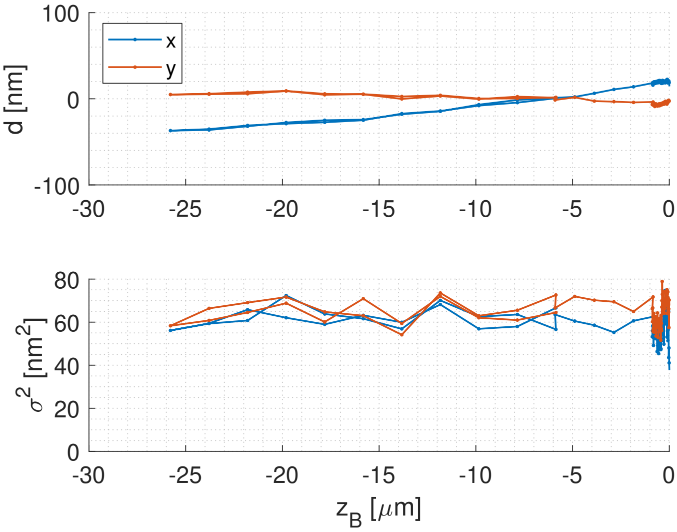

Figure E.9: The relative bead position versus actual bead position and variance for Exp 3.2.

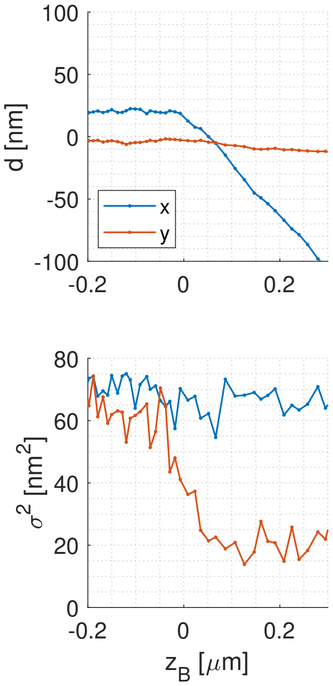

Figure E.10: The relative bead position versus actual bead position and variance near the interface, for Exp 3.2.

E.6. The position variance is found not to vary due to noise

Figure E.11 shows the relative bead position and variance for a system with at the organic phase Span-80 at the critical micelle concentration and at the aqueous phase 6 mM SDS, which should reduce the interfacial tension to the ultra-low regime ($\gamma \approx 10^{-5}$ N/m)[12]. The bead starts approximately 5 µm from the interface. At this point, the calibration procedure for converting the voltage signal to spatial dimensions is completed. The bead moves back and forth 20 µm away from the interface, with a coarse step size, to probe the optical homogeneity of the system. Then, the bead comes near the interface, using the coarse step size. When the bead approaches the interface the step size is reduced to 10 nm. In this experiment, the step size was reduced too late, such that the bead was already touching the interface. This explains the jump in the relative bead position in Figure E.12. Between −25 µm and the point of calibration, the x-direction has a drift of 95 µm, where in the y-direction there is nearly no drift. The variance is fluctuating without a visible pattern and is increasing upon touching the interface. It appears the variance is decreasing slightly over 25 µm in Figure E.11.

The PwSD is computed from four data points, denoted as a, b, c and d in Figure E.11. The result in shown in Figure E.13. The spectrum seems constant, and noise does not appear to make a contribution to the fluctuations in the variance. Figure E.14 shows the eccentricity and orientation of the spot of the raw voltage data. The voltage reading on the PSD appears to be constant throughout this experiment. The slight increase in eccentricity and decrease in orientation, just before the set zero, is due to the bead already touching the interface before the step size was reduced.

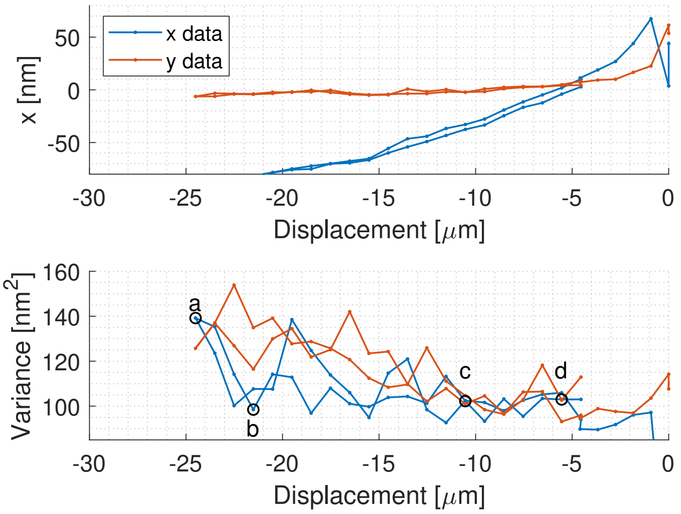

Figure E.11: The relative bead position as a function of distance to the interface for low laser power and κ_{OT} = 0.03 pN nm^{-1}.

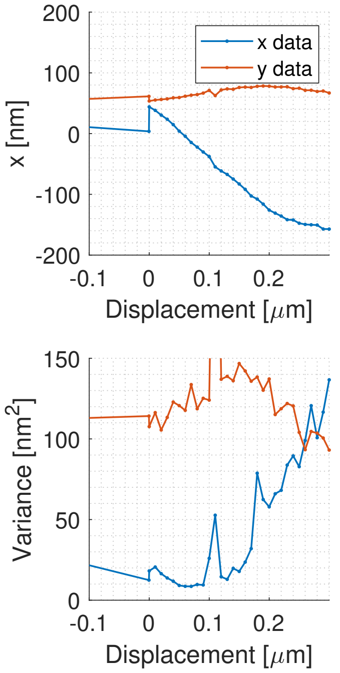

Figure E.12: The relative bead position and variance when touching the interface.

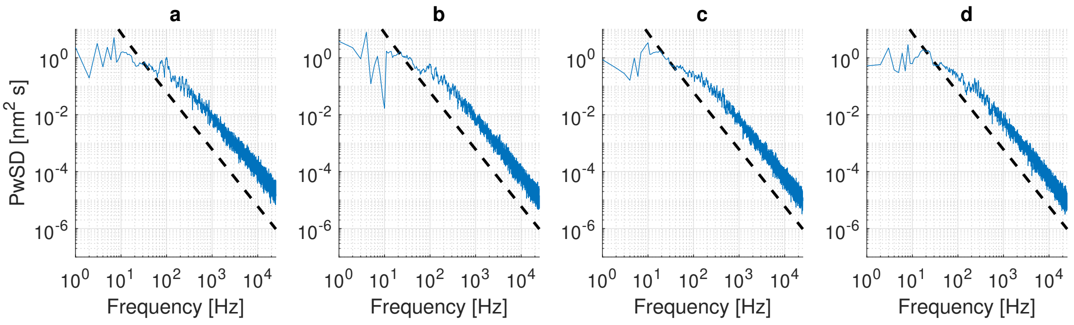

Figure E.13: The power spectral density for the dataset with low power, corresponding to Figure E.11.

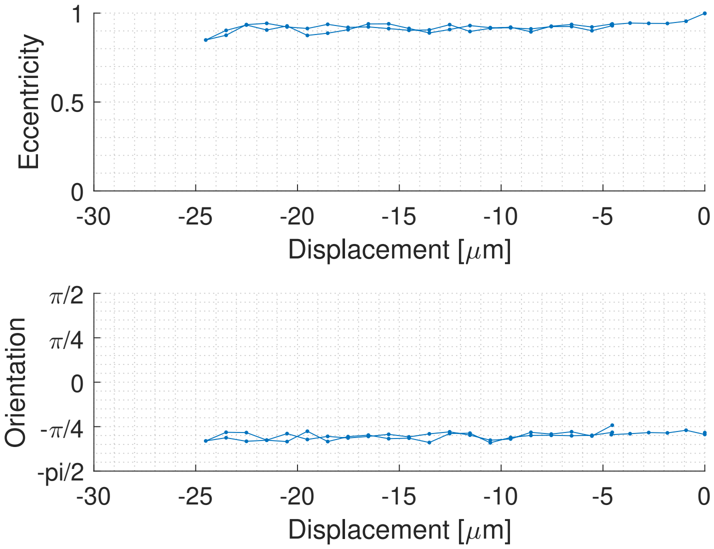

Figure E.14: The eccentricity and orientation of the voltage reading on the PSD for the dataset with low power, corresponding to Figure E.11.

The experiment as discussed in the previous section is repeated at exactly the same interface, same location and with the same bead path, but with a different bead and a medium trapping power, resulting in an estimated κ_x = 0.26 pN nm^{-1}. Figure E.15 shows the relative bead position and variance. As in the experiment with the low trapping power, there is no significant drift in the y-direction, whereas there is a significant drift in the x-direction: 55 µm from -25 µm to the point of calibration. The variance, especially in the direction perpendicular to the interface, is fluctuating. The measured variance does not scale with the previous trapping stiffness, which would be $\sigma_x^2 \approx 14$ nm^2. Figure E.16 shows that the variance is decreasing upon touching the interface.

Figure E.17 shows the eccentricity and orientation of the direct PSD reading to be constant near the interface. In figure E.15 three datapoints are selected. Point a denotes the first point of the measurement, at the location where the calibration procedure is also carried out. Point b and c are at -21 µm, but show a significantly different variance. Figure E.18 shows the scattered data for these three points. The voltage reading on the PSD changes shape, despite the bead not being near the interface. This effects the calibration to spatial dimensions, causing large variations in the variance.

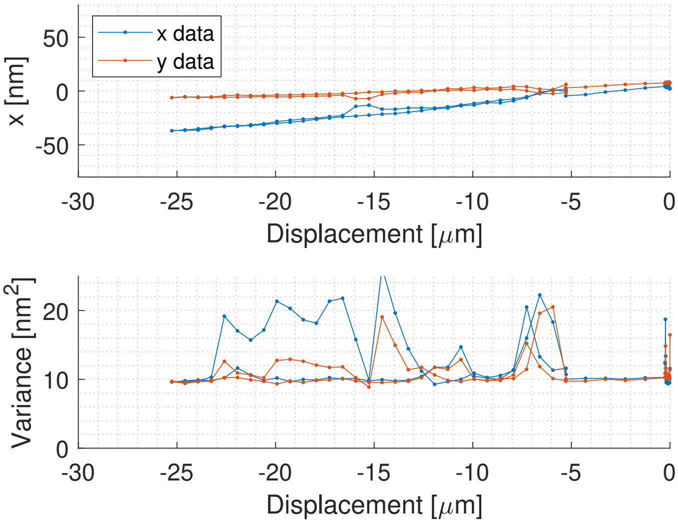

Figure E.15: The relative bead position as a function of distance to the interface for medium laser power and κ_{OT} = 0.26 pN nm^{-1}. The highlighted points a, b and c are further analysed in Figure E.18.

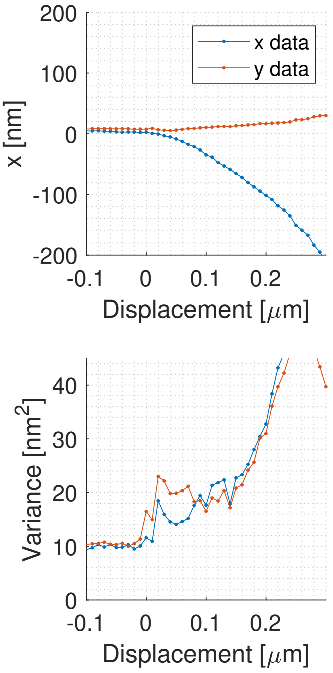

Figure E.16: The relative bead position and variance when touching the interface.

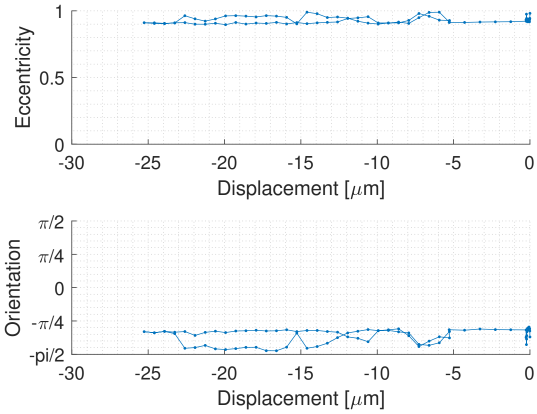

Figure E.17: The eccentricity and orientation of the voltage reading on the PSD for the dataset with medium power, corresponding to Figure E.15.

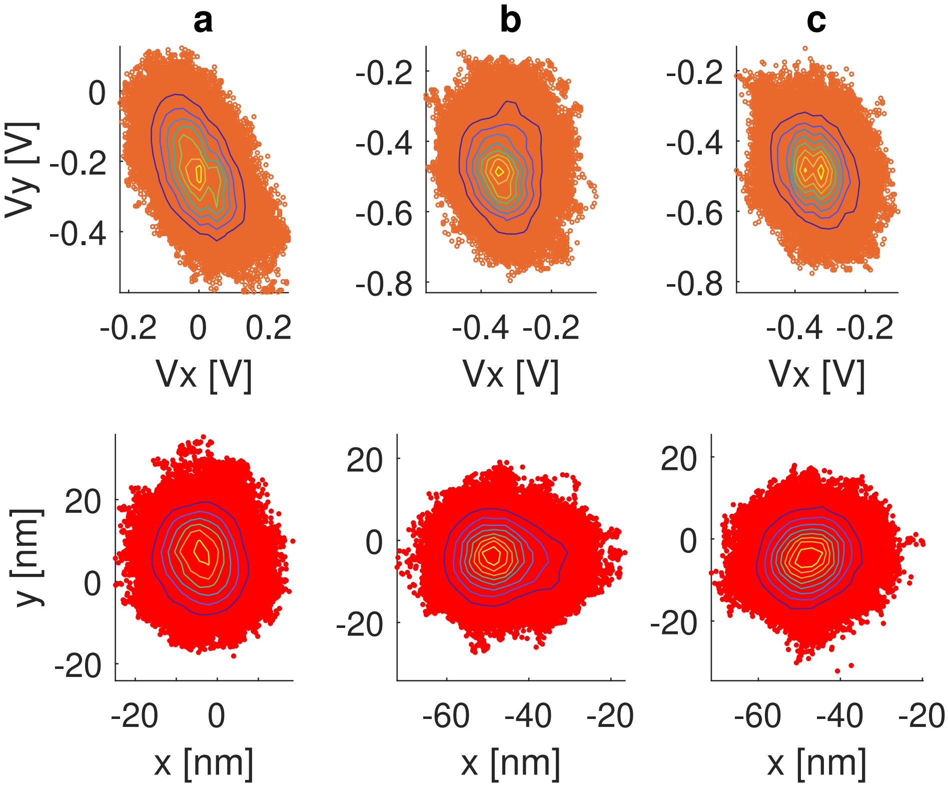

Figure E.18: Scattered voltage and spatial data for three different positions, denoted by a, b and c, as in Figure E.15. The voltage data is shown in orange whereas the spatial data (nm) is shown in red. The calibration procedure from voltage to nanometer is nearly linear, however, a fifth order polynomial is fitted to achieve a higher resolution.

E.7. The device does not influence the optical drift or variance fluctuations

Figure E.19 and E.20 show the variance and relative bead position as the bead crosses the aperture. No trend is observed.

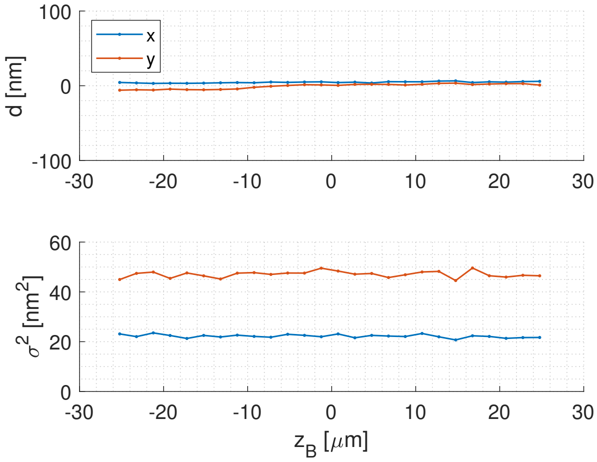

Figure E.19: Position and variance through empty aperture at middle of device: that is 50 µm from the bottom.

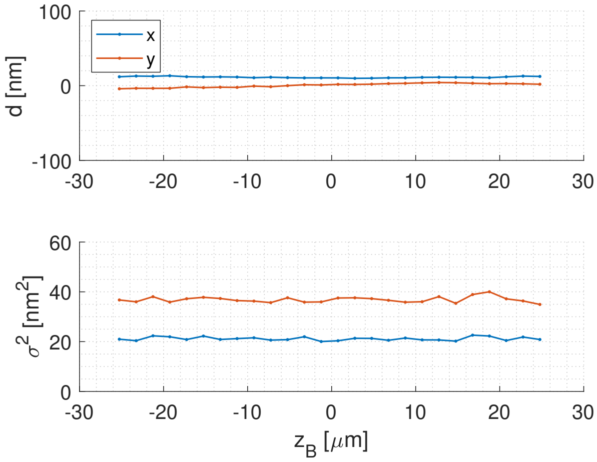

Figure E.20: Position and variance through empty aperture at 30 µm height in device.

E.8. Parallel to the interface

Figure E.21, E.22 and E.23 show the relative bead position as the bead moves parallel to an index matched interface. It is observed that the deviations are not symmetric, and not the same for x and y.

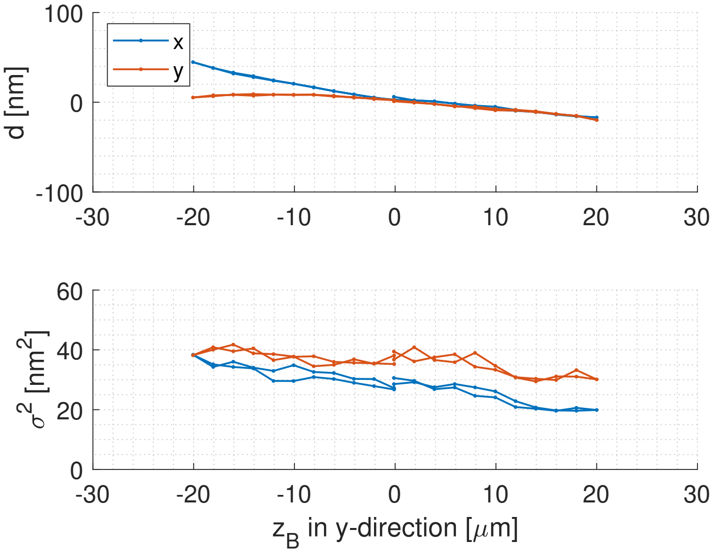

Figure E.21: The relative bead position and variance as the bead moves parallel to the interface. The measurement starts at 0 and moves 25 µm in both parallel directions.

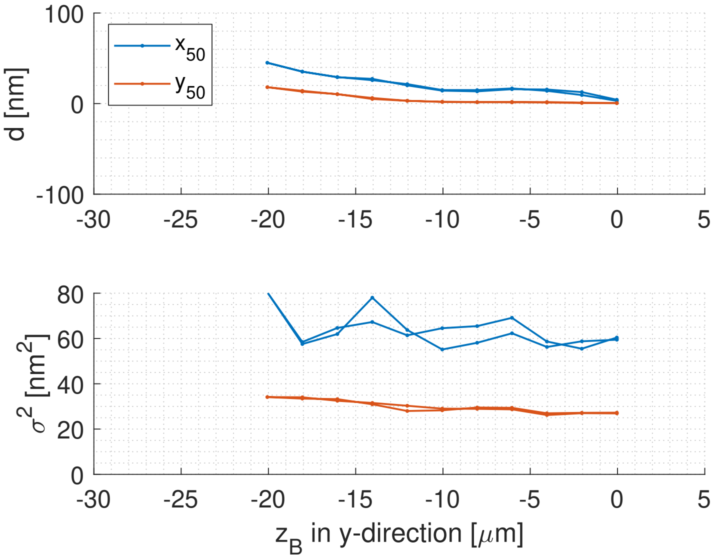

Figure E.22: The relative bead position and variance as the bead moves parallel to the interface. The measurement starts at 0 and moves 25 µm in both parallel directions.

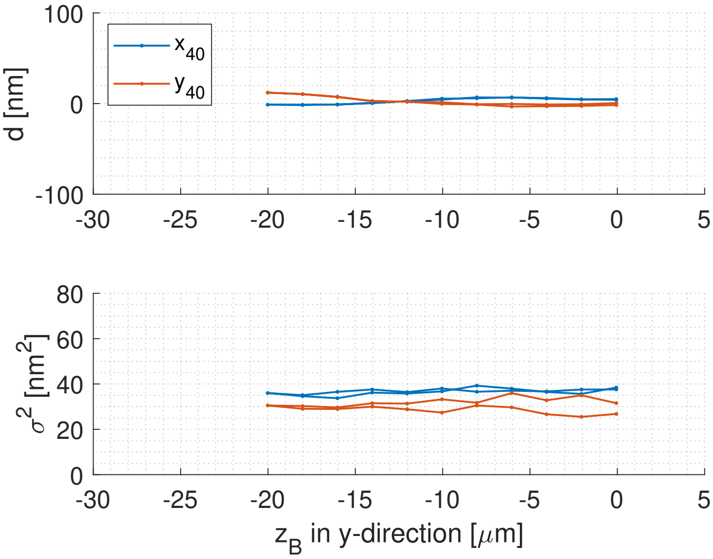

Figure E.23: The relative bead position and variance as the bead moves parallel to the interface. The measurement starts at 0 and moves 20 μm away.This measurement is at the same coordinates at Figure E.22, but 10 μm lower in the device.

E.9. Stiffness as function of distance to interface

We measured the trapping stiffness as a function of distance to the interface, for three different emissions: medium power, 20% emission, high power, 30% emission and very high power or 40% emission. Figure E.24 shows the outcome, where the interface is located at 0. the x-symbol denotes κ_y, where the o-symbol denotes κ_x. It can be seen that the higher the emission power, the more κ_x and κ_y deviate. This can be either due to an asymmetric laser, or reduced resolution, since the variance becomes smaller at higher emission powers. We conclude to operate the laser at maximum 30% emission.

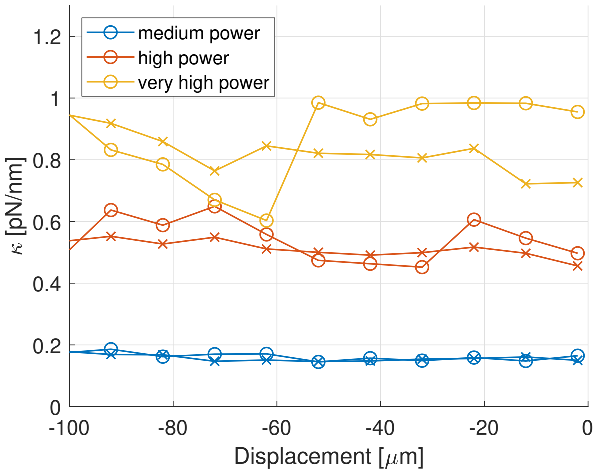

Figure E.24: The obtained estimates for the trapping stiffnesses as a function of distance to the interface. Here, the interface is located at 0. the x-symbol denotes κ_y, where the o-symbol denotes κ_x.

F

Absorbance spectrum

Fourier-transform infrared spectroscopy (FTIR) results for two index matched fluids. It can be seen that even though n is sufficiently matched, the two fluids have distinctly different absorbance spectrum. Moreover, the absorbance is also different for the wavelength of the detection laser and the trapping laser. Despite these differences, we are able to properly trap and think we have obtained reliable results.

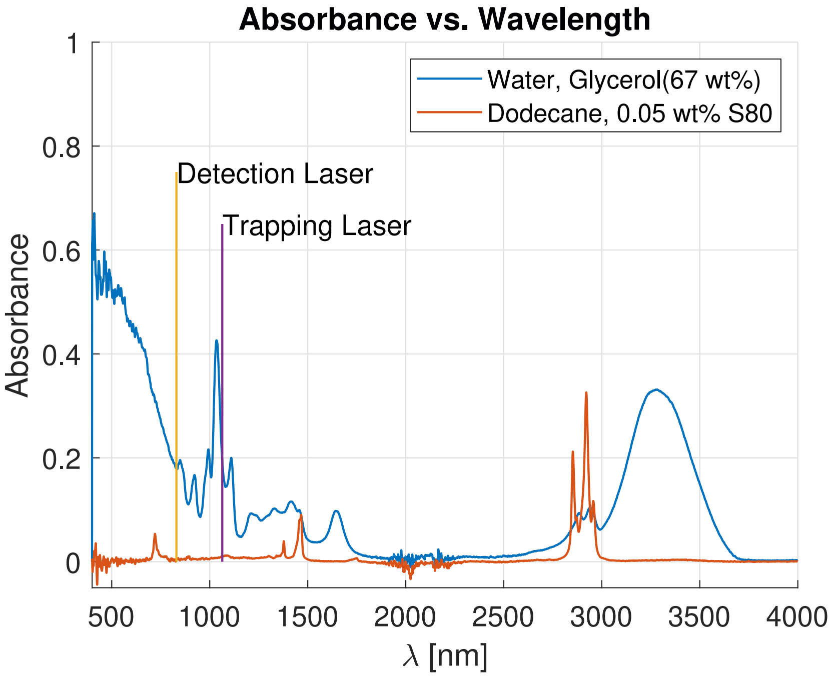

Figure F.1: FTIR results for two index matched fluids. The vertical yellow and purple line denote the wavelengths of the detection and trapping laser.

G

MATLAB code model

The MATLAB code for the model as well as further explanation can be obtained via the K-drive of the Aubin-Tam lab, via the following working directory: *W:-groups*.

Bibliography

[1] A. Dols-Perez, V. Marin, G. J. Amador, R. Kieffer, D.S.W. Tam, and M.-E. Aubin-Tam. Artificial Cell Membranes Interfaced with Optical Tweezers: A Versatile Microfluidics Platform for Nanomanipulation and Mechanical Characterization. *ACS Applied Materials & Interfaces*, 11(37):33620–33627, 2019. ISSN 1944-8244. doi: 10.1021/acsami.9b09983.

[2] A. L. Márquez and J. R. Wagner. Rheology of double (w/o/w) emulsions prepared with soybean milk and fortified with calcium. *Journal of Texture Studies*, 41(5):651–671, 2010. ISSN 00224901. doi: 10.1111/j.1745-4603.2010.00247.x.

[3] M.J. Rosen, H. Wang, P. Shen, and Y. Zhu. Ultralow interfacial tension for enhanced oil recovery at very low surfactant concentrations. *Langmuir*, 21(9):3749–3756, 2005. ISSN 07437463. doi: 10.1021/la0400959.

[4] M.J. Rosen. *Surfactants and Interfacial Phenomena*, volume 62. 2004. ISBN 9786468600. doi: 10.1093/jaoac/62.3.700.

[5] P.-G. de Gennes, F. Brochard-Wyart, and D. Quéré. *Capillarity and Wetting Phenomena*, volume 163. 2004. doi: 10.1016/j.ygcen.2009.04.018.

[6] J.W.M.; Bush. Interfacial Phenomena [Lecture Notes]. Technical report, Massachusetts Institute of Technology, 2010. URL https://ocw.mit.edu/courses/mathematics/18-357-interfacial-phenomena-fall-2010/lecture-notes/MIT18_357F10_lec_all.pdf.

[7] P.K. Kundu, I.M. Cohen, and D.R. Dowling. *Fluid Mechanics*, volume 110. Elsevier Inc., 6th edition, 2016. ISBN 9788578110796.

[8] P. Posocco, A. Perazzo, V. Preziosi, E. Laurini, S. Pricl, and S. Guido. Interfacial tension of oil/water emulsions with mixed non-ionic surfactants: Comparison between experiments and molecular simulations. *RSC Advances*, 6(6):4723–4729, 2016. ISSN 20462069. doi: 10.1039/c5ra24262b.

[9] A. Perazzo, V. Preziosi, and S. Guido. Phase inversion emulsification: Current understanding and applications. *Advances in Colloid and Interface Science*, 222:581–599, 2015. ISSN 00018686. doi: 10.1016/j.cis.2015.01.001. URL http://dx.doi.org/10.1016/j.cis.2015.01.001.

[10] S. Zeppieri, J. Rodríguez, and A. L. López De Ramos. Interfacial tension of alkane + water systems. *Journal of Chemical and Engineering Data*, 46(5):1086–1088, 2001. ISSN 00219568. doi: 10.1021/je000245r.

[11] A. H. Cortés-Estrada, L. A. Ibarra-Bracamontes, A. Aguilar-Corona, G. Viramontes-Gamboa, and G. Carbajal-De la Torre. Surface Tension and Interfacial Tension Measurements in Water-Surfactant-Oil Systems. *Experimental and Computational Fluid Mechanics*, 2014. doi: 10.1007/978-3-319-00116-6.

[12] S.H. Tsai, J. S. Wexler, J. Wan, and H. A. Stone. Microfluidic ultralow interfacial tensiometry with magnetic particles. *Lab on a Chip*, 13(1):119–125, 2013. ISSN 14730189. doi: 10.1039/c2lc40797c.

[13] J. Drelich. Conference Record of the Twenty-Second IEEE Photovoltaic Specialists Conference - 1991. *Conference Record of the IEEE Photovoltaic Specialists Conference*, 2:833–1598, 2002. ISSN 01608371. doi: 10.1109/pvsc.1997.653910.

[14] J. M. Andreas, E. A. Hauser, and W. B. Tucker. Boundary tension by pendant drops. *Journal of Physical Chemistry*, 42(7):1001–1019, 1938. ISSN 00223654. doi: 10.1021/j100903a002.

[15] P. Chen, D. Y. Kwok, R. M. Prokop, O. I. del Rio, S. S. Susnar, and A. W. Neumann. *Axisymmetric Drop Shape Analysis (ADSA) and its Applications*, volume 6. 1998. doi: 10.1016/S1383-7303(98)80019-7.

[16] E. Atefi, J. A. Mann, and H. Tavana. Ultralow interfacial tensions of aqueous two-phase systems measured using drop shape. *Langmuir*, 30(32):9691–9699, 2014. ISSN 15205827. doi: 10.1021/la500930x.

[17] B. Vonnegut. Rotating bubble method for the determination of surface and interfacial tensions. *Review of Scientific Instruments*, 13(1):6–9, 1942. ISSN 00346748. doi: 10.1063/1.1769937.

[18] T. Sottmann and R. Strey. Ultralow interfacial tensions in water – - alkane – surfactant systems. 8606(February 1997), 2001.

[19] E.H.A. de Hoog and H. N.W. Lekkerkerker. Measurement of the interfacial tension of a phase-separated colloid-polymer suspension. *Journal of Physical Chemistry B*, 103(25):5274–5279, 1999. ISSN 10895647. doi: 10.1021/jp990061n.

[20] J. D. Berry, M.J. Neeson, R. R. Dagastine, D.Y.C. Chan, and R. I. F. Tabor. Measurement of surface and interfacial tension using pendant drop tensiometry. *Journal of Colloid and Interface Science*, 454:226–237, 2015. ISSN 10957103. doi: 10.1016/j.jcis.2015.05.012. URL `http://dx.doi.org/10.1016/j.jcis.2015.05.012`.

[21] S. D. Hudson, J. T. Cabral, W. J. Goodrum, K. L. Beers, and E. J. Amis. Microfluidic interfacial tensiometry. *Applied Physics Letters*, 87(8):2003–2006, 2005. ISSN 00036951. doi: 10.1063/1.2034098.

[22] L. Wilhelmy. Physik und Chemie. *Ann. Phys. Chem.*, 4(29):177–217, 1863. doi: 10.1007/978-3-663-02353-1{_}12.

[23] J. Sprakel, N. A.M. Besseling, F. A.M. Leermakers, and M. A. Cohen Stuart. Equilibrium capillary forces with atomic force microscopy. *Physical Review Letters*, 99(10):2–5, 2007. ISSN 00319007. doi: 10.1103/PhysRevLett.99.104504.

[24] P. M. McGuiggan, D.A. Grave, J. S. Wallace, S. Cheng, A. Prosperetti, and M. O. Robbins. Dynamics of a disturbed sessile drop measured by atomic force microscopy (AFM). *Langmuir*, 27 (19):11966–11972, 2011. ISSN 07437463. doi: 10.1021/la2023709.

[25] G. D. Nadkarni and S. Garoff. An investigation of microscopic aspects of contact angle hysteresis: Pinning of the contact line on a single defect. *Europhysics Letters*, 20(6):523–528, 1992. ISSN 12864854. doi: 10.1209/0295-5075/20/6/009.

[26] G. Bolognesi, Y. Saito, A. I.I. Tyler, A. D. Ward, C. D. Bain, and O. Ces. Mechanical Characterization of Ultralow Interfacial Tension Oil-in-Water Droplets by Thermal Capillary Wave Analysis in a Microfluidic Device. *Langmuir*, 32(15):3580–3586, 2016. ISSN 15205827. doi: 10.1021/acs.langmuir.5b04702.

[27] H. Zhou, B. B. Gabilondo, W. Losert, and W. Van De Water. Stretching and relaxation of vesicles. *Physical Review E - Statistical, Nonlinear, and Soft Matter Physics*, 83(1):1–8, 2011. ISSN 15393755. doi: 10.1103/PhysRevE.83.011905.

[28] D. G.A.L. Aarts, M. Schmidt, and H. N.W. Lekkerkerker. Direct Visual Observation of Thermal Capillary Waves. *Science*, 304(5672):847–850, 2004. ISSN 00368075. doi: 10.1126/science.1097116.

[29] Y. M. Lau, J. Westerweel, and W. Van De Water. Using Faraday Waves to Measure Interfacial Tension. *Langmuir*, 36(21):5872–5879, 2020. ISSN 15205827. doi: 10.1021/acs.langmuir.0c00622.

[30] F.R.S. Lord Rayleigh. On the Instability of Jets. *Proceedings of the London Mathematical Society*, (June 1873):4–13, 1878.

[31] M. Tjahjadi, J. M. Ottino, and H. A. Stone. Estimating interfacial tension via relaxation of drop shapes and filament breakup. *AIChE Journal*, 40(3):385–394, 1994. ISSN 15475905. doi: 10.1002/aic.690400302.

[32] M. Moiré, Y. Peysson, B. Herzhaft, N. Pannacci, F. Gallaire, L. Augello, C. Dalmazzone, and A. Colin. Ultralow Interfacial Tension Measurement through Jetting/Dripping Transition. *Langmuir*, 33(10):2531–2540, 2017. ISSN 15205827. doi: 10.1021/acs.langmuir.7b00076.

[33] A. Yeung, T. Dabros, and J. Masliyah. Does equilibrium interfacial tension depend on method of measurement? *Journal of Colloid and Interface Science*, 208(1):241–247, 1998. ISSN 00219797. doi: 10.1006/jcis.1998.5807.

[34] F. Ortega, H. Ritacco, and R.G. Rubio. Interfacial microrheology: Particle tracking and related techniques. *Current Opinion in Colloid and Interface Science*, 15(4):237–245, 2010. ISSN 13590294. doi: 10.1016/j.cocis.2010.03.001. URL `http://dx.doi.org/10.1016/j.cocis.2010.03.001`.

[35] R. Shlomovitz, A. A. Evans, T. Boatwright, M. Dennin, and A. J. Levine. Measurement of monolayer viscosity using noncontact microrheology. *Physical Review Letters*, 110(13):29–33, 2013. ISSN 00319007. doi: 10.1103/PhysRevLett.110.137802.

[36] A. Dols-Perez, V. Marin, G. J. Amador, R. Kieffer, D.S.W. Tam, and M.-E. Aubin-Tam. Artificial Cell Membranes Interfaced with Optical Tweezers: A Versatile Microfluidics Platform for Nanomanipulation and Mechanical Characterization. *ACS Applied Materials and Interfaces*, 11(37):33620–33627, 2019. ISSN 19448252. doi: 10.1021/acsami.9b09983.

[37] A. Ashkin. Atomic-Beam Deflection by Resonance-Radiation Pressure. *Physical Review Letters*, 25(19):1321–1324, 1970. ISSN 1098-6596. doi: 10.1017/CBO9781107415324.004.

[38] A. Ashkin and J. M. Dziedzic. Observation of Radiation-Pressure Trapping of Particles by Alternating Light Beams. *Physical Review Letters*, 54(12):1245–1248, 1985.

[39] V.M. Marin Lizarraga. *Bridging the gap: combined optical tweezers with free standing lipid membrane*. PhD thesis, Delft Univerisity of Technology, 2018. URL `https://doi.org/10.4233/uuid:38f761f4-6d73-4ca9-9cca-8de432184f0c`.

[40] G. Volpe and G. Volpe. Simulation of a Brownian particle in an optical trap. *American Journal of Physics*, 81(3):224–230, 2013. ISSN 0002-9505. doi: 10.1119/1.4772632.

[41] W. H. Wright, G. J. Sonek, and M. W. Berns. Parametric study of the forces on microspheres held by optical tweezers. *Applied Optics*, 33(9):1735, 1994. ISSN 0003-6935. doi: 10.1364/ao.33.001735.

[42] R. M. Simmons and T. Jeffrey. Displacement Using. *Biophysical journal*, 70(April):10, 1996. ISSN 00063495.

[43] Y. Jun, S. K. Tripathy, B. R.J. Narayanareddy, M. K. Mattson-Hoss, and S. P. Gross. Calibration of optical tweezers for in vivo force measurements: How do different approaches compare? *Biophysical Journal*, 107(6):1474–1484, 2014. ISSN 15420086. doi: 10.1016/j.bpj.2014.07.033. URL `http://dx.doi.org/10.1016/j.bpj.2014.07.033`.

[44] M. Sarshar, W.T. Wong, and B. Anvari. Comparative study of methods to calibrate the stiffness of a single-beam gradient-force optical tweezers over various laser trapping powers. 19(11):1–12, 2014. doi: 10.1117/1.JBO.19. URL `http://biomedicaloptics.spiedigitallibrary.org/`.

[45] M.L. Gardel, M. T. Valentine, and D. A. Weitz. *Microrheology*. 1999.

[46] J. Lipfert, M. Wiggin, J. W.J. Kerssemakers, F. Pedaci, and N. H. Dekker. Freely orbiting magnetic tweezers to directly monitor changes in the twist of nucleic acids. *Nature Communications*, 2(1), 2011. ISSN 20411723. doi: 10.1038/ncomms1450.

[47] K.C. Neuman and A. Nagy. Single-molecule force spectroscopy: Optical tweezers, magnetic tweezers and atomic force microscopy. *Nature Methods*, 5(6):491–505, 2008. ISSN 15487091. doi: 10.1038/nmeth.1218.

[48] H. Yang, M. Cornaglia, R. Trouillon, T. Lehnert, and M. A. M. Gijs. Study of constrained Brownian motion of nanoparticles near an interface using optical tweezers. *Complex Light and Optical Forces IX*, 9379(February):93790W, 2015. ISSN 0277-786X. doi: 10.1117/12.2078341.

[49] E. Schäffer, S. F. Nørrelykke, and J. Howard. Surface forces and drag coefficients of microspheres near a plane surface measured with optical tweezers. *Langmuir*, 23(7):3654–3665, 2007. ISSN 07437463. doi: 10.1021/la0622368.

[50] T. Boatwright, M. Dennin, R. Shlomovitz, A. A. Evans, and A. J. Levine. Probing interfacial dynamics and mechanics using submerged particle microrheology. II. Experiment. *Physics of Fluids*, 26 (7), 2014. ISSN 10897666. doi: 10.1063/1.4887084.

[51] R. Shlomovitz, A. A. Evans, T. Boatwright, M. Dennin, and A.J. Levine. Probing interfacial dynamics and mechanics using submerged particle microrheology. I. Theory. *Physics of Fluids*, 26(7), 2014. ISSN 10897666. doi: 10.1063/1.4886996.

[52] Y. Shitamichi, M. Ichikawa, and Y. Kimura. Mechanical properties of a giant liposome studied using optical tweezers. *Chemical Physics Letters*, 479(4-6):274–278, 2009. ISSN 00092614. doi: 10.1016/j.cplett.2009.08.018. URL `http://dx.doi.org/10.1016/j.cplett.2009.08.018`.

[53] D. Wei. *Experimental Investigation of Ciliary Flow with C. reinhardtii: Hydrodynamics, Ultrastructure, and Ciliary difference*. PhD thesis, Delft University of Technology, 2020. URL `https://doi.org/10.4233/uuid:b803bf1d-cf2d-4049-baab-c5de098bdeb9`.

[54] M. Benmekhbi, S. Simon, and J. Sjöblom. Dynamic and Rheological Properties of Span 80 at Liquid-Liquid Interfaces. *Journal of Dispersion Science and Technology*, 35(6):765–776, 2014. ISSN 15322351. doi: 10.1080/01932691.2013.811573.

[55] M. Ito and T. Sato. In situ observation of a soap-film catenoid - A simple educational physics experiment. *European Journal of Physics*, 31(2):357–365, 2010. ISSN 01430807. doi: 10.1088/0143-0807/31/2/013.

[56] Y. H. Mori, N. Tsui, and M. Klyomlya. Surface and Interfacial Tensions and Their Combined Properties in Seven Binary, Immiscible Liquid-Liquid-Vapor Systems. *Journal of Chemical and Engineering Data*, 29(4):407–412, 1984. ISSN 15205134. doi: 10.1021/je00038a012.

[57] F. R. Beierlein, A. M. Krause, C. M. Jäger, P. Fita, E. Vauthey, and T. Clark. Molecular dynamics simulations of liquid phase interfaces: Understanding the structure of the glycerol/water-dodecane system. *Langmuir*, 29(38):11898–11907, 2013. ISSN 07437463. doi: 10.1021/la4021355.

[58] P. G. de Gennes. Wetting: statics and dynamics. *Reviews of Modern Physics*, 57(3):827–863, 1985.

[59] R. R. Brau, J. M. Ferrer, H. Lee, C. E. Castro, B. K. Tam, P. B. Tarsa, P. Matsudaira, M. C. Boyce, R. D. Kamm, and M. J. Lang. Passive and active microrheology with optical tweezers. *Journal of Optics A: Pure and Applied Optics*, 9(8), 2007. ISSN 14644258. doi: 10.1088/1464-4258/9/8/S01.

[60] K. Huang and I. Szlufarska. Effect of interfaces on the nearby Brownian motion. *Nature Communications*, 6:1–6, 2015. ISSN 20411723. doi: 10.1038/ncomms9558.

[61] T. Franosch, M. Grimm, M. Belushkin, F.M. Mor, G. Foffi, L. Forró, and S. Jeney. Resonances arising from hydrodynamic memory in Brownian motion. *Nature*, 478(7367):85–88, 2011. ISSN 00280836. doi: 10.1038/nature10498.

[62] A. Banerjee and K. D. Kihm. Experimental verification of near-wall hindered diffusion for the Brownian motion of nanoparticles using evanescent wave microscopy. *Physical Review E - Statistical, Nonlinear, and Soft Matter Physics*, 72(4):1–4, 2005. ISSN 15393755. doi: 10.1103/PhysRevE.72.042101.

[63] J. Rheims, J. Köser, and T. Wriedt. Refractive-index measurements in the near-IR using an Abbe refractometer. *Measurement Science and Technology*, 8(6):601–605, 1997. ISSN 09570233. doi: 10.1088/0957-0233/8/6/003.

[64] Y. Pang, H. Song, and W. Cheng. Using optical trap to measure the refractive index of a single animal virus in culture fluid with high precision. *Biomedical Optics Express*, 7(5):1672, 2016. ISSN 2156-7085. doi: 10.1364/boe.7.001672.

[65] M.M. Shindel, J. W. Swan, and E. M. Furst. Calibration of an optical tweezer microrheometer by sequential impulse response. *Rheologica Acta*, 52(5):455–465, 2013. ISSN 00354511. doi: 10.1007/s00397-013-0698-2.

[66] J. E. H. Pfisterer, R. I. Irvin, and N. Richard. Modeling physical optics phenomena by complex ray tracing. *Optical Engineering*, 54(3):035105, 2015. doi: 10.1117/1.

[67] H. C. Shum, A. Sauret, A. Fernandez-Nieves, H. A. Stone, and D. A. Weitz. Corrugated interfaces in multiphase core-annular flow. *Physics of Fluids*, 22(8), 2010. ISSN 10706631. doi: 10.1063/1.3480561.

[68] J. E. Saunders, C. Sanders, H. Chen, and H.-P. Loock. Refractive indices of common solvents and solutions at 1550 nm. *Applied Optics*, 55(4):947, 2016. ISSN 0003-6935. doi: 10.1364/ao.55.000947.

[69] M. Daimon and A. Masumura. Measurement of the refractive index of distilled water from the near-infrared region to the ultraviolet region. *Applied Optics*, 46(18):3811–3820, 2007. ISSN 15394522. doi: 10.1364/AO.46.003811.